



Durham E-Theses

Imaging polarimetry of cometary nebulae

Semple, Dominic Peter

How to cite:

Semple, Dominic Peter (1991) *Imaging polarimetry of cometary nebulae*, Durham theses, Durham University. Available at Durham E-Theses Online: <http://etheses.dur.ac.uk/6208/>

Use policy

The full-text may be used and/or reproduced, and given to third parties in any format or medium, without prior permission or charge, for personal research or study, educational, or not-for-profit purposes provided that:

- a full bibliographic reference is made to the original source
- a [link](#) is made to the metadata record in Durham E-Theses
- the full-text is not changed in any way

The full-text must not be sold in any format or medium without the formal permission of the copyright holders.

Please consult the [full Durham E-Theses policy](#) for further details.

IMAGING POLARIMETRY OF COMETARY NEBULAE.

Dominic Peter Semple B.Sc., Cert. Ed.

A thesis submitted to the University of Durham
for the degree of Doctor of Philosophy.

The copyright of this thesis rests with the author.
No quotation from it should be published without
his prior written consent and information derived
from it should be acknowledged.

Department of Physics
August 1991.

The copyright of this thesis rests with the author.
No quotation from it should be published without
his prior written consent and information derived
from it should be acknowledged.



18 AUG 1992

Abstract

In this work a review of many of the current theories of star formation as it is understood today is presented.

New polarimetric observations of three cometary nebulae, R Mon/NGC2261, R Cr A/NGC6729 and the Chamaeleon Infrared Nebula are presented and discussed. It is shown how previous polarimetric measurements of the illuminating source of Hubble's variable nebula (NGC2261) have often produced results which increase in error with increasing wavelength. The reason for this is that previous authors have used an aperture size for measurements of R Mon which includes effects of a highly polarized feature $\sim 5''$ north of R Mon. Though this phenomenon has been seen before by other observers, its effect on polarimetric measurements of R Mon has not been recognised before despite tests to check for this. The data presented here agree with the interpretation that this feature is the northern-lobe of a *mini-bipolar* nebula, and it is further suggested that this is a manifestation of episodic mass outflow from R Mon.

Previous explanations for the polarization of R Mon and R Cr A cannot explain the rapid change in polarization and position angle that these young stellar objects are seen to undergo. Models of these objects which assume that they appear as polarized sources are used to explain the polarizations and are discussed. These models are not only able to produce the level of polarization seen at the source, but they are also currently the best models for explaining the rapid changes in polarization that are observed.

A jet-like feature is seen to the south-west of the main nebulosity in the Chamaeleon IRN for the first time in observations presented in this thesis. A similar jet seen emerging from R Cr A has been explained as being an emission feature collimated by an inner-circumstellar disc by previous authors. Evidence presented in this work for the jets seen emanating from both R Cr A and the Chamaeleon IRN, suggests that these features are merely the preferentially illuminated rims of one of the outflow cavities, seen mainly by reflection of light from the source.

Further evidence is provided to show that NGC2261 and NGC6729 are illuminated by R Mon and R Cr A respectively. In the case of the Chamaeleon IRN new evidence is provided to show that the nebula is illuminated by a heavily obscured infrared source located midway between the two outflow cavities.

Contents

Abstract	i
List of figures	ii
Preface	iv
1 STAR FORMATION AND COMETARY NEBULAE	1
1.1 Introduction	1
1.2 Phase One	2
1.2.1 Cloud Core Formation	3
1.3 Phase Two	6
1.3.1 Magnetic Braking	6
1.3.2 Protostar Formation	7
1.4 Phase Three	9
1.4.1 Evidence for Outflows	9
1.4.2 Theories of Outflow	10
1.4.3 T Tauri Stars	14
1.4.4 Herbig-Haro Objects	19
1.4.5 Jets from Young Stellar Objects	29
1.5 Phase Four	33
1.6 Summary: The Four Stages of Star Formation	33
1.7 Cometary Nebulae	35
1.7.1 Dibai's Classifications of Nebulosities	35
1.7.2 Lada's Classifications for Molecular Outflows	38
1.7.3 Cometary Nebulae: A Model	39

1.8	Summary	42
2	THE POLARIZATION OF R MON/NGC2261	43
2.1	Introduction	43
2.2	Observations	48
2.2.1	The Aquisition of Data	48
2.2.2	The Importance of Seeing	50
2.3	Results	52
2.3.1	Polarization Maps	52
2.3.2	Synthesised Aperture Polarimetry	55
2.3.3	The Polarization Minimum	69
2.3.4	Polarization Measurements in NGC2261	70
2.3.5	Time Variation of Polarization in NGC2261/R Mon	73
2.4	Discussion and Interpretation	76
2.4.1	R Mon and The Polarization Knot	76
2.4.2	The Polarization Minimum	88
2.4.3	NGC2261	90
2.5	Conclusions	91
3	THE POLARIZATION OF R CrA	93
3.1	Introduction	93
3.2	Observations	98
3.3	Results	98
3.3.1	Polarization Maps	98
3.3.2	Synthesised Aperture Polarimetry	102
3.4	Discussion and Interpretation	110
3.4.1	NGC6729	110
3.4.2	R Cr A	111
3.4.3	The Jets	115
3.5	Conclusions	119

4	THE POLARIZATION OF THE CHAMAELEON IRN	120
4.1	Introduction	120
4.2	Observations	122
4.2.1	The Aquisition of Data	122
4.3	Results	122
4.3.1	Polarization Maps	122
4.3.2	Synthesised Aperture Polarimetry	129
4.4	Discussion and Interpretation	135
4.4.1	The Optical Knot, The Polarization Minimum and The IRS	135
4.4.2	The Nebula	140
4.5	Conclusions	141
5	SUMMARY AND CONCLUSIONS	143
5.1	Aperture Dependence of Polarization	144
5.2	Polarized Source Interpretations	145
5.3	Jets	145
5.4	Future Observations	146
5.5	Final Remarks	147
	Appendices	148
	A Polarization Maps of R Mon/NGC2261	149
	B Filter Responses	157
	References	159
	Acknowledgements	164

List of Figures

1.1	A diagram using the analogy of two fluids to help describe a Rayleigh-Taylor instability.	4
1.2	A magnetically braked cloud core. Adapted from Mouschovias (1980).	8
1.3	The molecular bipolar outflow configuration from Pudritz & Norman (1986). R_d is the radius of the circumstellar disk.	13
1.4	An intensity contour and polarization map of the HH83/Re17 nebula, (courtesy of Rolph 1990).	23
1.5	A schematic diagram which illustrates the main features of the shocked cloudlet model. Adapted from Schwartz (1978, 1985).	25
1.6	Schematic diagram illustrating the main points of the interstellar nozzle model for HH objects. Adapted from Cantó <i>et al.</i> (1980 & 1981).	28
1.7	A diagram summarising the “four stages of star formation.” Adapted from Shu <i>et al.</i> (1987).	34
1.8	The nebular classifications of Dibai (1971). Shaded areas are nebulous regions; the black circle is the illuminating source.	36
1.9	A schematic diagram depicting a bipolar nebula. One lobe of the bipolar is seen preferentially, and at optical wavelengths the object appears cometary in its morphology.	40
2.1	A greyscale intensity image of Hubble’s variable nebula. Data was taken in 1988 in the I waveband on the INT.	44
2.2	An intensity contour and polarization map of R Mon/NGC2261 from the 1988 I waveband dataset.	53

2.3	An intensity contour and polarization map of R Mon/NGC2261 from the 1989 V dataset. Note the null points in the polarization.	54
2.4	Polarization profile running north-south through R Mon. (Note: adjacent points do not represent independent polarization measurements due to smoothing effect of close aperture positions).	56
2.5	The variation of measured polarization for R Mon with aperture size. (Note the difference in scales on the polarization axis).	58
2.6	The polarization at R Mon using a 3" aperture (dotted line) and a 10" aperture (black circles) for the 1989 & 1990 datasets.	61
2.7	A greyscale polarization image (I waveband in March 1988). Note the highly polarized region (white) north of R Mon (cross).	65
2.8	The variation of polarization with wavelength for the polarization knot, from measurements using a 3" aperture on the 1989 and 1990 datasets.	66
2.9	The variation of polarization position angle with wavelength using a 3" aperture at different points for the 1989 (dotted-line) & 1990 data.	68
2.10	Variation of polarization with wavelength at three arbitrary points in NGC2261; measurements were made with a 10" aperture.	72
2.11	The variation in the measured polarization and position angle at R Mon with time using a 10" aperture; data from various sources (see text).	74
2.12	The variation of measured polarization and position angle with time at R Mon and the polarization knot in the V waveband.	75
2.13	The change in polarization with time at a distance of 5–20" North of the R Mon intensity maximum.	77
2.14	The change in polarization with time at a distance of 25–40" North of the R Mon intensity maximum.	78
2.15	The change in position angle with time at a distance of 5–20" North of the R Mon intensity maximum.	79

2.16	The change in position angle with time at a distance of 25–40′ North of the R Mon intensity maximum.	80
3.1	An intensity contour and polarization map of the R Cr A/NGC6729 cometary nebula from the 1990 V dataset.	99
3.2	An intensity contour and polarization map of the R Cr A/NGC6729 region close to R Cr A. (1990 V dataset).	100
3.3	An intensity contour and polarization map of the R Cr A/NGC6729 cometary nebula from the 1990 R dataset, together with a greyscale intensity image of the same region.	101
3.4	The variation of polarization with distance from R Cr A (along the “jet”) from north–east to south–west of R Cr A.	104
3.5	The variation of polarization with distance from R Cr A along a line east–west of the R Cr A intensity maximum (I_{\max}).	105
3.6	The variation of measured polarization at the R Cr A intensity maximum with aperture size.	107
4.1	An intensity contour and polarization map of the Cham-IRN in the I waveband. The origin is at the optical knot intensity maximum. . .	123
4.2	An intensity contour and polarization map of the Cham-IRN in the I waveband for the region close to the optical knot (the origin). . .	124
4.3	Greyscale intensity images of the Chamaeleon Infrared Nebula in the I waveband at different contrast and brightness levels. Note the jet-like structure in the bottom image.	125
4.4	A greyscale intensity image of the Chamaeleon Infrared Nebula in the R waveband. Note the western counterlobe separated from the main nebula body by a “gap” in the nebular brightness.	126
4.5	An intensity contour and polarization map of the Cham-IRN in the I waveband clearly showing the western jet-like feature.	128

4.6	Polarization profiles made along a line east–west through the optical knot intensity maximum (I_{\max}), using a measurement aperture of 3" in diameter.	130
4.7	The variation of measured polarization at the optical knot with aperture size.	131
4.8	The variation of polarization and position angle at the optical knot intensity maximum, using a 3" aperture.	133
A.1	R Mon/NGC2261 1989 V dataset.	150
A.2	R Mon/NGC2261 1989 R dataset.	151
A.3	R Mon/NGC2261 1989 I dataset.	152
A.4	R Mon/NGC2261 1990 B dataset.	153
A.5	R Mon/NGC2261 1990 V dataset.	154
A.6	R Mon/NGC2261 1990 I dataset.	155
A.7	R Mon/NGC2261 1990 $H\alpha$ dataset.	156

Preface

The contents of this thesis describe some of the work carried out by the author between September 1988 and August 1991, under the supervision of Dr. S.M. Scarrott in the Department of Physics at the University of Durham. This research was financed by a Science and Engineering Research Council studentship.

The bulk of the data presented in this thesis have been analysed and interpreted by the author. The author was present when many of the observations to collect these data were made. Some of the data described in chapter 2 were initially presented by Draper (1988) and were made available to the author for new analyses and interpretations.

None of the material contained within this thesis has been previously submitted by the author for a degree in this or any other university.

Chapter 1

STAR FORMATION AND COMETARY NEBULAE

*Hung by the heavens with black, yield day to night!
Comets, importing change and time of states,
Brandish your crystal tresses in the sky...*

William Shakespeare

Henry VI, I, i.

1.1 Introduction

It is now generally accepted that most, if not all stars, undergo a period of very energetic mass loss during their evolution onto the main-sequence. These mass losses are frequently characterised by the occurrence of massive bipolar outflows of cold molecular gas (see, for example, Lada 1985). Before any attempt can be made to study or discuss these outflows, or more particularly the properties of cometary nebulae which form the main subject in this work, a more general discussion of the whole star formation process must be undertaken. This is a consequence of the fact that, as will be shown, cometary nebulae are a visible signpost that star formation is in progress. In this chapter, a general review will be given of star formation as it



is understood today. **The Four Stages of Star Formation**, as entitled by Shu, Adams and Lizano (1987), will to some extent form a loose basis for the general structure of this review. We will discuss many of the phenomena which are seen as signposts of a continuing star formation process, before embarking upon a discussion of cometary nebulae which will be relevant to later chapters.

1.2 Phase One

It is generally accepted that the most active sites of star formation in our galaxy are located within giant molecular clouds, (GMCs). Such molecular clouds are often up to 100 parsecs in diameter, and have masses in the range of $10^5 - 10^6 M_{\odot}$ (Lada 1985, Shu *et al.* 1987). These clouds typically have temperatures of ~ 10 Kelvin. Any heating of the cloud due to cosmic ray action on the molecules is re-radiated in the form of CO emission which has a cooling effect, and thereby maintains the GMCs thermal equilibrium.

Observations of CO emission, for example, allow the GMCs to be mapped, and these observations have established that these giant molecular clouds are made up of a number of individual small clouds, or clumps. These smaller clouds have sizes in the range of 2–5 parsecs across, and masses in the range of $10^3 - 10^4 M_{\odot}$, Shu *et al.* (1987). It has been found that many of these subregions of the GMC contain higher density cores which have, for instance, been mapped in H_2 , CO, CS, HC_3N and NH_3 , Shu *et al.* (1987). How could these smaller cloud cores form within the larger giant molecular cloud? It seems likely that these clumps were formed by the action of a magnetic Rayleigh-Taylor instability. Such a process is discussed for example, by Shklovskii (1978), Mouschovias (1980), and in section 1.2.1 below.

The theory that cloud cores are the sites of low mass ($\leq 3M_{\odot}$) star formation is supported by the fact that such cores are often associated with many of the signs of star formation such as T Tauri stars (see section 1.4.3), and bipolar outflows, which will be discussed in greater detail later. The *Infrared Astronomical Satellite IRAS*, has discovered that $\sim 50\%$ of the known NH_3 cores have infrared sources associated

with them, which are identified as protostars, Shu *et al.* (1987). Dense clumps such as those located in the R Coronae Australis (see Chapter 3), and ρ Ophiuchi dark cloud regions, are good examples of these phenomena. Temperatures of cloud cores in the ρ Ophiuchi region have been measured in the 30–35 Kelvin range from CO emission. This heating is explained as coming from the friction between the particles in the GMC, in other words the ions and the neutral particles (neutrals). The increased density of the cloud core relative to the parent cloud increases the number of collisions between the ions and the neutral material, and thereby generates more heat. Examples of Zeeman splitting of thermally excited OH molecules, is further evidence for the existence of high density regions, since densities of over 10^3 cm^{-3} are required for this excitation to take place. The measured magnetic field along the line of sight has been measured as high as $125 \mu\text{G}$ in the case of the Orion A complex (Shu *et al.* 1987).

1.2.1 Cloud Core Formation

Before we discuss the formation of a molecular cloud core, let us consider an analogy using two fluids by way of clarification. These fluids are of unit volume, one of which is light and the other of which is heavy. The heavy fluid is placed on top of the light fluid, and experiences a gravitational force in the direction of the light fluid (see figure 1.1).

The interface between the two fluids is perfectly horizontal. Should any deformations form in the fluid interface, these deformations will grow in size as the heavier fluid protrudes down into the lighter fluid under the influence of gravity. (This would have the effect of reducing the energy of the system). This is the basis of the Rayleigh-Taylor instability.

The bulk of the material in a molecular cloud is electrically neutral. The ionized material, which may consist of electrons and charged grains as well as ions, is an electrically conducting medium which is coupled to the magnetic field which runs through the cloud; the field lines are said to be “frozen-in” to this material. The

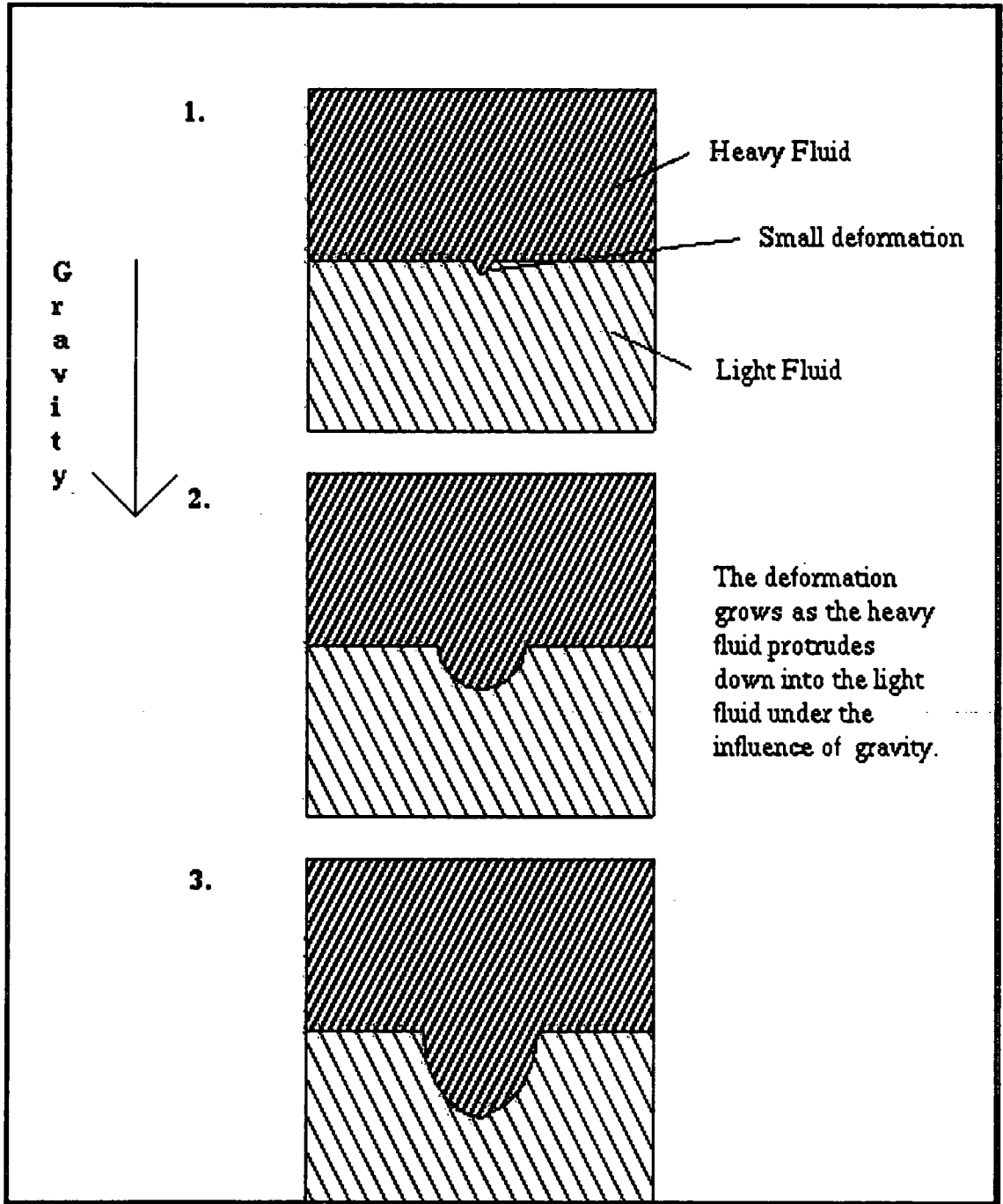


Figure 1.1: A diagram using the analogy of two fluids to help describe a Rayleigh-Taylor instability.

neutral material is not itself directly coupled to the magnetic field. The neutrals can only be affected by the field in so far as they are collisionally coupled to the ionized material. (Naturally, the probability of a collision between neutrals and ions increases as the density of the cloud medium increases). If no significant diffusion of the ions relative to the neutrals takes place within the lifetime of the cloud, then the magnetic field is said to be “frozen-in” to the neutral matter. Motion of the ions along the magnetic lines of force does not affect the magnetic field, but when the ions move transverse to the field lines they carry the field lines with them.

Now take the case of a frozen-in horizontal (galactic) magnetic field in the role of the light fluid, which supports some mass of gas (the GMC) which we will equate with the heavy fluid in figure 1.1. We now begin to discuss a magnetic Rayleigh-Taylor (or Parker) instability.

The molecular cloud has a strongly ionized component, and is thereby a conducting medium. (Cosmic rays are the most likely ionizing agent acting on the cloud material, though natural radioactivity may also be an ionizing agent). Under the influence of gravity the cloud experiences a force which pulls it towards the galactic plane. However, the molecular gas cannot move across the magnetic lines of force, since this would cause a bending of the field lines which would induce a force opposing the motion. Thus, the movement of the ionized gas towards the galactic plane would be halted, and the field lines would be in a state whereby they support the gas cloud. The only way in which the cloud could move therefore, is by sliding along the magnetic field lines.

Suppose now for some reason, (under the influence of some external force, a nearby supernova explosion perhaps, it doesn't really matter), that some small depression develops somewhere in the field lines. Under the influence of gravity, the molecular gas would slide down into this dip towards the galactic plane, in the same way that the heavy fluid protruded down into the light fluid due to the influence of gravity in the analogy. The mass of gas increases in the depression, and due to the increased weight, the magnetic depression deepens, and more molecular mass flows

into the ever deepening magnetic dip. The gas is unable to expand *across* the field lines, for this would mean the expending of energy, and it cannot move back *up* the field lines and out of the dip because of the opposition of gravity. Hence a localized cloud core begins to form, with a density somewhat larger than that of the medium from which it condensed. The magnetic dip deepens towards the galactic plane, until it reaches some maximum depth. At this point the magnetic field lines become so compressed that their elasticity eventually balances the weight of the molecular gas, and the formation of the molecular cloud core ceases.

1.3 Phase Two

Consider a molecular cloud which is rotating about some internal axis. For the cloud to be in a state of equilibrium, the cloud neither collapses inwards due to gravitational attraction, nor breaks up due to the centrifugal forces which are in evidence due to the cloud's rotational motion. In other words, at the equator, the force of gravity acting on the cloud is equal and opposite the centrifugal force. In this situation (assuming that no external forces are found to be acting upon the cloud), the cloud cannot begin to collapse, which is a necessity for the star formation process to begin. In this equilibrium state, the angular momentum that the cloud possesses is constant. If the cloud is to collapse, the rotational velocity of the molecular cloud must be slowed, and thereby angular momentum lost, in order that the gravitational force becomes the dominant force acting upon the cloud. In this situation it is said that angular momentum is prohibiting the cloud's collapse. It is possible for the angular momentum to be removed from the cloud in this situation, in a process which is known as magnetic braking.

1.3.1 Magnetic Braking

This is the process by which rotational energy is transferred from an object, in this case a molecular cloud, to its low density surroundings by means of the propagation

of magnetic disturbances. Much work has been done on this phenomenon. See for example the work of Mouschovias (1980).

Consider a molecular cloud is threaded by a uniform (galactic) magnetic field, which connects across the cloud boundaries into the uncondensed external medium, in the $\pm Z$ direction (see the top diagram in figure 1.2).

The magnetic field is frozen-into the molecular cloud, and the cloud itself possess some intrinsic angular momentum and thereby rotates about some internal axis. At some time later, the frozen-in field lines will have been twisted round due to the rotation of the molecular cloud. Such a twist will generate stresses in the magnetic field. Layers of material which are close to the molecular cloud in the external medium now find themselves pulled in the direction of motion of the cloud, and thus the external material gains some angular momentum. (This naturally assumes that the external medium will also have the magnetic field lines frozen-into it). Layers of material which are adjacent to these initially disturbed layers, now experience a similar force, due to the motion of the initially disturbed layers, and thus a rotational disturbance propagates away from the cloud in the $\pm Z$ directions, along the magnetic lines of force. This is illustrated in (the bottom diagram) in figure 1.2; (Z_f is the distance that the "magnetic front" has travelled away from the cloud core, and this defines the region which has been disturbed by enforced rotation).

Summing up, a rotational disturbance propagates away from the cloud due to the twist of the magnetic field lines, and this disturbance exerts a mechanical effect (enforced rotation) on the external material. Thus, this torsional wave removes angular momentum *from* the molecular cloud and transfers it *towards* the uncondensed external medium. The rotational energy of the cloud decreases, and the cloud rotation is said to be magnetically braked.

1.3.2 Protostar Formation

At some point in time, due to the effect of magnetic braking, the angular momentum of the molecular cloud is no longer large enough to oppose the gravitational collapse

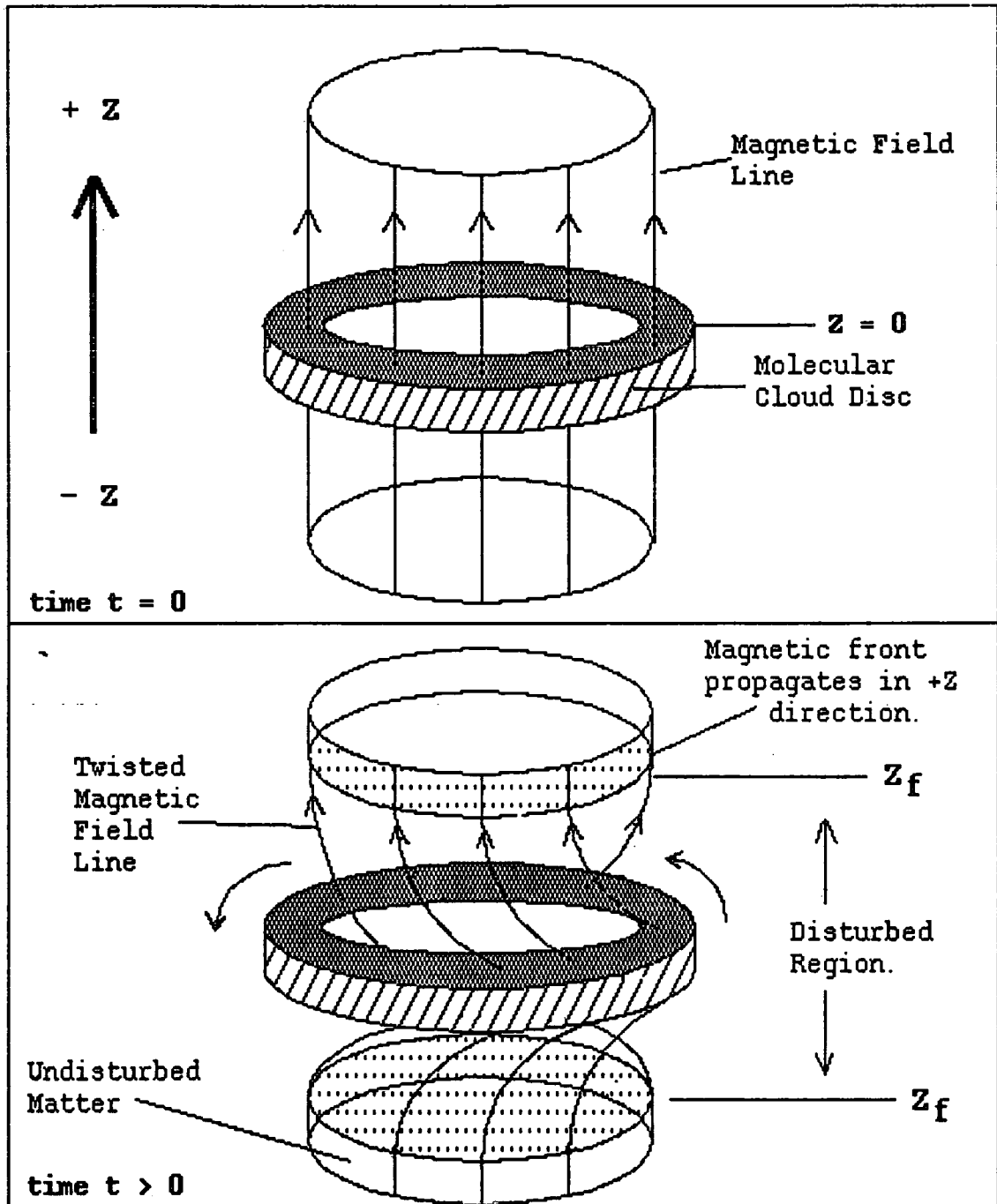


Figure 1.2: A magnetically braked cloud core. Adapted from Mouschovias (1980).

of the cloud towards the cloud core, and so the cloud collapses. (This assumes that any other forces which may help support the cloud have also been overcome. Such forces may be due to thermal pressures caused by particle motions for example). The density of a molecular cloud core varies as R^{-2} , where R is the radius of the cloud. Matter nearer to the cloud core experiences a greater gravitational force than matter further away, since the gravitational force also varies as R^{-2} . Thus matter nearer to the cloud core will be attracted first, and as the mass of the core increases, material further out will be attracted. The cloud is then said to be collapsing from “inside-out”, and the former cloud core becomes an accreting protostar whose mass is proportional to the initial mass of the molecular cloud from which it condenses. The mass of the protostar (M), is also given by $M=(\delta M/\delta T)T$, where T is the time, and $(\delta M/\delta T)$ is the rate of mass infall.

1.4 Phase Three

1.4.1 Evidence for Outflows

There is much evidence to show that young stellar objects undergo a period of massive energetic mass loss during their evolution towards the main-sequence. Kuhl (1978) has shown that in a survey of T Tauri stars (see section 1.4.3), 60% of the objects observed in $H\alpha$ and other emission lines showed a double peaked structure due to a blue-shifted absorption component. Another 5% of the T Tauri stars exhibited classical P Cygni profiles. The presence of the blue-shifted absorption features has been interpreted as evidence for steady mass outflow and stellar wind activity in these young stellar objects. Lada (1985) shows that in surveys of T Tauri stars, about 10% are observed to have molecular outflows associated with them, which together with other data leads him to suggest that only 10–20% of the pre-main-sequence lifetime of a young stellar object (YSO) is spent in the molecular outflow phase, which is about 10^5 years for a T Tauri star. Similar surveys of embedded infrared sources, reveal that almost 80% of the objects, were associated with molec-

ular outflow. The objects which yielded no evidence for molecular outflows were all visible sources, which may have therefore finished their molecular outflow phase, (see section 1.5). This observation, that an embedded infrared source (IRS), is more likely to be associated with molecular outflow than an optically visible YSO, has led many authors including Lada to conclude that “*the molecular outflow phase may be the earliest observationally identifiable stage of stellar evolution.*”

As the mass of the protostar increases due to accretion of the infalling cloud and disc material, a temperature will eventually be reached whereby deuterium burning will start. This eventually drives the object completely convective if the mass $< 2M_{\odot}$, and in the presence of differential rotation a dynamo effect will be generated, which will lead to a stellar wind. This wind, combined with the molecular winds, will eventually punch a hole in the placental envelope of dust and gas around the YSO to yield the observed bipolar outflows. This will happen in the polar regions where least resistance to the outflows is located. This does not, however, explain how or why the molecular outflows occur.

1.4.2 Theories of Outflow

As the rotating molecular cloud collapses down to form a protostellar core, a new problem is encountered. Through conservation of angular momentum, the accreting protostar and circumstellar disc contain the angular momentum of the initially collapsing molecular cloud. Since the radius of the protostar is very much less than the radius of the molecular cloud, the angular velocity of the protostar and the accreting material increases such that the evolution of the protostar by continued accretion cannot continue unless the angular momentum of the young stellar object is reduced. Magnetic braking can once again come into play to help reduce the rotational energy of the system (see section 1.3.1), in the same way that it reduced the angular momentum of the parent molecular cloud. The angular momentum can also be reduced if by some means the mass in the system can be decreased.

In recent times, the most highly favoured models for the removal of matter in the

vicinity of a young stellar object has come from work done on magnetically driven outflow mechanisms.

Relaxing Magnetic Twist

The model of Uchida and Shibata (1985, 1987) and Shibata (1987), argues that the large scale CO bipolar outflows that are seen to originate from YSOs, can be accelerated by the relaxation of a magnetic twist produced by the rotation of a forming circumstellar disc.

Part of the molecular cloud condenses to form an accretion disc rotating about a central protostar. A large scale magnetic field threads the disc, perpendicular to the plane of the disc, and is frozen-in to the disc material. Magnetic braking (section 1.3.1), due to the twist in the magnetic field lines, can slow the disc rotation somewhat, allowing material to move nearer to the star and thereby accelerate since the disc rotation is Keplerian. According to this model, the magnetic twist continues, and the twist accumulates near the surface of the disc. At some point the pressure build-up becomes so great that the magnetic twisting and the subsequent build-up in pressure cannot continue. When this happens the magnetic twist must relax, and a magnetic front propagates away from the disc (in the $\pm Z$ directions) accelerating disc material with it.

As material is removed from the disc, angular momentum is removed, (since the disc mass decreases), and bipolar outflows of molecular material are seen about a YSO, since the magnetic twist is likely to be symmetrical about the disc. There seem to be similarities between this model and the model which Draine (1983) has proposed to explain bipolar molecular outflows. The difference between these approaches is that in the Draine model, it is the rotation and subsequent twist of the field lines *from the YSO* that are the important feature, whereas with the Uchida and Shibata model, it is the rotation of the magnetic field *by the disc* that is the cause of the outflows. There seems to be no real reason why both models cannot operate simultaneously.

Centrifugally Driven Molecular Winds

In this model, Pudritz and Norman (1983, 1986) & Pudritz (1985), the molecular cloud collapses perpendicular to the magnetic field, which threads the accretion disc of the YSO. Once again, the magnetic field lines are assumed to be frozen-in to the underlying disc material, and a twist is caused in the field lines by the rotation of the disc. This action, (combined with the contraction of the cloud to form the disc and protostar), produces an “hourglass” configuration, where the field lines are “pinched” near the circumstellar disc, (see figure 1.3).

This is an important point, since the pinching provides the angle between the field lines and the plane of the molecular disc which is necessary if the disc material is to be centrifugally accelerated away from the disc along the field lines.

Matter in the inner part of the disc accretes onto the protostar, producing optical, UV and FUV radiation. (It is thought that this radiation from the accretion-shock provides most of the luminosity of a YSO during its outflow phase). The radiation produced then ionizes material at the protostellar disc surfaces out to large distances. The ionized material can then be expected to be strongly coupled to the magnetic field, and since it is forced to co-rotate with the magnetic field, and by the $\mathbf{J} \times \mathbf{B}$ force and centrifugal force, the matter is removed from the disc and accelerated along the magnetic field lines.

The outflowing material not only carries off its own angular momentum, but some of the angular momentum of the disc as well. This is an important point. Winds which are thermally driven alone will simply remove their *own* mass and angular momentum from the disc. In the Pudritz and Norman model, the matter which is accelerated away from the disc is still linked to the disc by the magnetic field lines. As a result, matter leaving the disc is able to exert a mechanical force on the disc as the field lines attempt to drag this ejected matter around. This slows the rotation of the disc and removes further angular momentum from the disc in addition to the ejected matter’s own angular momentum. Thus a hydromagnetic wind results, which is bipolar due to symmetry, and the disc is braked by the molecular outflow.

It must be noted that matter more deeply embedded in the disc is shielded from the ionizing radiation released during the accretion, so much of the disc mass, and thereby disc angular momentum, is unavailable for outflow. This model, like the others, is constrained by the degree to which the neutral material is coupled to the ionized material through neutral-ion collisions. If coupling is not efficient, then the field which is not frozen-in will simply slip through the molecular material. The nature of this model, whereby outflow is along the field lines, means that some degree of collimation is provided for the molecular outflows.

1.4.3 T Tauri Stars

It is now generally accepted that T Tauri stars are newly formed low-mass stars ($\leq 3M_{\odot}$), which have recently become visible in the optical range. They are emission line variable stars, and tend to occur in groups known as T-associations. Their position on the Hertzsprung-Russell diagram (HR diagram) is above and to the right of the main-sequence, and is therefore interpreted by many as an indication of their youth. (See the HR diagrams in Tayler (1978) for example). Bertout (1989) classifies T Tauri stars as a pivotal class representing the stage in stellar evolution between the deeply embedded low-luminosity sources which can only be studied at infrared and radio wavelengths, and the solar-type main-sequence stars. As such, T Tauri stars represent an important link in the understanding of pre-main-sequence stellar evolution. T Tauri stars are often associated with many of the signposts of star formation, such as jets (see section 1.4.5), and Herbig-Haro objects (see section 1.4.4).

T Tauri Criteria

T Tauri stars are usually defined according to certain optical spectroscopic criteria. See, for example, Strom, Strom and Grasdalen (1975); Bertout (1989), and Lada (1985). These spectroscopic criteria are as follows:

- Strong in Hydrogen Balmer lines.

- H and K lines in CaII.
- FeI, FeII, TiII, HeII emissions.

SII , and [OI].

- LiI absorption may also be strong.

[SII] and FeI lines are only visible in T Tauri stars with strong emission spectra. Their spectral classification is usually in the range of F to M. T Tauri stars are also characterised by other phenomena.

Emission Line Profiles Kuhl (1978) illustrated that of the T Tauri stars in his survey, some 60% showed a double-peaked profile in H α and other emission lines, due to a blue-shifted absorption component, which is interpreted as evidence for outflow from the YSOs. He suggests that the 5% of objects which show the classic P Cygni profiles are undergoing the last major outflow before a normal stellar wind take over. Another 5% of the T Tauri stars show an inverse P Cygni profile, and these are defined as a subclass of the T Tauri stars known as YY Orionis stars. The profile is interpreted as signifying the presence of inflowing matter. They are so named after the first YSO found to show this behaviour. Kuhl suggests that the YY Orionis stars represent the last vestiges of the accretion phase. In some cases, DR Tau for example, Balmer-line profiles have been observed to change from the classic P Cygni profile to an inverse P Cygni profile in a period of a few days, (Bertout, 1989). In one set of observations of YY Orionis lasting 14 days, Kuhl (1978) found that the star did not show the redward-displaced absorption component in 6 of the 14 days. What this implies is that complex mass motions are going on in the vicinity of T Tauri stars with a variable accretion rate in evidence. In all Kuhl concludes that 90% of the stars observed show evidence for a “combination of outflow and rotation as well as large-scale prominence and flare-type activity.”

Schwartz (1978) points out that molecular gas which may have been ionized in the circumstellar envelope should rapidly recombine and become neutral with increasing distance from the YSO. As a result, the bulk of the stellar wind is neutral, which Schwartz feels may account for the P Cygni absorption which is seen in most T Tauri stars.

The Variability of T Tauri Stars T Tauri stars have been found to be photometrically variable on all the time scales so far investigated. Rydgren and Vrba (1983) found that the T Tauri stars they investigated were variable over periods from ~ 2 –4 days. A number of researchers have looked at photometrically variable T Tauri stars, which are variable on time scales comparable to the stars rotational period. Bertout (1989) sums up this work, and finds that the rotational periods of many such objects are in the range 1–9 days. Both regular and irregular light variations are seen, which take place on the time scales of days to weeks. U-band variability has also been seen on a scale of 15 minutes. Many T Tauri stars also show some large-scale flare activity. Another related class, the FU Orionis stars are characterized by strong brightening, ≥ 5 magnitudes, over a period of perhaps months, and a decay in the order of months or even decades. The star V1057 Cygni was seen to undergo a 6 magnitude rise in a period of less than 100 days. A possible explanation for this flare-type activity is discussed later in this section.

An explanation for the periodic variations in the luminosity of T Tauri stars has been put forward by for example, Bouvier and Bertout (1989) and Bertout (1989). They explain the light variations as due to the rotational modulation of the light curve by groups of dark spots on the stellar surface of the object. The presence of these spots cuts down the amount of light being emitted by the stellar surface. Bouvier and Bertout explain these spots as the physical manifestations of the magnetic dynamo activity in the YSO. These phenomena are, perhaps, not too unexpected, since our own Sun also shows such sunspot activity. Sufficiently large spots lead to the rotational modulation of the stellar

light curve, since spots may be as large as 10% of the stellar surface! These spots are usually cooler than the surrounding photosphere by 700–1000 Kelvin. Bertout (1989) also goes on to say that hot-spots have also been found, which may be related to the accretion phenomena.

T Tauri stars have also been found to be polarimetrically variable. Serkowski (1969a) notes that in measuring the polarization of two stars, T Tauri and RY Tauri, a change in the polarization of 4% was found between his measurements and previous observations made by another observer 4 years earlier. Serkowski (1969b) also notes that the T Tauri star R Cr A changed its polarization by 9% in a period of only 5 weeks; (see chapter 3). Polarized source models have been used to explain the rapid change in polarizations that have been observed in T Tauri stars. For a discussion of this see chapter 2 on R Mon, and also later chapters. It is possible that the rapid photometric variability of T Tauri stars, and the explanation of this phenomena by Bertout (1989), may be strongly linked to the polarimetric variabilities which are seen.

IR and UV Excesses, and Discs T Tauri stars have been found to exhibit a wide range of both infrared (IR) and ultraviolet (UV) excesses. The infrared emissions have been found in observations between 2 and 100 μ m, (Cohen 1982). It is thought that optical and UV radiation emitted by YSOs is absorbed by circumstellar discs which are optically thick to their own thermal radiation. The dust grains then reradiate the heat as thermal emissions at IR wavelengths. Initial infrared excesses were reported by Mendoza (1966) for a number of objects. By far the greatest excesses in the observations of Mendoza were found for T Tau (6.2 magnitudes), and R Mon (8.5 magnitudes). Such observations also help to confirm that YSOs are surrounded by circumstellar discs. YSOs which are still at an early stage of formation and still have an envelope of infalling material around them from the “inside-out” collapse of the molecular cloud core, will also radiate at IR wavelengths for the same reason, (reradiation of optical or UV light at IR wavelengths) and may only be

observed as an IRS.

Data from the *International Ultraviolet Explorer (IUE)*, has shown that UV line fluxes are at levels of some $10^4 - 10^6$ times that of the Sun. It is generally thought that these UV fluxes are generated in an accretion shock. The region in which the disc reaches down to the photosphere must be hydrodynamically complex. As material is slowed to subsonic velocities it is thought that half the accretion luminosity is dissipated, and gravitational potential energy is converted into the internal of the gas and/or heat. The slowing of the rotational velocity of the disc material and the subsequent release in energy is what is explained as the accretion shock. It is also thought that "disc instabilities" may cause variations in the mass accretion rate which may explain the rapid outbursts seen for instance in FU Orionis stars, with a rapid mass accretion increase to $10^{-4} M_{\odot} yr^{-1}$, Bertout (1989).

Models of bipolar and cometary outflows from YSOs require some degree of channeling or collimation, which it is believed can be accomplished by a molecular circumstellar disc, (see for example Snell *et al.* 1980, and Cantó *et al.* 1981). Many authors have also made measurements in CO which confirm the presence of such molecular discs with radii of the order of 2000 AU.

Polarimetric data has provided indirect evidence for the existence of such circumstellar discs, where a band of parallel polarization vectors is found across a source. In recent times the observed polarizations were explained by extinction due to magnetically aligned grains, (see Gething *et al.* 1982 for example). Bastien and Ménard (1987) however, illustrate that grain alignment cannot account for the observed levels of polarization which are seen in many such objects. A more detailed discussion on this topic can be found in chapter 2, and most importantly on the topic of polarized sources. See also Gledhill (1991) and Scarrott *et al.* (1991).

1.4.4 Herbig-Haro Objects

Herbig-Haro objects (HH objects) are semistellar patches of nebulosity, which are located close to areas of star formation such as dark cloud complexes. These nebulosities are often seen in groups or knots, rather than simply as large patches of nebulosity. Herbig-Haro objects were first discovered in surveys in $H\alpha$ emission stars in dark cloud regions in the 1950's independently by Herbig and Haro, after whom these objects are named. Examples of the two possible types of object are HH7-11, which is a group of semistellar knots, and HH102 which exhibits a more nebulous form.

Spectral Characteristics

Herbig-Haro objects are characterised by their emission spectra. These are dominated by hydrogen Balmer line emissions and low excitation in [OI]; [SII]; [NI] and [FeII]. Moderate strength emissions are found in [OII] and [NII], with relatively weak emissions in [OIII]. (See, for example, Strom *et al.* 1975, Schwartz 1983). Early spectroscopic studies of HH1 showed many low-excitation emission lines which are rarely seen in nebulae, including [FeII], CaII and [NI].

Observations made using spectra taken in the [SII] doublet implied electron densities which were four times that indicated from spectra taken in the [OII] doublet, Schwartz (1983). This result was part of the evidence which was used in shock-wave interpretations of HH objects, (See later). Work by Schwartz also revealed the similarity between the spectra taken from T Tauri nebulae, and HH spectra. Infrared spectrophotometry of HH objects showed H_2 emissions in a number of objects, which had been shown to be consistent with shock-wave heating of molecular gas at densities of 10^4cm^{-3} , and a shock-wave velocity of some 15kms^{-1} (see section 1.4.4).

Even the brightest Herbig-Haro objects are found to be quite faint at ultraviolet wavelengths. Since HH objects tend to be located within dark cloud complexes, substantial extinction would be expected of the UV wavelengths, and hence the reason for faint UV emission spectra. Observations with the *IUE* found unexpected

emissions in CII and CIV, for example. Such emissions are indicative of high temperatures which are not evident in the optical spectra. Such spectra cannot be produced by scattering, and any theory which attempts to fully explain the HH phenomena would need to explain these emissions as well.

Radio continuum observations of HH objects indicate that the energy output from HH objects is a fraction of what would be expected if the whole volume of the cloudlet were excited, as would be expected in a HII region. The levels of energy which are found can be explained if only the surface layers of the objects were excited, which thus favours shock-wave interpretations which are able to explain this.

Proper Motions

Many Herbig-haro objects have been found to exhibit large proper motions. Cudworth and Herbig (1979) confirmed previous measurements on the objects HH28 and HH29, which yielded tangential velocities of $\sim 150\text{kms}^{-1}$ in a direction towards the South Galactic Pole. These authors also demonstrated that if the motions of HH28 and HH29 are extended backwards then they pass very close to the position of an embedded infrared source which was located in $2.2\mu\text{m}$ surveys, and is known as IRS5. It was thereby suggested that L1551 IRS5, which is in the Taurus region, is the exciting star for HH28, HH29, and for HH102 which is also located nearby. Snell *et al.* (1980) went on to confirm the relationship between IRS5 and the HH objects HH28, HH29 and HH102 in measurements made in ^{12}CO emission, by showing that the HH objects were associated with the blueshifted CO outflow lobe which is seen to the south-west of the embedded IRS5. A redshifted CO lobe was also seen by Snell *et al.* to the north-east of IRS5, and their measurements indicate that the two lobes extend for ~ 0.5 parsecs away from the embedded infrared source. Finding HH objects associated with a molecular outflow lobe from a YSO helps to show that HH objects are indicators of outflow phenomena. Snell *et al.* propose a model for this system, which can be applied to many such YSOs. In the model, the IRS is

embedded in a optically thick circumstellar disc, (which is viewed nearly edge on for this object). The double-lobed CO outflow structure arises from a dense shell of material which is swept up by a strong stellar wind from the IRS, with wind velocities of 200kms^{-1} which are channelled into two opposite streams. The velocity of the shell boundary is some 15kms^{-1} .

A very similar situation to that of HH28 and HH29 was also found for HH1 and HH2. The two Herbig-Haro objects were found to have tangential motions of up to 350kms^{-1} away from a 17th magnitude T Tauri star, which was found to be located between the two HH objects.

Measurements of the motions of the HH39 knots (see chapter 2), were published by Jones and Herbig in 1982. Their measurements were made from photographic plates taken between 1920 and 1931 of Hubble's variable nebula, NGC2261. One of the authors found marks on some of the negatives taken between 1920 and 1938, marking the position HH39, and it is postulated that these marks may have been made by Hubble himself. Presumably, the marks indicate the astronomers query that something interesting or odd is occurring in the data, since the patches of nebulosity appear to move with time. It is interesting to speculate that had more attention been paid to these phenomena at the time, then Herbig-Haro objects may have been discovered some years earlier.

The observed motions of Herbig-Haro objects away from embedded infrared sources, T Tauri stars, (and cometary nebulae for example), all seem to confirm that these phenomena are associated with young stellar objects, but are not themselves protostellar objects. As such, they are signposts to the star formation process.

Polarimetry

Polarization measurements and polarimetry has been an important tool in the understanding of Herbig-Haro objects. Strom, Strom and Kinman (1974c) made polarization measurements of the knots of HH24, which yielded values of up to 26%. Normals which were drawn to the polarization vectors of these knots cross at a point

which is nearly coincident with the position of a known infrared source (IRS). The results therefore indicate that the IRS is the main source of illumination for HH24.

A further excellent example of this technique is presented by Rolph (1990) and Rolph *et al.* (1990), for the case of HH83/Re17. HH83 is a nebulous object located near the L1641 dark cloud in Orion. A jet is seen running perpendicular to the major axis of the nebula, and an IRS was found close by on the jet axis, coincident with an *IRAS* source. Both the jet and the IRS are signposts of the star formation processes, as well as the nebulosity. Polarization measurements result in a pattern of polarization vectors which is typical of a simple reflection nebula. By drawing normals to the polarization vectors to identify the centre of the polarization pattern, the illuminating source can be derived. Rolph's results indicate that the illuminating source position is coincident (within errors), with the IRS source *IRAS05311-0631* (see figure 1.4).

Rolph also found that the jet was not polarized, which is an indicator that the jet is not illuminated by scattered light from the *IRAS* source, but is illuminated by emission. First impressions of a contour plot obtained from observations of HH83 might lead to the impression that the illuminator of the object is the star which is seen to be located at (0,0) in the polarization map (figure 1.4, which has been kindly provided by Chris Rolph). Polarimetry shows that the true illuminator is the *IRAS* source, and thus polarimetry is shown to be a powerful tool for the identification of illuminating sources. In figure 1.4 the centre of the centrosymmetric pattern of polarization vectors is shown, together with the IRS position. The initial classification of HH83 as a Herbig-Haro object came from the the classic HH emission lines that it was observed to have. The data of Rolph *et al.*, were able to show that the emission in HH83 comes predominantly from the unpolarized jet which lies on the axis of the reflection nebula, whilst the extended nebulosity is interpreted by Rolph *et al.* as the inside of a hollow cavity, the visible lobe of a bipolar nebula.

Other examples of HH objects which are associated with infrared sources, include HH6-10, which is coincident with a strongly variable IRS. The colours of the HH

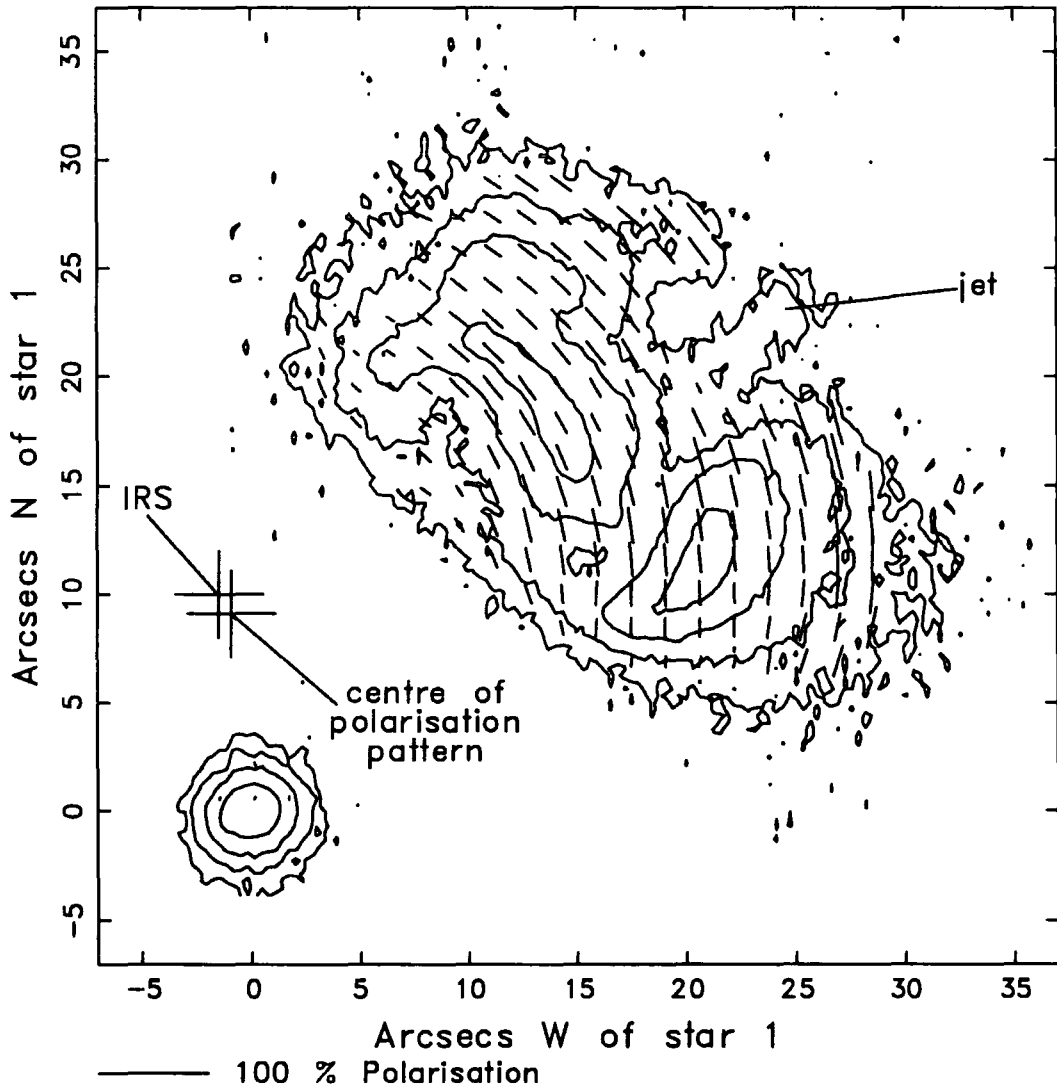


Figure 1.4: An intensity contour and polarization map of the HH83/Re17 nebula, (courtesy of Rolph 1990).

object are strongly reminiscent of a heavily obscured T Tauri star.

Most Herbig-Haro objects are observed in associations with the blueshifted lobe of a bipolar outflow. The reason for this is probably fairly simple. The redshifted lobe of a bipolar nebula is further away from us than the blueshifted lobe. It may also be the case that the redshifted lobe is pointing into a molecular cloud. As a result, the effects of this will mean that it is a lot more difficult to see HH objects associated with redshifted molecular lobes because of increased obscuration.

Models of Herbig-Haro Objects

All models of Herbig-Haro objects need to account for the emission lines which are found in spectroscopic studies of the objects. All the models account for the observed emission lines by considering shock-excitation of molecular gas. The models differ slightly though, in their approach. For example, Schwartz considers that the molecular gas of the HH object is what is excited, whilst Norman and Silk prefer to consider the shock-excitation of the ambient medium by the HH object.

- **Schwartz: The Shocked Cloudlet Interpretation** In 1978, R.D.Schwartz proposed a model to explain the Herbig-Haro phenomena, which is also reviewed and updated slightly by Schwartz in 1983 and 1985. The model was formulated originally following observations of HH1 and HH2, and considers a two component shock.

Schwartz considers a supersonic stellar wind from a pre-main-sequence YSO, which encounters a dense cloudlet in the ambient medium. This cloudlet is what will be identified with the HH object. The wind creates a luminous bow-shock around the front side of the cloudlet, initiating a high degree of excitation (a high temperature region), in the *surface of the cloudlet*, see figure 1.5.

At greater distances from the head of the shock, the bow wave is increasingly oblique to the surface of the cloudlet, and a lower temperature shock is produced over a larger area than the high temperature shock. A secondary

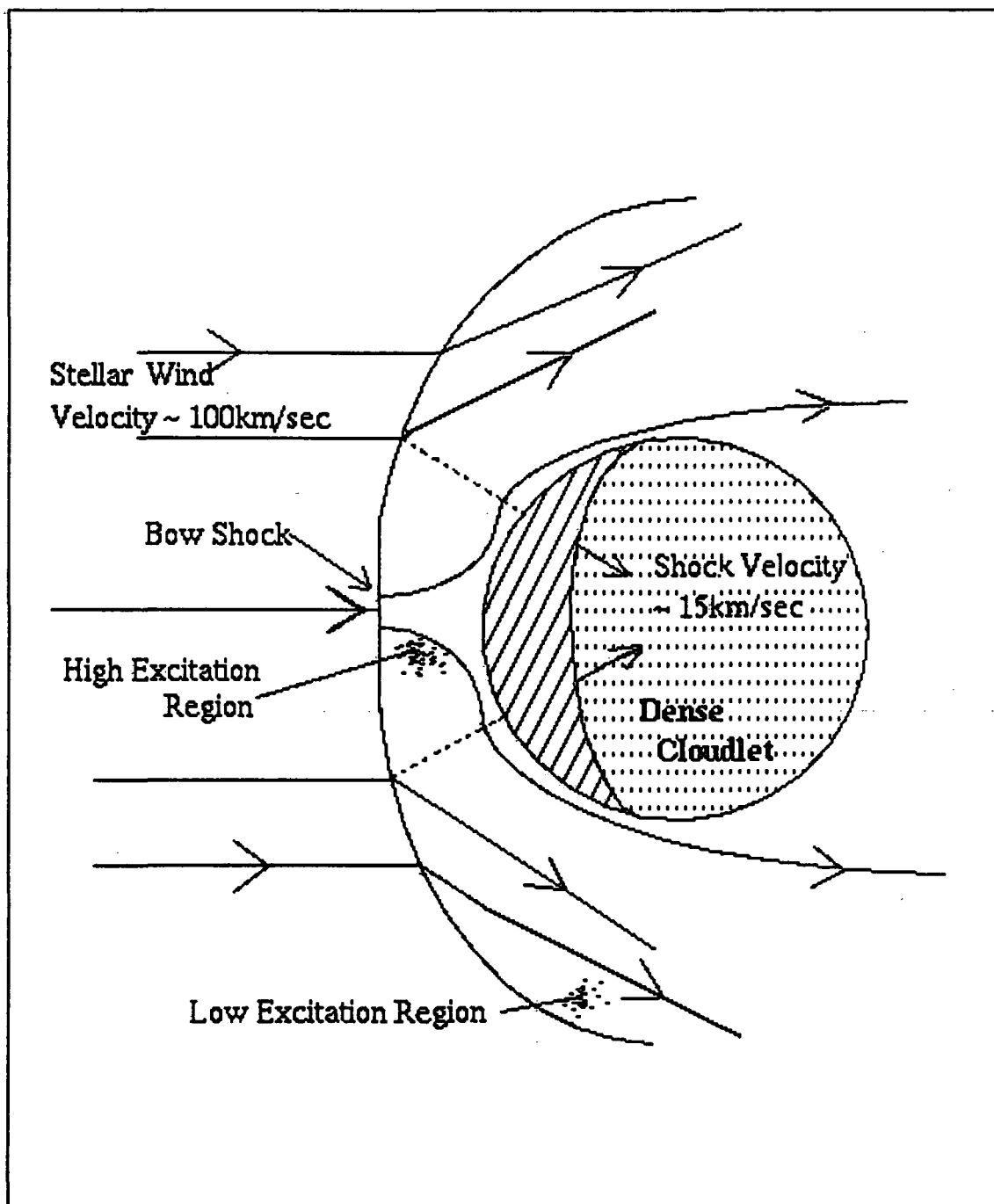


Figure 1.5: A schematic diagram which illustrates the main features of the shocked cloudlet model. Adapted from Schwartz (1978, 1985).

shock is propagated into the cloudlet by the ram-pressure of the post bow shock gas, on the front side of the cloudlet.

The bow-shock as the stellar wind encounters the cloudlet is where the kinetic energy of the wind is converted into the thermal energy of the shock. The high temperature excitation at the head of the cloudlet can produce temperatures of $\sim 3 \times 10^5$ Kelvin. Emissions from this region can produce the UV emissions which are seen in CIV, for example. The lower ionization region which dominates the optical spectrum, and which is from a larger area, is excited to temperatures of $\sim 10^5$ Kelvin. The secondary shock, Schwartz believes, is capable of producing the $2\mu\text{m}$ radiation due to the transitions of H_2 that are seen in some HH objects. Schwartz reveals that high radial velocities can be achieved by acceleration of the cloudlet by the stellar wind, with a shock velocity of $\sim 15\text{kms}^{-1}$, and a wind velocity of $\sim 100\text{kms}^{-1}$ for a cloud density of $\sim 10^4\text{cm}^{-3}$.

- **Norman and Silk: The Interstellar Bullet** Norman and Silk (1979) proposed a model which is in some ways the inverse of the shocked cloudlet model of Schwartz. In this model, clumps of material which may have been left over from the early stages of star formation, or may have been formed in a Rayleigh-Taylor instability (see section 1.2.1), are accelerated away from the source YSO by the ram pressure of the stellar wind. The cloudlets then plough into the lower density ambient medium, which becomes collisionally excited. The excitation of the *ambient medium* is then observed as the HH object. Norman and Silk termed this the “interstellar bullet” interpretation. In a similar way, Königl (1982) considers the acceleration of cloudlets and the subsequent excitation of the surrounding medium as an explanation for HH objects. In Königl’s model though, the acceleration of the cloudlet is by a jet which has been created by the focussing of the in stellar wind some way. A similar focussing mechanism to that proposed by Königl is discussed in the model of Cantó *et al.* below, whilst Königl’s explanation for chains of HH knots, such as

HH7-11, is to be found in section 1.4.5. One of the criticisms of the interstellar bullet model, by Schwartz (1983) for example, is that it bases the acceleration of the cloudlet on winds from a pre-T Tauri object. Schwartz in his criticism is able to go on to cite at least five *visible* T Tauri Stars (including T Tau and HL Tau), which are identified as the exciting sources for various HH objects. Applying the same basic technique to a T Tauri, rather than a pre-T Tauri star, should validate the models attempt to explain some HH objects though.

- **Cantó: The Interstellar Nozzle** Cantó *et al.* (1981) and Cantó & Rodríguez (1980), discuss a method of focussing a stellar wind. This model begins with a YSO embedded in a molecular cloud, and close to the boundary of the cloud. A molecular disc surrounds the YSO and channels the stellar wind into two opposite directions. The authors draw a distinction between the molecular interstellar disc required for such a channeling, and a “normal” circumstellar disc. The “normal” circumstellar disc has a size in the regions of a few thousandths of a parsec; the interstellar molecular disc is on the scale of tenths of a parsec.

There is a pressure gradient in the region of the YSO between the low density medium around the molecular cloud and the higher density cloud material. The result of this is that the molecular outflow from the YSO will expand in the direction of least pressure (down the density gradient), being collimated by the circumstellar disc which is itself a denser region. This produces an egg-shaped cavity along the axis of the disc (see figure 1.6), and not a spherical cavity as would be the case if the density of the material surrounding the YSO was completely the same in every direction.

Stellar winds then interact and shock against the walls of the cavity, and are refracted towards the tip, or focus, of the cavity. At this point a second shock of the molecular gas in the stellar wind occurs, which upon cooling radiates with the characteristic emission-lines of a Herbig-Haro object. Schwartz (1983)

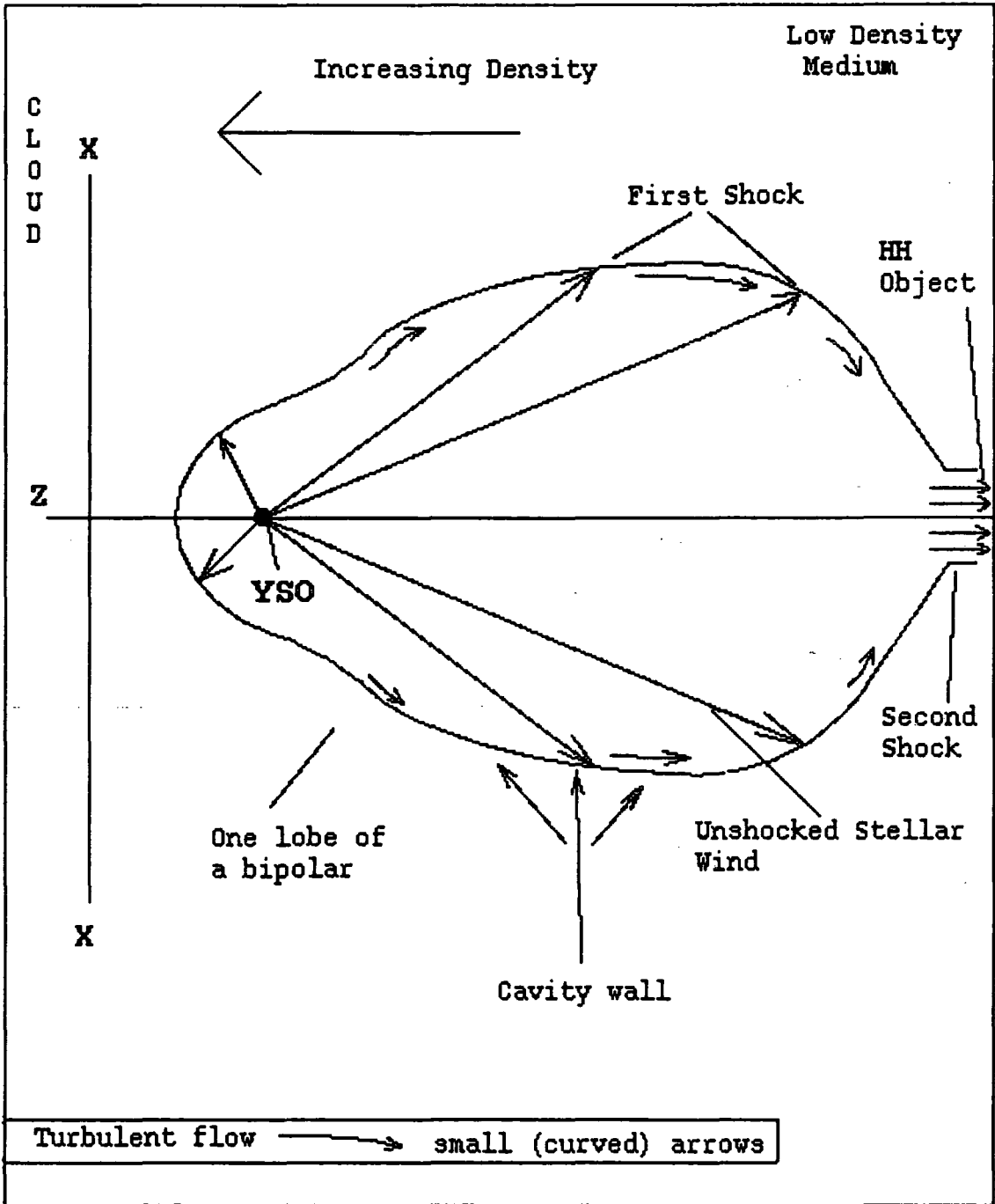


Figure 1.6: Schematic diagram illustrating the main points of the interstellar nozzle model for HH objects. Adapted from Cantó *et al.* (1980 & 1981).

comments that he finds it difficult to see how such a model can account for the degree of motion seen in some HH objects, and that on the face of it the point where the shock occurs, and therefore where the HH object is observed, should remain essentially fixed in space. Königl (1982) considers a similar situation to that envisaged by this model as part of a unified interpretation for molecular bipolar outflows from YSOs. He considers that an instability will occur under certain situations at the focus in the Cantó model, which will propagate the opening of a neck perpendicular to the elongation axis of the outflow, to form a nozzle which is able to maintain a supersonic collimated jet flow along the axis and away from the YSO.

Cantó *et al.* (1981) made similar observations to those of Snell *et al.* (1980), but in the vicinity of R Mon, where large CO outflows were located. A blueshifted CO lobe was found to the north of R Mon, and is associated with the fan of the cometary nebula NGC2261, whilst to the south of R Mon a redshifted lobe was found. The large interstellar molecular CO disc that surrounds R Mon channels the stellar wind, and the north collimated stream glances off a molecular cloud north-west of NGC2261, producing a focussed shock which radiates as HH39, (see chapter 2 and figure 1.6). Other molecular outflows have been found in ^{12}CO emission around many T Tauri stars.

1.4.5 Jets from Young Stellar Objects

One of the manifestations of molecular outflows, seen in many young stellar objects, is the optical jet. Sources which have jet-like structures associated with them include examples such as HH83, PV Cephei, R Mon, R Cr A, HH57, and HL Tau. Mundt (1985) puts the typical jet length at 0.01–0.2 parsecs, with opening angle of between $\sim 3 - 10^\circ$. The velocities associated with these outflows are typically a few hundred kms^{-1} . The stars driving the jets are typically T Tauri type stars or infrared sources, whose luminosities are usually in the range of $0.1L_\odot$ – $100L_\odot$. With the exception of R Mon (which has a luminosity of $1400L_\odot$), few sources have luminosities of greater

than $1000L_{\odot}$. Mundt (1985) though, points out that little effort has been made to date to find optical jets around more luminous objects, and so R Mon is not necessarily the exception to the rule. The spectral characteristics of jets have many of the features commonly associated with Herbig-Haro objects, which suggests that both jets and HH objects may in fact be strongly related phenomena, HH83 being the prime example. This is in addition to the fact that jets and HH objects are commonly seen together. Many jets are also observed to have knots or hot-spots associated with them, which are often catalogued as HH objects, such as the case of HH7-11.

The HH46/47 region is of the best examples of a highly collimated jet-like outflow. In this case the HH objects lie on a straight line with an optical jet and an IRS, which is believed to be the exciting source. Another excellent example is the HH7-11 region in NGC1333. Here a number of HH-like condensations are found in a chain almost equally spaced, and a line running through an IRS.

Models of Jets

As yet there is no universally agreed explanation for the jet phenomena, though many models have been put forward. In one interpretation, a thick circumstellar disc collimates outflow from a YSO, which is seen as an optical jet. Cantó *et al.* (1981) and Ward-Thompson *et al.* (1985), have both put forward such models to account for jets in the cases of different T Tauri stars. The interpretation of Königl (1982) is discussed briefly in section 1.4.4.

Königl goes on to consider a situation whereby a supersonically collimated outflow experiences a pressure change somewhere along its length. The result of this pressure change is to set up a series of oscillations which continue until the action of viscosity damps them out. The flow can then be seen as a stationary wave of compression and rarefaction along the jet as a result of the disturbance. The converging compression waves then form shocks, which, when the energy is dissipated, are seen as emission knots which may be catalogued as HH objects. HH7-11 in NGC1333 is

one example. Königl simply applies this explanation to one type of HH phenomena, that are seen in regular chains. A more general explanation by Königl of Herbig-Haro objects, is due to the acceleration of clumps of material by the ram-pressure of a jet, in a similar fashion to that explained in the shocked cloudlet model of Schwartz (1978, 1983 & 1985), and in section 1.4.4 above. Cantó & Raga (1991) have recently proposed the theory that part of the emission observed in high-velocity outflows from YSOs could be formed in the turbulent mixing of layers of the outflow. This turbulence could, they believe, contribute substantially to the emission from stellar-jets or Herbig-Haro objects.

Magnetic collimation of ionized molecular material is another possible explanation for jet collimation. In the same way that more general outflows can be explained by magnetic action, in the magnetic relaxation model of Uchida and Shibata (1985 & 1987) and the centrifugally driven wind model of Pudritz and Norman (1983 & 1986), (section 1.4.2), so perhaps, a more collimated outflow can occur in the form of an optical jet. One way in which this could occur is if only the inner-part of the circumstellar disc was responsible for a jet. In this situation, as the mass of the protostar grows, the inner part of the disc becomes Keplerian. (It is thought that instabilities in this disc may cause the FU Orionis outburst phenomena, due to runaway accretion of the inner part of the disc which begins due to the frictional heating of the outer envelope of the protostar). Winds from this inner disc would be relatively more collimated than winds initiated from the larger disc and would be perceived as a jet.

The focusing mechanisms which may be involved in collimating outflows from YSOs solve an important astrophysical problem. They alleviate the need for an unrealistically powerful stellar wind by focusing a large fraction of the stellar wind's momentum and kinetic energy. As an example Cantó *et al.* (1980), calculate that their interstellar nozzle approach would deposit ~ 300 times more energy to the HH object HH1 than would be expected from an isotropic distribution of the wind's energy.

An Optical Effect Interpretation In 1986, Cantó, Sarmiento & Rodríguez published a paper which proposed a completely different interpretation of the optical jet phenomena. These authors put forward a model to show that many of the elongated structures which are interpreted as optical jets are in fact the projection of the emitting walls of the bipolar cavity, which is created by the stellar wind in the surrounding molecular cloud. The interstellar nozzle proposed by Cantó *et al.*, and discussed in section 1.4.4, explains how the kinetic energy of the stellar wind from a YSO is thermalized in oblique shocks with the cavity walls. Upon cooling, these shocks radiate and present a spectrum similar to that seen in HH objects. The glowing walls of these cavities, when projected on to the plane of the sky parallel to the observers line of sight may then appear as elongated structures: jets. The structures themselves can be seen either by reflection of light from the YSO or shock excitation emissions, as well as a combination of the two as is found in many Herbig-Haro objects. The situation is strengthened if one limb of the YSO bipolar cavity is illuminated preferentially by the YSO. This could happen due to dust or clouds of material orbiting the YSO cast shadows on the outflow cavity, so that one limb is preferentially illuminated. (Shadow casting is discussed with respect to the cometary fan of NGC2261/R Mon, by Lightfoot 1989). Cantó *et al.* (1986) in this model, apply the hypothesis and attempt to model R Mon, R Cr A and PV Cephei, to name but three examples, with apparent success. The curved nature of many jet-like structures is seen as further evidence that this interpretation may be correct in some circumstances. The curved-jet would simply be the curve of the cavity wall.

It seems likely that some combination of all these jet models takes place. In some places a collimated outflow jet is observed, whilst in other situations the illuminated cavity edge is seen instead.

1.5 Phase Four

In the fourth phase of star formation, according to the definition of Shu *et al.* (1987), the stellar winds and molecular outflows widen the gap in the placental material which was initially formed in the polar regions. As time continues, the gap is widened over all 4π steradians by the stellar wind as material is cleared away. A low mass YSO is revealed, which has a remnant circumstellar disc surrounding it.

The star will eventually go onto the main-sequence as hydrogen burning begins, but this phase, and any phase which may come after it, is outside the scope of this work.

1.6 Summary: The Four Stages of Star Formation

Figure 1.7 illustrates the following summary of the four stages of star formation:

1. Slowly rotating cloud cores are formed out of a parent giant molecular cloud.
2. The cloud cores collapse from “inside-out”. This phase is characterised by a central protostar and disc deeply embedded within an infalling envelope of dust and gas. Material falling onto the protostar causes an accretion shock which provides the main luminosity for low-mass protostars.
3. A molecular outflow begins, which together with a stellar wind, breaks out along the rotational axis of the protostar. The physical manifestations of this phase are the bipolar outflows and collimated “jets” which are observed emanating from many YSOs.
4. The small gap created in phase 3 is eventually widened, and with time most of the remaining envelope of dust and gas around the YSO is blown away by the stellar wind, revealing a central T Tauri-like star, with remnant circumstellar disc.

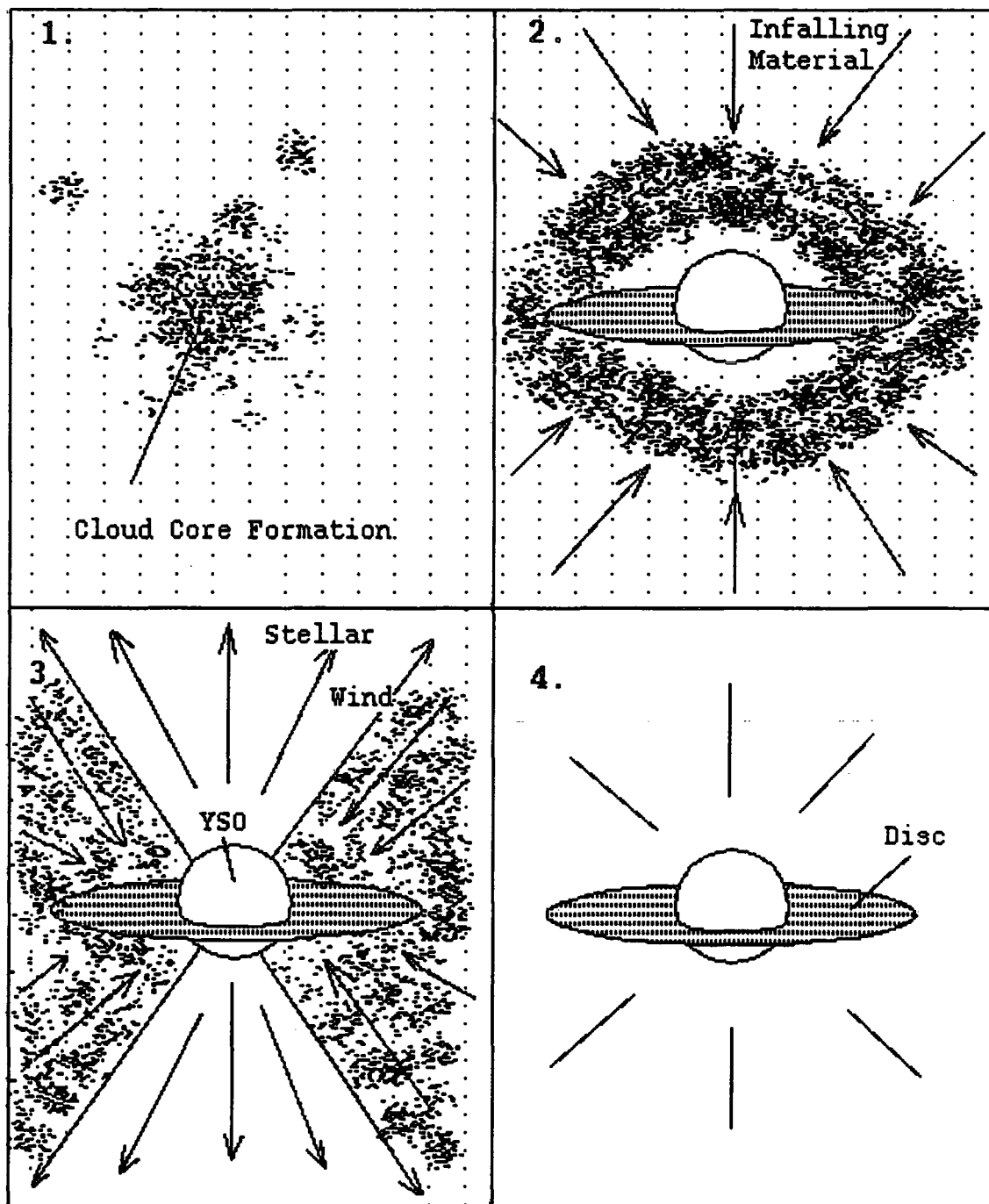


Figure 1.7: A diagram summarising the “four stages of star formation.” Adapted from Shu *et al.* (1987).

1.7 Cometary Nebulae

Now that we have examined the star formation process and the characteristics of each phase in the evolution of a YSO, we can look at cometary nebulae, which are young stellar objects undergoing their outflow phase (Phase Three in section 1.4). We will discuss the optical appearance of the outflows and see whether they are cometary or bipolar, but we must also look at the morphology of the molecular outflow as seen for example in CO emission, to give a more accurate definition of the outflow type. This will be done by looking at the optical classifications of Dibai (1971), and the molecular classifications of Lada (1985).

Cometary Nebulae, which are the main topic in this work, are so classified because their optical appearance strongly resembles that associated with their romantic celestial counterpart: the periodic or non-periodic comet. However, Dibai (1971) classifies cometary nebulae according to a much wider set of parameters. The morphological characteristics of the nebulous objects that Dibai calls “cometary nebulae” are given in the next section.

1.7.1 Dibai’s Classifications of Nebulosities

The following classifications of Dibai are depicted in figure 1.8.

1. *A globule with an emission rim and a central condensation containing a variable star.*
2. (The classical cometary nebulae). *Coned-shaped nebulae, which have a star at the apex of the optical fan.* One example is NGC2261. Dibai also classifies nebulae which are “not associated with stars”. It is not clear as to exactly what this means. Perhaps Dibai means that no exciting star is observed, as would be the case if a deeply embedded IRS were responsible for the illumination of the cometary nebula. As examples of cometary nebulae without associated stars, Dibai cites IC59, and NGC6729. This latter classification is certainly in error, for NGC6729 is clearly associated with the star R Cr A! Furthermore, evidence

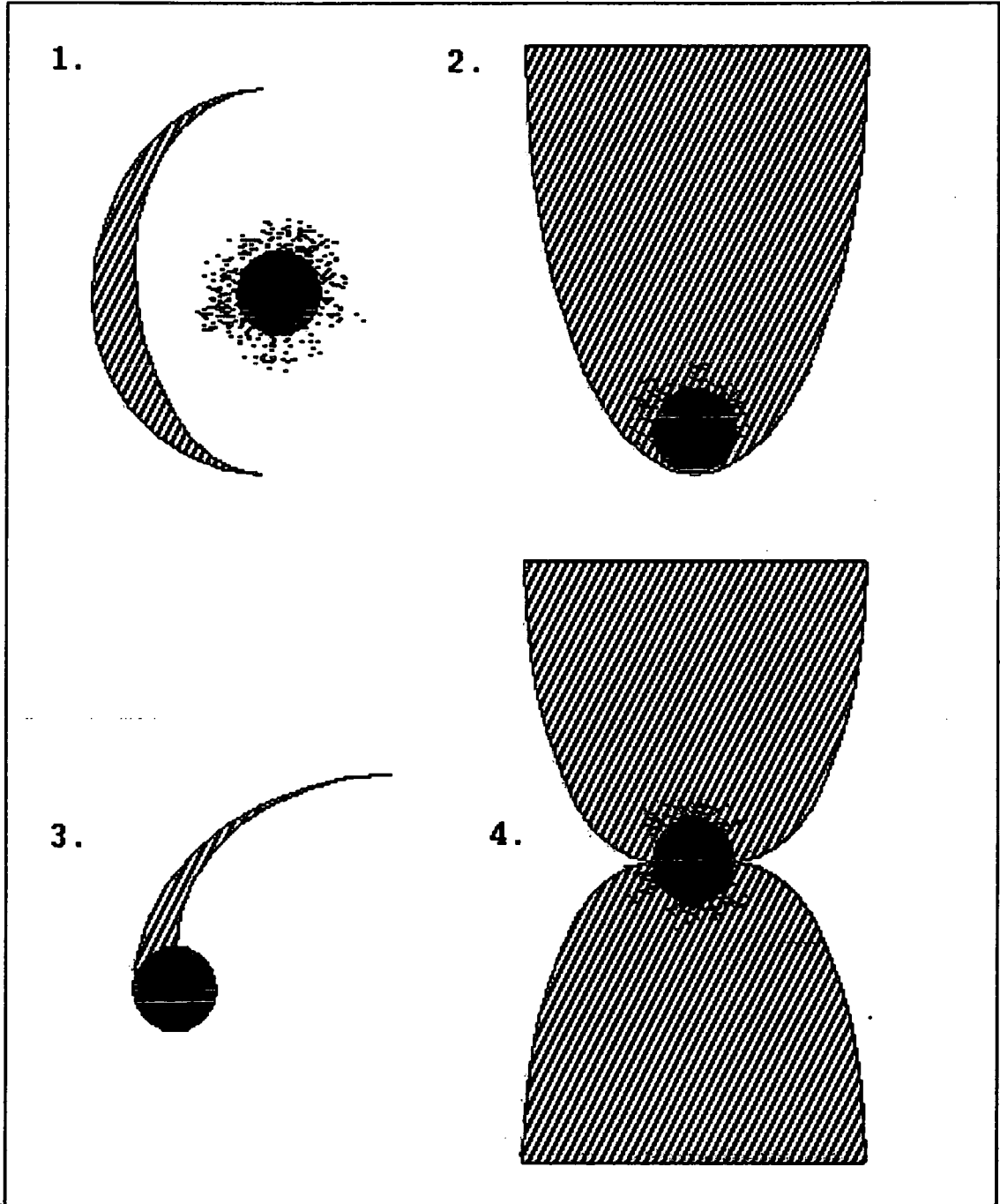


Figure 1.8: The nebular classifications of Dibai (1971). Shaded areas are nebulous regions; the black circle is the illuminating source.

Examples Of The Nebula Classifications of Dibai			
Type 1	Type 2	Type 3	Type 4
T Tau	Parsamyan 17	Lk H α -198	Lk H α -208
DG Tau	Parsamyan 18	RR Tau	Lk H α -233
HL Tau	Parsamyan 21	Z C Ma	HD44179
Lk H α -120	R Mon/NGC2261	SU Aur	Cham-IRN ?
FU Ori	R Cr A	Parsamyan 5	Hourglass in M8
HK Ori	Cham-IRN ?		S106

Table 1.1: Examples of objects associated with extended nebulae, using the classifications of Dibai (1971) & adapted from Cohen (1974). The relevance of the question mark is explained in the text.

such as that from polarimetry and spectroscopy proves beyond reasonable doubt that R Corona Australis is the main illuminating source for NGC6729, with T Cr A also making a contribution to the illumination of the nebula; see Chapter 3.

3. *A star connected with a bent, comma-shaped nebulosity.* One example given by Dibai is the “bright filament in NGC1999”.
4. *Biconical nebulae*, in other words bipolars, which have an hourglass shape. A central star-like condensation is to be found situated between the two lobes of the bipolar, in the “waist” of the hourglass.

Table 1.1 illustrates some examples of objects which fall into the classes defined by Dibai. Some of these examples are taken from Cohen (1974), whilst others are provided by the author.

Photographic images of Parsamyan 17,18, 21 and 22 can be found in Cohen (1974).

1.7.2 Lada's Classifications for Molecular Outflows

In 1985, Lada catalogued some 67 high-velocity molecular outflow sources. A source is termed high-velocity if the measurements (usually from CO surveys), indicate the gas velocities exceed 10kms^{-1} . Of these objects some 41 have been mapped in molecular outflow for which Lada classified the objects, where classification was in fact possible, according to three basic morphological types.

1. **BIPOLAR.** Lada noted that most of the objects in the catalogue fell into this category, in fact over 70% in all. These 30 sources are so termed because of their tendency to consist of two spatially separate lobes of emission, one consisting of predominantly redshifted gas, whilst the other is predominantly blueshifted gas. These lobes also have the tendency to be located symmetrically about a central star or embedded infrared source.
2. **ISOTROPIC.** 4 sources fell into this category. These sources are so named because they appear to have both redshifted and blueshifted gas originating in the same region of the sky.
3. **MONOPOLAR.** 7 sources in the list are termed monopolar. This name is applied to any object where only either redshifted, or blueshifted molecular outflows are observed. Lada further comments that the sources which earn this name have the tendency to appear elongated in the sky. One of these sources was later mapped using greater angular resolution than the original observations. The results showed that this source was in fact not monopolar at all, but bipolar in molecular outflow. The outflow mechanisms, magnetically driven winds and so forth, tend to have a symmetrical shape. As a result, it should be expected that most outflows will be symmetrical, with outflows extending away from the northern and southern polar axes of the star. It is not clear then, why there should be any sources where only one direction of outflow is occurring. Perhaps one possible explanation is that for some reason the density of the molecular cloud from which the protostar is evolving is

greater on one side of the object than the other. The greater density of the ambient medium in one direction would then inhibit outflow away from the protostar from one of the polar axes. Alternatively, and perhaps more likely, is the fact that there are no real monopolar outflow sources, and that the term merely refers to an optical effect caused by the poor degree of angular resolution obtained in the initial observations.

1.7.3 Cometary Nebulae: A Model

Levreault (1984) has proposed a model to explain the cometary nebula PV Cephei, which owes much to the model of Cantó *et al.* (1981) for the R Mon/NGC2261 complex. In Levreault's model, a circumstellar disc acts as a collimation mechanism, channeling the stellar wind from the YSO into two opposite directions. These streams then sweep up the molecular cloud material as the streams expand away from PV Cephei, which produces the observed high velocity gas that is seen in the vicinity of PV Cephei. Two roughly conical cavities are then formed, the closer (blueshifted lobe), of which has erupted through the front surface of the molecular cloud (see figure 1.9).

The circumstellar material has a greater degree of extinction than the material in the lobes, and so starlight from PV Cephei escapes preferentially into these cavities. Light is then scattered in the cavities, and into the observers line of sight, to produce the observed nebula. (The fact that light is scattered in the lobes means that the light will become polarized, which will be important in later chapters).

The orientation of the YSO and the nebula in the model above is such that one lobe is nearer to the observer. The redshifted lobe, which is tilted away from the observer, is also tilted *into* the molecular cloud from which the YSO originated. As a result, and since the blueshifted lobe has broken out of the molecular cloud, the blueshifted lobe is seen clearly, whilst cloud material will help to obscure the redshifted lobe. The degree to which an object will be tilted to the observers line of sight will naturally vary. Different molecular clouds will have different densities,

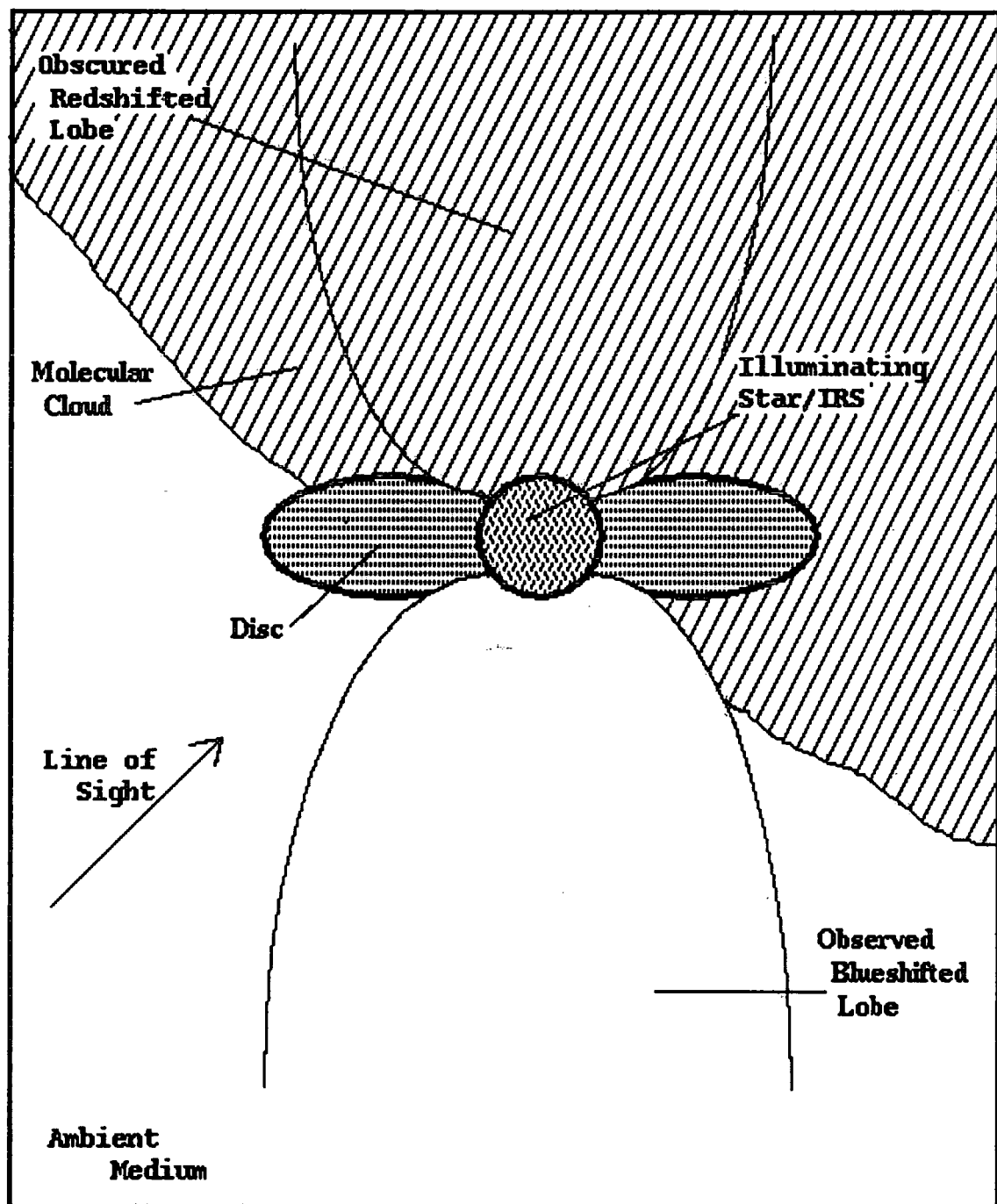


Figure 1.9: A schematic diagram depicting a bipolar nebula. One lobe of the bipolar is seen preferentially, and at optical wavelengths the object appears cometary in its morphology.

depending upon the elements which are to be found in the cloud. The greater the density of the molecular cloud, the greater the degree of extinction of starlight from the redshifted lobe will be. As a result, in some situations the tilt of the object, and the obscuration of one of the lobes by the molecular cloud, will mean that *optically* only one outflow lobe is observed. In some cases the degree of tilt may be such that the circumstellar disc also combines with the other factors to obscure the redshifted lobe. The net effect will be to yield an object, which in its purest form will reveal a nebulous fan extending away from a starlike condensation at the apex of the fan, with no obvious optical counterlobe. The nebula then takes on the optical form of the comet, with the fan of the nebula being compared to the tail of the comet, and the star-like exciting source being compared to the nucleus/head of the comet.

In the case of PV Cephei, Levreault (1984) has shown that a bipolar molecular outflow is indeed seen around the YSO, whilst Cantó has shown the same for the case of the NGC2261/R Mon complex, which Cohen (1974) has called the *prototype* cometary nebula. This confirms the hypothesis that cometary nebulae are simply bipolar nebulae, where one lobe is seen preferentially at optical wavelengths. Two further examples of nebulous objects which are optically classified as cometary, but which have been found to have bipolar outflows from observations of CO emission, are RNO15 and R Cr A, (Lada 1985).

Defining Cometary Nebulae

In this work, the reference to a nebula as cometary shall follow its *optical appearance only*. This is Type 2, in table 1.1. We shall make no further reference to the classifications of Dibai (1971), from this point onwards. As was discussed above, the orientation of a YSO undergoing a phase of energetic outflow is one of the important factors determining whether the appearance of the outflow optically can be defined as a cometary, or a bipolar. Consider an object which optically can be defined as a pure cometary, (no visible redshifted counterlobe). Then begin to tilt the object, so that the blueshifted lobe moves away from the observer, and the redshifted lobe

is moved towards the observer. The redshifted lobe gradually comes into view, and some point is reached whereby the angular extent of the original “blueshifted” lobe, is equal in extent to the original “redshifted” lobe. In other words, we have an optical bipolar nebula. The question is, for the purposes of classification, when does a cometary nebula become a bipolar nebula?

In the pure definition of a cometary nebula, no counterlobe should be seen by the observer. If we look at the Chamaeleon Infrared Nebula (Cham-IRN), then a small counter-lobe can clearly be seen. (See chapter 4). According to any purist’s definition, this would mean that the Cham-IRN would have to be defined as a bipolar nebula. However, the extent of the eastern optical fan is so great relative to the western counter-lobe nebulosity, that this object should still be defined as cometary in form; (thus the question mark in table 1.1). Hence, cometary nebulae can now be redefined as follows: a cometary nebula is so classified where the optical appearance of the nebulosity is such that the extent of the optical fan far exceeds the extent of the counter-lobe, and the general appearance of the comet still remains.

1.8 Summary

It is clear that there are many signposts that the star formation process is occurring, such as HH Objects, infrared sources and molecular outflow regions. Molecular outflows would be expected to be bipolar in form due to symmetry and when the circumstances arise these outflows will appear cometary in form at optical wavelengths. As a result cometary nebulae are themselves a signpost that star formation is occurring and the study of such nebulae will hopefully yield a better understanding of the star formation process.

Chapter 2

THE POLARIZATION OF R MON/NGC2261

2.1 Introduction

Since Hubble's classic paper on the variability of the Cometary Nebula NGC2261 and the associated variable star R Monocerotis in 1916, a plethora of studies upon the object, including photometric, spectroscopic and polarimetric observations, have been undertaken. The striking structural variations that the nebula is seen to undergo from time to time have been interpreted by many to be due to variations in the illumination of the nebula by the star R Mon, as was hypothesised by Lampland (for example) as far back as 1926, quoting also the previous work of Slipher. This theory is strengthened by the fact, as Lampland points out, again referring to the work of Slipher, that the "*nucleus and the outlying nebulosity have the same spectrum,*" which yields the interpretation that the "*fan-shaped*" nebula, as Herschel, (who discovered it in 1783), described it, shines by reflected light from R Mon. Polarimetric observations by Gething *et al.* (1982) and Warren-Smith, Draper & Scarrott (1987b), for example, confirm this hypothesis, due to the centrosymmetric pattern of polarization vectors found in the nebula, the normals to which indicate R Mon as the illuminating source.

Ménard *et al.* (1988) quoting other authors, reveal that R Mon is ~ 800 pc away,

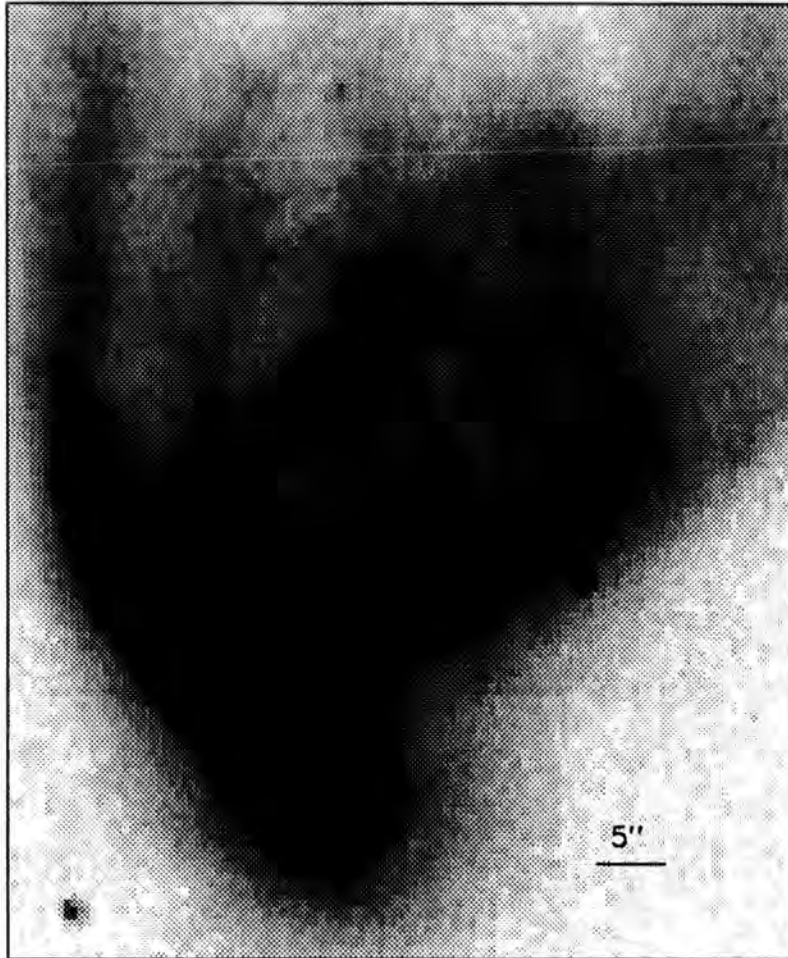


Figure 2.1: A greyscale intensity image of Hubble's variable nebula. Data was taken in 1988 in the I waveband on the INT.

and has a luminosity of $1400L_{\odot}$, whilst Beckwith *et al.* (1986) have also speculated that R Mon may have a mass as great as $5M_{\odot}$. R Mon $\alpha = 6^{\text{h}}36^{\text{m}}24^{\text{s}}$, $\delta = +8^{\circ}46'0''$ (1950), is a pre-main-sequence star, the spectral type of which has been the subject of much debate. Cantó *et al.* (1981) point out that there is, in fact, no consensus on the spectral type of the object. Joy (1945) classified R Mon with a group of T-Tauri stars as being in the range F5–G5 with emission lines resembling those of a solar chromosphere. Mendoza (1966) says that no normal stellar spectrum was seen. Herbig (1960) provisionally classified R Mon within a group of B or early A stars. Herbig (1968) goes on to say that there is no convincing evidence in the spectrum of R Mon of the presence of a G- or K- type star, and that when R Mon rose to almost a 10th magnitude star in 1946, the spectrum was superficially like that of an A-type supergiant, but the extreme sharpness of the high balmer lines suggested to him a shell. The total luminosity is found to be 60 times that expected from the visual absolute magnitude, (an infrared excess). This has been attributed to the rethermalization of light from a heavily obscured G–K star by Low and Smith (1966).

Lampland (1931) discusses the apparent progressive displacements of various parts of the nebula, after observing NGC2261 from 1916 until 1931. He describes how the same parts of the nebula are seen to be veiled, greatly dimmed, or completely obscured, and finally reappear later in the same position and with the same form and brightness as recorded on photographs taken in earlier years. Some of these apparent progressive displacements of boundaries of obscuration, he reveals, were measured with rates of motion as high as $0.25''$ per day, and the motions of these patterns were always away from R Mon, indicating again that the changes in the nebula were due to changes in the illumination arriving at the fan from R Mon. The motions of some of the structures seen would imply a velocity across the nebula of greater than the speed of light, as Lightfoot (1989) has pointed out, which is clearly impossible. Lightfoot, in his paper, has published some interesting work detailing possible ways in which shadowplay within the nebula results in the observed phenomena. Similarly,

Bellingham and Rossano (1980) conclude that the variations observed in NGC2261, and indeed in R Cr A and T Cr A, are due to variations in the diffuse envelopes or circumstellar shells surrounding the underlying stars.

Lampland took some 237 photographic plates over an interval from 1916 to 1948, at The Lowell Observatory, of R Mon. Lampland and Ashbrook (1949), analysing these plates, measured a change in the amplitude of R Mon of some 2.5 magnitudes over this period. They talk of an *erratic flickering*, with a cycle length of the order of a few weeks accounting for a few tenths of a magnitude, whilst a larger fluctuation of about one magnitude occurs over a period of one year. Bellingham and Rosano, discussing the long period variations of such variable T Tauri-like stars, and using Lampland and Ashbrook's data, deduce that there is a "hint" of a 1500 day variation in the brightness of R Mon. More obvious, they say, is a variation of about 8000 days in length and 0.5 magnitudes in amplitude, which is superimposed upon a linear increase in brightness of about 0.75 magnitudes over the period of the observations. Hubble (1916) reported that R Mon has been seen to vary in brightness between 9.5 and 13th magnitude.

Cantó *et al.* (1981) made observations of R Mon and the NGC2261 complex, in ^{12}CO . They concluded that R Mon was located at the centre of a disc-shaped molecular cloud, and that the stellar wind from R Mon has created a bipolar cavity within the cloud. The presence of blueshifted and redshifted components in the ^{12}CO observations further suggested to the authors that NGC2261 is the northern lobe of a bipolar nebula, where the southern lobe is obscured by the tilt of the molecular disc. The size of this molecular disc is calculated to be $\sim 0.8\text{pc}$ in diameter, and $\sim 0.4\text{pc}$ in width, and has a mass of $\sim 30M_{\odot}$. They calculate a mass loss rate from the R Mon as $\sim 1.4 \times 10^{-8}M_{\odot}$ per year, using a wind velocity of 200 km s^{-1} . The molecular cloud/disc density is relatively low, with a calculated value of 2000cm^{-3} , which is consistent with the non-detection of NH_3 , for example, in the molecular cloud. The relatively low density of the cloud means that R Mon suffers little extinction at infrared wavelengths. Sato *et al.* (1985) show an interesting diagram of

the R Mon/NGC2261 system, which helps to show how the tilt of the nebula with respect to the observer, combined with the obscuration of the southern redshifted lobe by the molecular disc/cloud, creates the cometary nebula. A discussion on the appearance of such nebulae is given in section 1.7.3.

Many pre-main-sequence objects have Herbig-Haro objects (HH objects) associated with them, (see section 1.4.4), and R Mon is no exception. HH39 is located some 7.5 arc minutes north of R Mon, (~ 1.4 parsecs from R Mon), and is a series of HH-like knots. Brugel, Mundt and Bührke (1984) have proposed that a collimated jet of material flows directly up the axis of the nebula and shocks into clumps of material at the position of HH39 at high velocities, thus producing the HH objects. The conclusions of Brugel *et al.* are based upon the detection of emission lines in the nebula. A similar explanation for HH39 to that of Brugel *et al.* (1984), was reached by Cantó *et al.* (1981), but in the model of Cantó *et al.* it is a focused wind rather than a jet which is the responsible for the excitation of the gas which manifests itself as HH39 (see section 1.4.4). Jones and Herbig (1982) measured the velocity of the knots and found them to be clustered about a mean of 290kms^{-1} , (though one had a velocity of only 60kms^{-1}). These authors also confirmed that the knots of HH39 had a motion away from R Mon and NGC2261.

Walsh and Malin (1985) have shown that some of the knots within the HH39 association vary in brightness, and that a faint loop of material connects the HH39 region to the eastern arm of NGC2261. The detection of the loop has been suggested by Walsh & Malin to signify a cavity with the HH objects at its tip, where shocked wind flows along the walls of the outflow cavity (which is consistent with the Cantó *et al.* model). Walsh & Malin have also detected a faint jet-like nebulosity to the south of R Mon. It was suggested by Warren-Smith, Draper and Scarrott (1987b) that this feature is the western rim of the optically obscured southern (redshifted) counterlobe of R Mon. This counterlobe would then correspond to the redshifted CO outflow already detected by Cantó *et al.* (1981). Warren-Smith *et al.* (1987b) found this feature to be polarized to levels of 30%–40% which is consistent with the con-

clusion that the feature is mainly seen by reflected light from R Mon. The position of the jet-like feature did not change in the time period between the observations of Warren-Smith *et al.* (1987b) and earlier observations made by Gething *et al.* (1982). Since the rim of the redshifted lobe would not be expected to move with time either, these results are therefore additional evidence that the model proposed by Cantó *et al.* (1981) for R Mon and adapted for explaining PV Cephei by Levreault (1984) is correct, (see section 1.7.3).

Multicolour imaging polarimetry of this cometary reflection nebula will be described, and an interpretation of the data will be presented. It will be shown how the new data presented here, and in many ways more importantly the way in which the data itself is analysed, is of critical importance in explaining the polarization results. The conclusions that will be presented herein, will hopefully yield a better understanding of this object, and may aid the understanding of similar objects.

2.2 Observations

2.2.1 The Aquisition of Data

Observations were made of R Monocerotis and the nebula NGC2261, over a period of 3 nights from January 27th to January 29th 1989, by observers including the author. This was done at the f/18 Cassegrain focus of the 1 metre telescope of The Mount Stromlo and Siding Springs Observatory, at Siding Springs in New South Wales, Australia. The Durham Imaging Polarimeter was used, Warren-Smith (1979), Scarrott *et al.* (1983), Draper (1988) and Rolph (1990), with a GEC coated CCD as a detector, to take a total of 40 CCD images in 5 wavebands, B, V, R, I and Z, with a total exposure time over these 40 images of 9120 seconds. The FWHM seeing experienced during the time obtaining these images was $\sim 2-3''$, whilst the combined FWHM seeing was slightly better than $3''$, (some $2.8-3''$). Other images also taken during the same observing run but on later nights in these wavebands were rejected from these analyses due to the poorer seeing conditions prevalent at

the time these observations were made. Observations were also made over 3 nights, from 23rd February 1990 to February 25th 1990, at the f/15 Cassegrain focus of the 1 metre Jacobus Kapteyn Telescope on the island of La Palma in The Canary Islands. 28 CCD images, in B, V, I, H α and continuum, were taken with a total exposure time of 7840 seconds. The FWHM seeing, was 2.3" or better for the duration of the observing run. The combined seeing was 2.8" or better, for all the datasets except the continuum. The continuum data experienced a small focus error and as a result, the continuum has been neglected from the main analyses of R Mon and NGC2261. (See section 2.3.2).

In addition to these datasets, an investigation was carried out to reanalyse all the data previously reduced by Draper (1988), which includes data taken over a period of 7 years from 1979 to 1986. Draper's datasets were resampled and realigned to a common reference image which had been used previously in the reduction of all the 1989 and 1990 data by the author. This was to enable all the data on R Mon which had been gathered by the Durham Polarimetry group, to be compared more easily with each other. The data used at this point in the investigation came from a variety of sources. Included are datasets from 1979 taken at the f/13.5 Cassegrain focus of the 1 metre George and Florence Wise Observatory Telescope in Israel, with an electronographic camera as a detector, and again using The Durham Polarimeter. This dataset provided an initial interpretation of R Mon for Gething *et al.* (1982). Data were also taken on the 3.9 metre Anglo-Australian Telescope in 1981, again with an electronographic camera, and at The Wise Telescope with a CCD as a detector, over a period from February 1985 to March 1986. For a fuller description of these datasets, see Draper (1988). The next dataset to be looked at was taken in March 1988 in the I waveband at the f/15 Cassegrain focus of the 2.3 metre Isaac Newton Telescope (INT), on La Palma. This dataset was originally reduced by Draper but never published, and has been considerably reanalysed by the author for the analyses detailed. These INT data comprise 20 CCD images, taken with a combined exposure time of 2920 seconds. A FWHM seeing of less than 0.9" was

experienced for the data taken with the INT. The data produced a combined seeing of better than $1.7''$, when all the CCD images taken during observing were merged together.

Finally and more recently, some observations were made at the f/11 Cassegrain focus of the 4.2 metre William Herschel Telescope (WHT). For investigations centred on the region close to R Mon, just 4 CCD images were used in reductions by the author, taken in the V waveband on the night of the 19th January 1991. Each CCD image had an exposure time of 30 seconds. The combined FWHM seeing was some $1.7''$. The image scale of the reference image used in the alignment of all the data was $0.482''$ per pixel.

For a set of measurements to be made, a set of at least 4 CCD images must be taken at different half-waveplate positions. A description of this procedure is given by Warren-Smith (1979). The exposures taken usually include short exposures to record details from R Mon, (and also without the possibility of any saturated pixels), and longer exposures to ensure that detail from the nebula is recorded. The R waveband obtained in 1989 though experienced some slight saturation at the R Mon intensity maximum, and no other unsaturated exposures were made. As a consequence of this no measurements were made at R Mon itself in this dataset, but measurements were possible elsewhere in the nebula. The programs of Warren-Smith allow synthesised apertures to be placed upon polarimetric data. This aperture polarimetry will be used throughout, when measurements at specific points are to be made.

2.2.2 The Importance of Seeing

The whole discussion of the microstructure of R Mon is greatly affected by the seeing. When the data presented here are compared to the data originally presented by Draper and Gething *et al.* as well as the data taken on R Mon going back as far as 1964 by other authors, it must be remembered that different seeing conditions would have been in evidence at the time each of the observations were made. Any

comparison between the results obtained with different datasets must always bear this in mind. Any author will naturally always attempt to present the data which has been taken in good seeing, and indeed this author has rejected any data which was taken in very bad seeing. Since, of course, most of the previous authors have used aperture sizes of greater than 10", this limits the effect that seeing will have upon a measurement, since the aperture size is much larger than the seeing disc. Of course, the very use of this large aperture size makes any differentiation between different features in the microstructure centred upon R Mon impossible. It will also be shown later how the use of such a large aperture yields incorrect values for measurements made upon R Mon, due to the inclusion of different features within the aperture. However, observations made within the cometary fan of NGC2261, where measurements do not change radically over a distance of a few arcseconds, are not as susceptible to the problems of poor seeing as measurements taken around R Mon.

In analyses which explore the microstructure of R Mon, the image scale of the telescope used in obtaining the data will naturally also affect the data. All the data acquired by the Durham Polarimetry Group since 1989 on this object has, as was discussed earlier, been aligned to a common reference image. The job of aligning all this data, taken on different telescopes with different image scales and different seeing conditions, has at times, been non-trivial. Most of the data taken was obtained on 1 metre telescopes, the JKT, the MSSSO 1 metre, the Wise Observatory. Three datasets though, were obtained on larger telescopes, namely the INT, the AAT and the WHT. Investigations involving the microstructure of R Mon should preferably be made using the larger image scales found on the larger telescopes. However, good seeing is also a requirement. If data is collected on a small telescope in good seeing, then it is likely that this will be better than the collection of data with a larger telescope in bad seeing. In other words, both image scale and seeing are important in such analyses.

The worst combined seeing that was experienced, in any of the datasets used in

obtaining the measurements to be detailed, was less than $3''$. Measurements made upon the data never used an aperture size of less than $3''$ in size as a result of this.

2.3 Results

2.3.1 Polarization Maps

Linear polarization maps made from the data taken in the 1988, 1989 and 1990 observing runs are presented in figure 2.2 and figures A.1 to A.7.

Polarization calculations for these maps were made with a bin size of 9 pixels square ($4.3''$ square) moved in steps of 7 pixels. The main body of NGC2261 shows what seems to be a classic and regular centrosymmetric pattern of polarization vectors, with a centre of the pattern located at R Mon. This pattern is typical of many reflection nebulae which are illuminated by a point-like source, which in this case is R Monocerotis. As has been noted by other authors, there are deviations from the centrosymmetric pattern as we approach the intensity maximum of R Mon, and this has long been attributed to the presence of circumstellar disc surrounding the illuminator star. Here a band of vectors is seen across the illuminating star R Mon. The orientation of this disc surrounding R Mon is defined by the position angle of the polarization vectors measured (in such interpretations) when an aperture measurement is made at R Mon. It is also interesting to note that on either side of the polarization disc null points are found, where the polarization effectively falls to zero. These null points are more clearly seen in some of the data presented here. A good example is the map presented here taken in the V waveband at the end of January 1989 (see figure 2.3).

The bin sizes used in this close up of R Mon were 7 pixels ($3.4''$) square, and the bins were moved on by the same amount for each subsequent polarization measurement. At points $\sim 17''$ west and $\sim 10''$ east of the intensity maximum of R Mon, the polarization is seen to fall off to zero, and these are the null points.

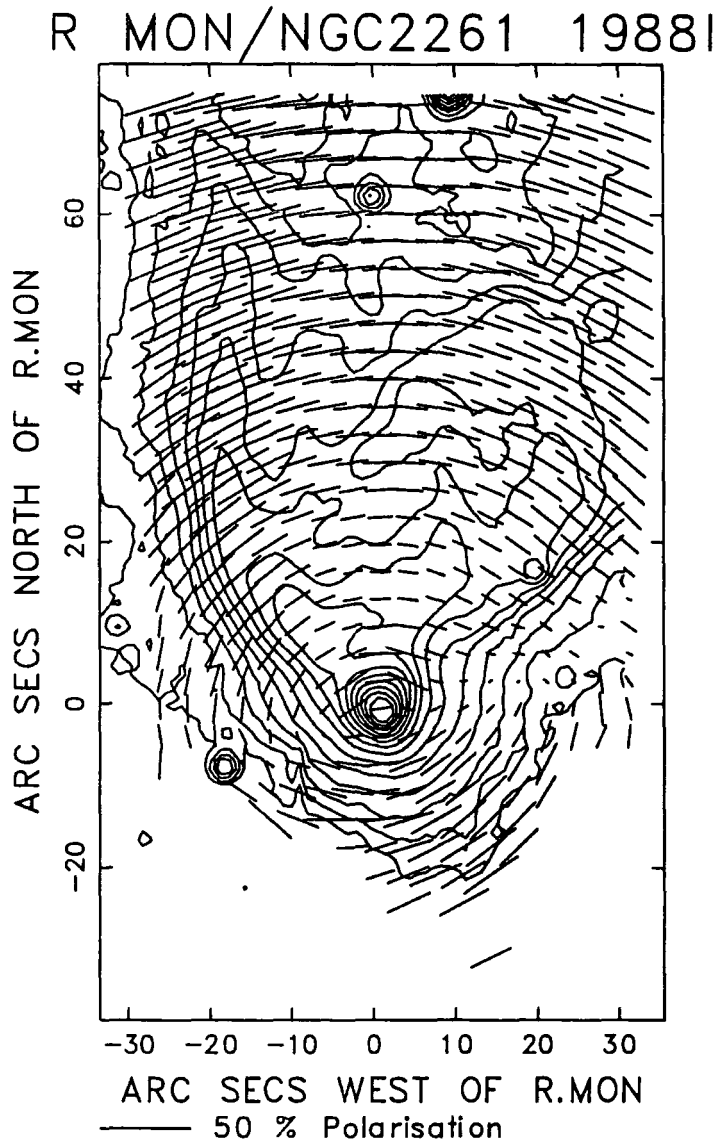


Figure 2.2: An intensity contour and polarization map of R Mon/NGC2261 from the 1988 I waveband dataset.

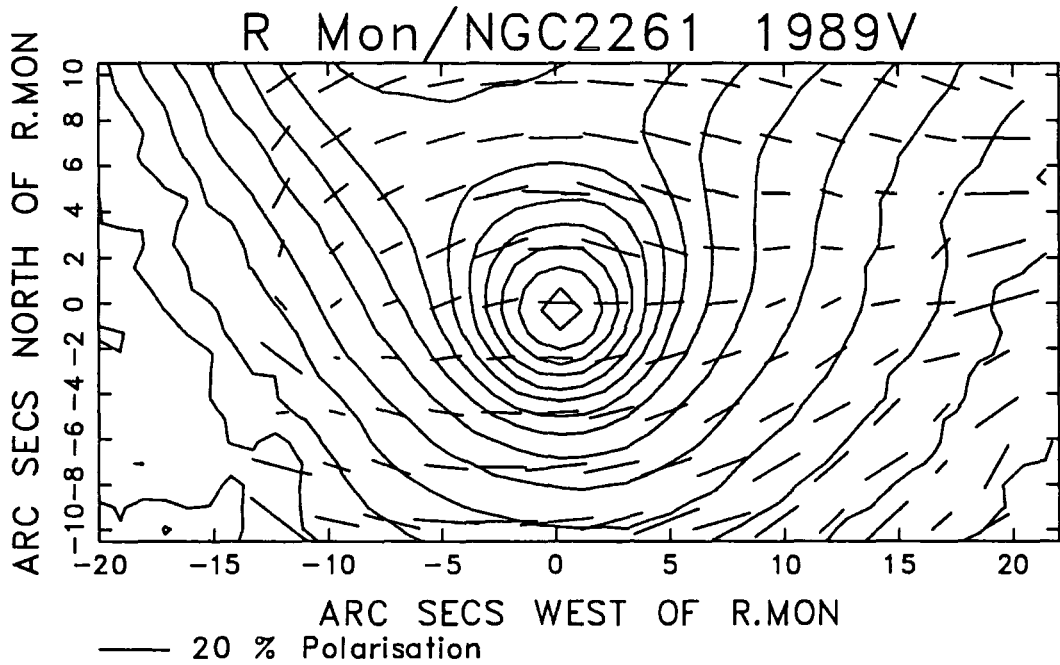


Figure 2.3: An intensity contour and polarization map of R Mon/NGC2261 from the 1989 V dataset. Note the null points in the polarization.

2.3.2 Synthesised Aperture Polarimetry

Polarization measurements were made upon all the datasets available to the author. A line of apertures of 3" diameter and separated by one pixel, (0.5"), was placed upon a north-south line running through the intensity maximum of R Mon, reaching 15" to the north, and the same distance south of R Mon. Figure 2.4 shows profiles of intensity and polarization along this line in the B, V, I and Z wavebands taken in 1989.

These profiles reveal a number of interesting phenomena: the polarization is found to increase to some maximum value at approximately 4-5" north of the R Mon intensity maximum, and the position of the minimum polarization is not coincident with the intensity maximum. These features will be discussed individually.

The Polarization of R Mon

The vast majority of the polarimetric measurements which have been made on R Mon itself, have been done with apertures of 10" or greater, as was illustrated in the work of Draper (1988), for example. Aspin, McLean and Coyne (1985) made measurements of the polarization of R Mon in wavelengths from B to R in apertures ranging in size from 5" to 30" in intervals of 5". Their conclusion was that regardless of the aperture size used, the resulting value of the polarization derived was "*essentially the same*"; "...aperture size is found to be unimportant in measurements" of the observed polarization, they say, and "*all the published values are representative of the true polarization at that epoch.*" Their results do however show a small change in the value of the polarizations measured as the aperture size changes, though it is difficult to draw a satisfactory conclusion from this since few errors have been quoted on their measurements.

Draper showed that as the aperture size upon R Mon is increased from a few arc-seconds upwards, there is a gradual increase in the polarization until the aperture is 10". At this point the polarization becomes generally more constant with increasing aperture size. The change in the polarization though is less than 1.5% in the

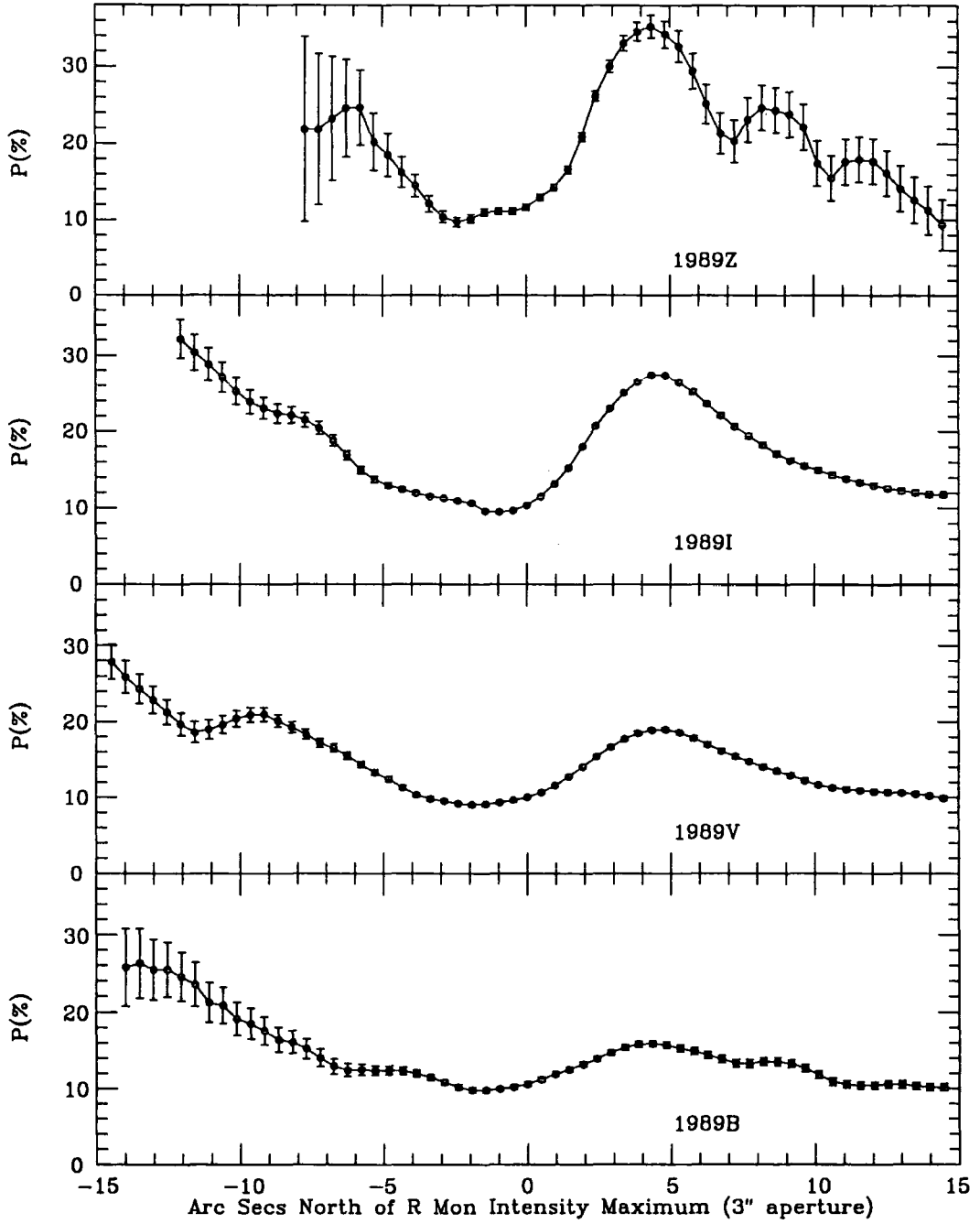


Figure 2.4: Polarization profile running north-south through R Mon. (Note: adjacent points do not represent independent polarization measurements due to smoothing effect of close aperture positions).

range of 3'' to 10'', and so Draper draws a similar conclusion to that of Aspin *et al.* (1985), that the polarization of R Mon is aperture independent. The waveband that Draper makes these measurements and conclusions upon is the V waveband, and the relevance of using this waveband for the measurements will become apparent later.

In an attempt to verify the conclusions drawn by Draper, and Aspin *et al.*, circular apertures of different sizes ranging from 3'' up to 20'' (where possible) were first placed upon the data taken in late January 1989, and later upon the 1990 datasets. If a plot is made of Polarization against aperture size in arcseconds for the 1989 V dataset, then we obtain a similar result to that obtained by Draper for data taken in the V waveband in 1986 (see figure 2.5).

We find that the polarization increases from some $10.0 \pm 0.2\%$ with a 3'' aperture up to some $11.3 \pm 0.2\%$ with a 10'' aperture, a change of only 1.3%. The polarization is roughly constant as we continue to increase the aperture size, as was concluded by the authors mentioned above. If, however, we now repeat the measurements at longer wavelengths, a different conclusion must be drawn.

Examining the 1989 I dataset (figure 2.5), we again see that the polarization increases with aperture size up to some point at which the polarization measured becomes more aperture independent. The difference now, however, is that the polarization changes from some $10.4 \pm 0.2\%$ with a 3'' aperture, up to $12.5 \pm 0.2\%$ with a 10'' aperture, a change of 2.1%. Analysis of the dependence upon aperture in the 1989 Z dataset (figure 2.5), reveals a change in polarization from $11.7 \pm 0.4\%$ with a 3'' aperture, up to $16.6 \pm 0.5\%$ with a 10'' aperture, a change now of as much as 5%. This reveals an important point. At shorter wavelengths, the size of the aperture used is not critical. The change in polarization is small, and Aspin *et al.* conclude that what change is occurring within their data is unimportant, (some 0.6% polarization change in the V waveband with increasing aperture size, with data taken in November 1983). However, as we move to longer wavelengths the aperture size is of critical importance, and the polarization changes by some 5% in the Z waveband

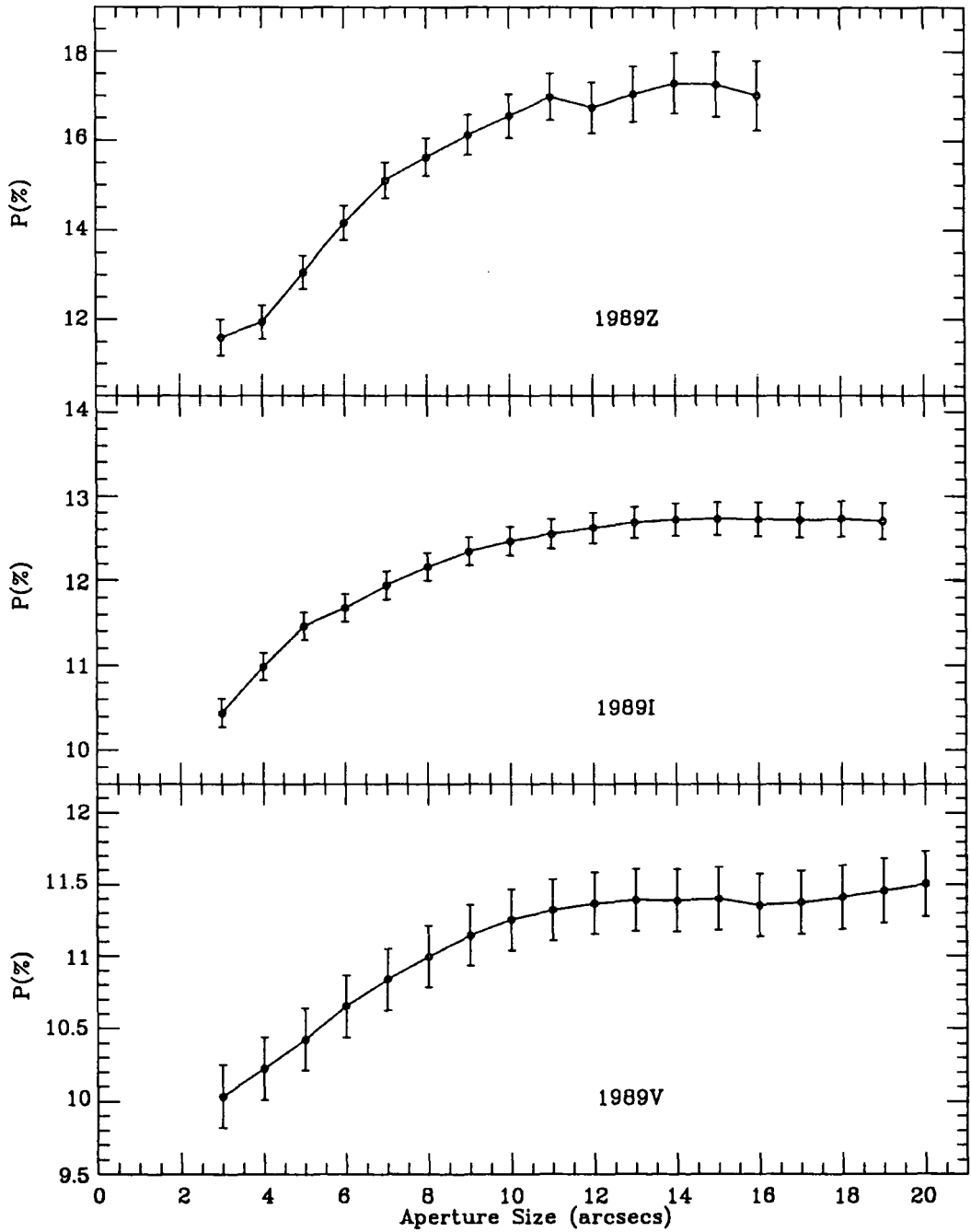


Figure 2.5: The variation of measured polarization for R Mon with aperture size. (Note the difference in scales on the polarization axis).

over the range 3" to 10" alone. If a very large aperture size is used on R Mon itself, then clearly a large part of the nebula will be included in the measurement, and since the nebula itself is highly polarized, spurious results will occur. This is a point that was discussed by Ward-Thompson (1984) when considering the variable star R Cr A and its surrounding nebula, when he showed that apertures of up to 47" had been used when attempting to measure the polarization of R Cr A itself by at least one author. Clearly, if an accurate measurement of the polarization of R Mon is to be made, then an aperture of this extreme size must not be used.

As has been illustrated above, there is a more significant change in the polarization of R Mon with aperture size than had previously been concluded by other authors. This is shown by analysing data from a broader spread of wavelengths than was done, or was available to the authors above. It is no longer valid to assume that it is safe to use a 10" aperture in measurements on R Mon, unless the reason for doing so is to compare the results obtained with those presented by others using that size of aperture. If we are to look at the polarization of R Mon itself, then a small aperture must be used. The results illustrated here show that results with, say, a 5" aperture, cannot be compared with those from a 15" aperture, especially at longer wavelengths. The truth must therefore also be apparent that in all the many works published on NGC2261 over the past 80 years, the polarization of R Mon has rarely been accurately measured because the aperture size used has always been too large.

Another question must also be asked: why does the aperture size used in measurements become more critical at longer wavelengths? The change in the aperture dependence is an interesting effect, and was therefore investigated to find its cause.

Polarization measurements were made upon R Mon with a 3" circular aperture, and are summarised in table 2.1. The results obtained using a 10" aperture are to be found in table 2.2. The resulting measurements using the 3" sized aperture seem to show a basically constant or slow increase in the value of the polarization with wavelength (see figure 2.6). The B waveband has a measured polarization of

$10.6 \pm 0.3\%$ which rises to only $11.7 \pm 0.4\%$ in the Z. (The 1990 datasets concur, with an increase in polarization from B to I of only 0.6%, from $10.0 \pm 0.3\%$ to $10.6 \pm 0.3\%$). In other words, the polarization of R Mon itself is effectively uniform across the full wavelength range, and the polarization is wavelength independent. The mean polarization for the 1989 datasets from B to Z is 10.7%, with a standard error on this mean of 0.4%. (For the 1990 datasets, the mean polarization of R Mon is 10.2% with a standard error of 0.2%).

If $10''$ apertures are placed upon the data, centred at the intensity maximum, then a larger change in the polarization of R Mon results than that seen using a $3''$ aperture. Figure 2.6 shows the difference in the measured polarization of R Mon when using both $3''$ and $10''$ apertures.

For the 1989 datasets, the polarization increases from $10.5 \pm 0.3\%$ in B, up to $16.6 \pm 0.5\%$ in Z, using a $10''$ aperture. (For the 1990 datasets, the polarization changes from $10.9 \pm 0.3\%$ in B to $13.5 \pm 0.2\%$ in I, using a $10''$ aperture). The greatest deviation between the polarizations measured with a $3''$ and a $10''$ aperture is found at the longer wavelengths, as is clearly demonstrated in figure 2.6.

H α Measurements of R Mon

R Mon was found to have a polarization of $10.3 \pm 0.3\%$ at $88.5 \pm 0.7^\circ$ in H α (with a $3''$ aperture), from the data obtained in 1990. This compares with the values obtained by Garrison and Anderson (1978) for example, who measured polarizations of $13.1 \pm 0.6\%$ at a position angle of $106 \pm 1^\circ$, though it is not known what aperture size this authors used for their measurements. The data obtained in the continuum and the H α initially presented the author with the ability to check to see if the H α was depolarized with respect to the continuum as suggested by Aspin *et al.* (1985). However, analysis of the data revealed that the continuum dataset had a small focus error. It was therefore decided that it was inadvisable to compare the continuum with the H α polarization for measurements made with a $3''$ aperture. Measurements were therefore made on the H α and the continuum data using apertures of $10''$,

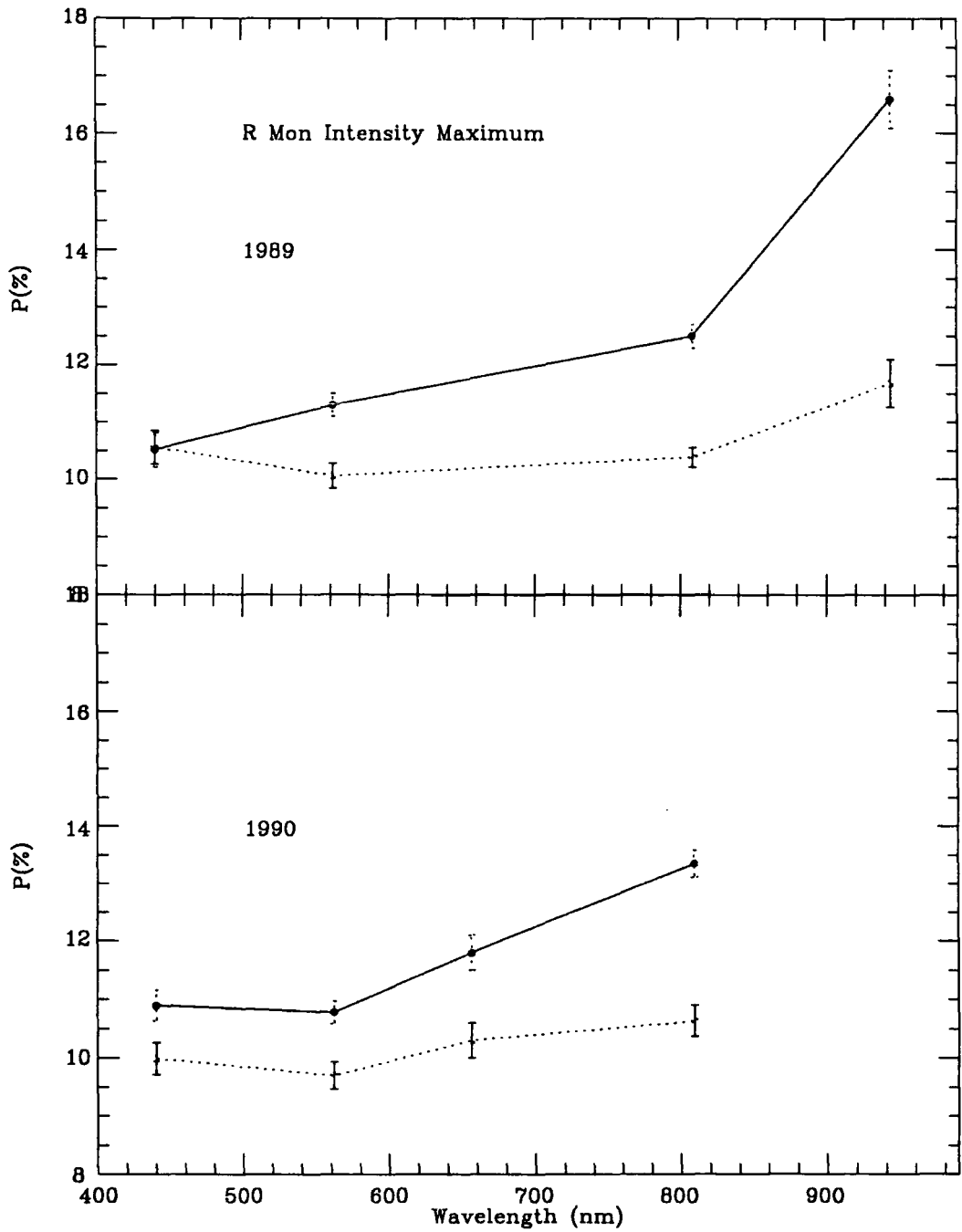


Figure 2.6: The polarization at R Mon using a 3'' aperture (dotted line) and a 10'' aperture (black circles) for the 1989 & 1990 datasets.

R Mon Intensity Maximum 3" aperture					
Observing Run	Waveband	P(%)	δP (%)	θ ($^{\circ}$)	$\delta\theta$ ($^{\circ}$)
3rd January 1979	V	9.4	0.4	76.0	1.2
5th January 1979	R	10.6	0.4	63.9	1.1
January 1981	V	16.6	0.4	98.7	0.7
18th February 1985	I	9.7	0.2	114.9	0.7
13th December 1985	I	8.7	0.2	111.6	0.7
16th December 1985	R	9.9	0.2	96.9	0.5
14th December 1985	Z	14.3	0.3	103.7	0.5
5th January 1986	V	9.2	0.2	89.7	0.6
12th March 1986	I	14.1	0.3	107.4	0.5
17th March 1988	I	11.6	0.3	93.7	0.6
29th January 1989	B	10.6	0.3	88.4	0.8
28/29th January 1989	V	10.0	0.2	89.1	0.6
27/28th January 1989	I	10.4	0.2	87.6	0.5
29th January 1989	Z	11.7	0.4	79.5	1.0
25th February 1990	B	10.0	0.3	93.0	0.8
25th February 1990	V	9.7	0.2	97.4	0.7
23rd February 1990	H α	10.3	0.3	88.5	0.8
27th February 1990	I	10.6	0.3	105.7	0.7
19th January 1991	V	12.4	0.3	80.6	0.6

Table 2.1: Aperture polarimetry with apertures centroided at the R Mon intensity maximum, and using a simulated 3" circular aperture.

R Mon Intensity Maximum 10" aperture					
Observing Run	Waveband	P(%)	δP (%)	θ ($^{\circ}$)	$\delta\theta$ ($^{\circ}$)
January 1979	V	13.4	0.5	72.0	1.5
January 1979	R	14.9	0.5	67.0	1.5
January 1981	V	15.7	0.5	93.0	1.1
February 1985	I	10.6	0.3	109.6	1.0
December 1985	I	11.6	0.3	104.5	1.0
December 1985	R	10.6	0.3	96.5	1.0
December 1985	Z	12.4	0.4	106.5	1.5
January 1986	V	10.5	0.3	94.0	1.5
March 1986	I	12.7	0.3	105.7	1.0
March 1988	I	13.1	0.3	96.5	0.6
January 1989	B	10.5	0.3	90.6	0.8
January 1989	V	11.3	0.2	93.1	0.5
January 1989	I	12.5	0.2	92.0	0.4
January 1989	Z	16.6	0.5	92.8	0.8
January 1990	B	10.9	0.3	91.0	0.7
January 1990	V	12.3	0.3	94.0	0.6
January 1990	H α	11.8	0.3	93.9	0.7
January 1990	I	13.5	0.2	99.3	0.5
January 1991	V	12.3	0.3	82.8	0.6

Table 2.2: Aperture polarimetry with 10" circular apertures centroided on the R Mon intensity maximum.

which are much larger than the size of the out-of-focus image. This allowed a ready comparison with the measurements of Draper (1988) for example, who also used a 10'' aperture. The $H\alpha$ was found to have a polarization of $11.8 \pm 0.3\%$ at a position angle of $93.9 \pm 0.7^\circ$, whilst the continuum was found to have a polarization of $11.9 \pm 0.3\%$ at a position angle of $92.5 \pm 0.7^\circ$ (with a 10'' aperture). It is clear then that the measured polarizations in the continuum and the $H\alpha$ are essentially the same within errors. These results will be discussed later in section 2.4.1.

The Polarization Knot

If a greyscale intensity image is generated from polarization calculations, see figure 2.7, then it is apparent that there is a region of high polarization to the north of the R Mon intensity maximum. (In figure 2.7 white represents high polarization regions and black low polarization). Figure 2.7 was taken from polarization measurements made in the 1988 I waveband dataset.

This highly polarized region coincides with the polarization peak evident in figure 2.4 and hereafter it will be termed the polarization knot. The knot covers an area of $\sim 5\text{--}10''$ by $5''$.

Polarization measurements were made of the polarization knot, using an aperture of $3''$. This was chosen as a good size, since a vastly larger sized aperture would include polarization effects from both R Mon and the nebula of NGC2261. A smaller aperture could also be possibly more prone to being affected by the seeing at the time of the observations. These measurements are summarised in table 2.3.

The polarization of the knot was found to be greatly wavelength dependent as is clearly illustrated in figure 2.8, rising very rapidly from $15.9 \pm 0.4\%$ in the B from the 1989 observations, up to over 35% in the Z waveband; ($35.3 \pm 1.5\%$).

The results are confirmed in the 1990 observations, as the polarization increases from $16.2 \pm 0.3\%$ in B up to almost 26% in the I waveband, ($25.9 \pm 0.2\%$ measured). Minchin *et al.* (1991) have also shown that the level of polarization found at the knot is in excess of 50% in the infrared.



Figure 2.7: A greyscale polarization image (I waveband in March 1988). Note the highly polarized region (white) north of R Mon (cross).

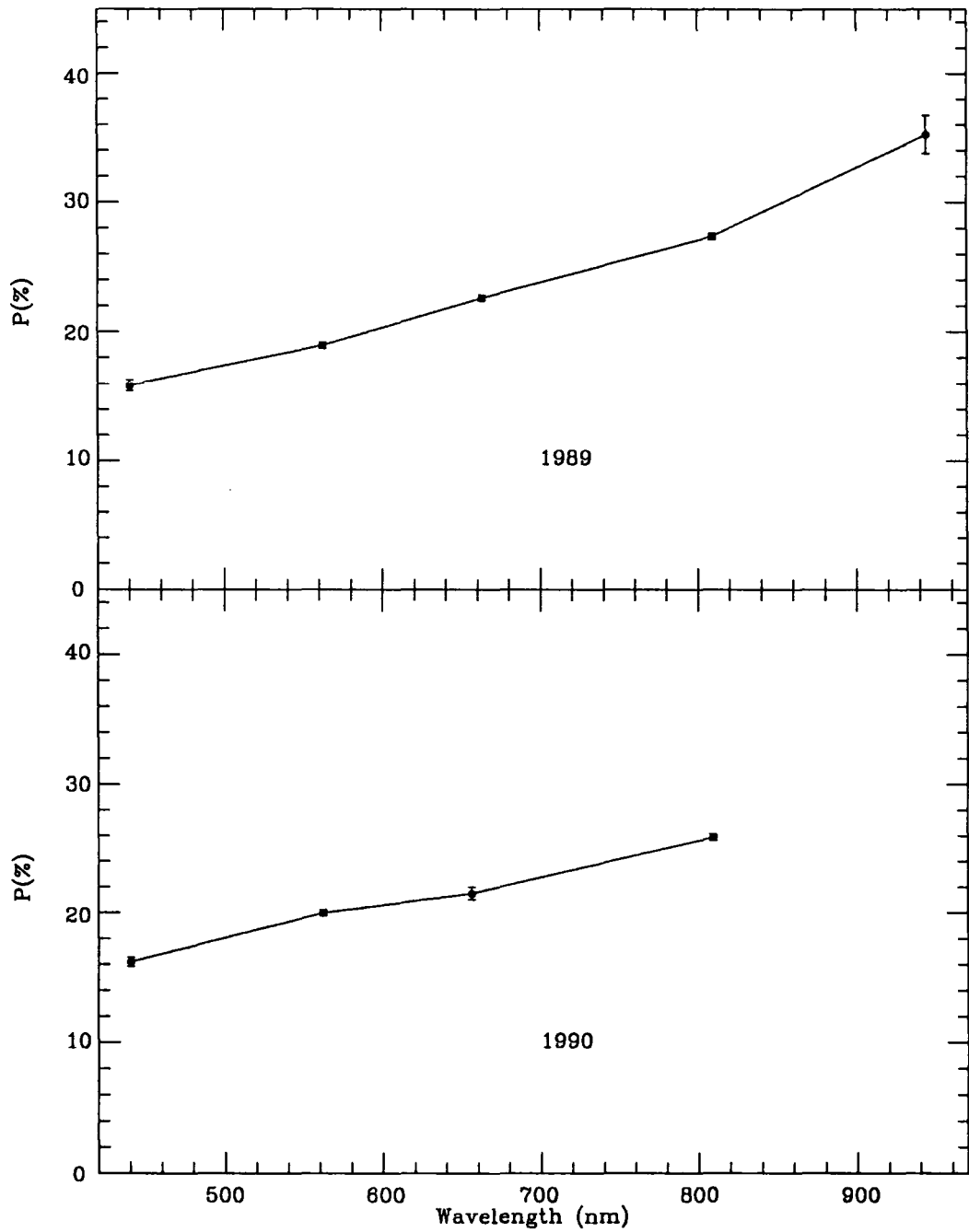


Figure 2.8: The variation of polarization with wavelength for the polarization knot, from measurements using a 3'' aperture on the 1989 and 1990 datasets.

R Mon Polarization Knot 3" aperture					
Observing Run	Waveband	P(%)	$\delta P(\%)$	$\theta(^{\circ})$	$\delta\theta(^{\circ})$
January 1979	V	22.3	0.6	75.1	0.8
January 1979	R	24.2	0.7	75.7	0.8
January 1981	V	25.8	0.6	90.8	0.7
February 1985	I	14.8	0.3	96.4	0.7
December 1985	I	20.7	0.4	93.8	0.5
December 1985	R	18.8	0.2	89.6	0.3
December 1985	Z	23.1	0.8	92.0	1.0
January 1986	V	17.8	0.2	84.5	0.3
March 1986	I	19.2	0.3	91.8	0.5
March 1988	I	29.8	0.2	89.9	0.2
January 1989	B	15.9	0.4	88.6	0.7
January 1989	V	18.9	0.3	89.4	0.4
January 1989	R	22.6	0.2	87.5	0.3
January 1989	I	27.4	0.2	86.9	0.2
January 1989	Z	35.3	1.5	88.4	1.2
February 1990	B	16.2	0.3	89.4	0.6
February 1990	V	20.0	0.2	89.9	0.3
February 1990	H α	21.5	0.5	95.0	0.6
February 1990	I	25.9	0.2	91.3	0.3
January 1991	V	21.2	0.4	85.6	0.4

Table 2.3: Aperture polarimetry measurements at the polarization knot, using a simulated 3" circular aperture.

Measurements made determining the position angle at the knot show that the position angle is constant and wavelength independent for both the 1989 and the 1990 datasets, (see figure 2.9). At shorter wavelengths the measured angles from the two observing runs are very similar, $88.6 \pm 0.7^{\circ}$ for B in 1989 and $89.4 \pm 0.6^{\circ}$ for B from the 1990 run. Within errors therefore, these values are the same. In the I waveband, the values found are $86.9 \pm 0.2^{\circ}$ for 1989 and $91.3 \pm 0.3^{\circ}$ for 1990. The mean value of the position angle for the 1989 datasets was found to be 88.2° , with a standard error on the mean of 0.4° . The mean position angle for the 1990 datasets was found to be 91.4° , with a standard error on the mean of 1.3° .

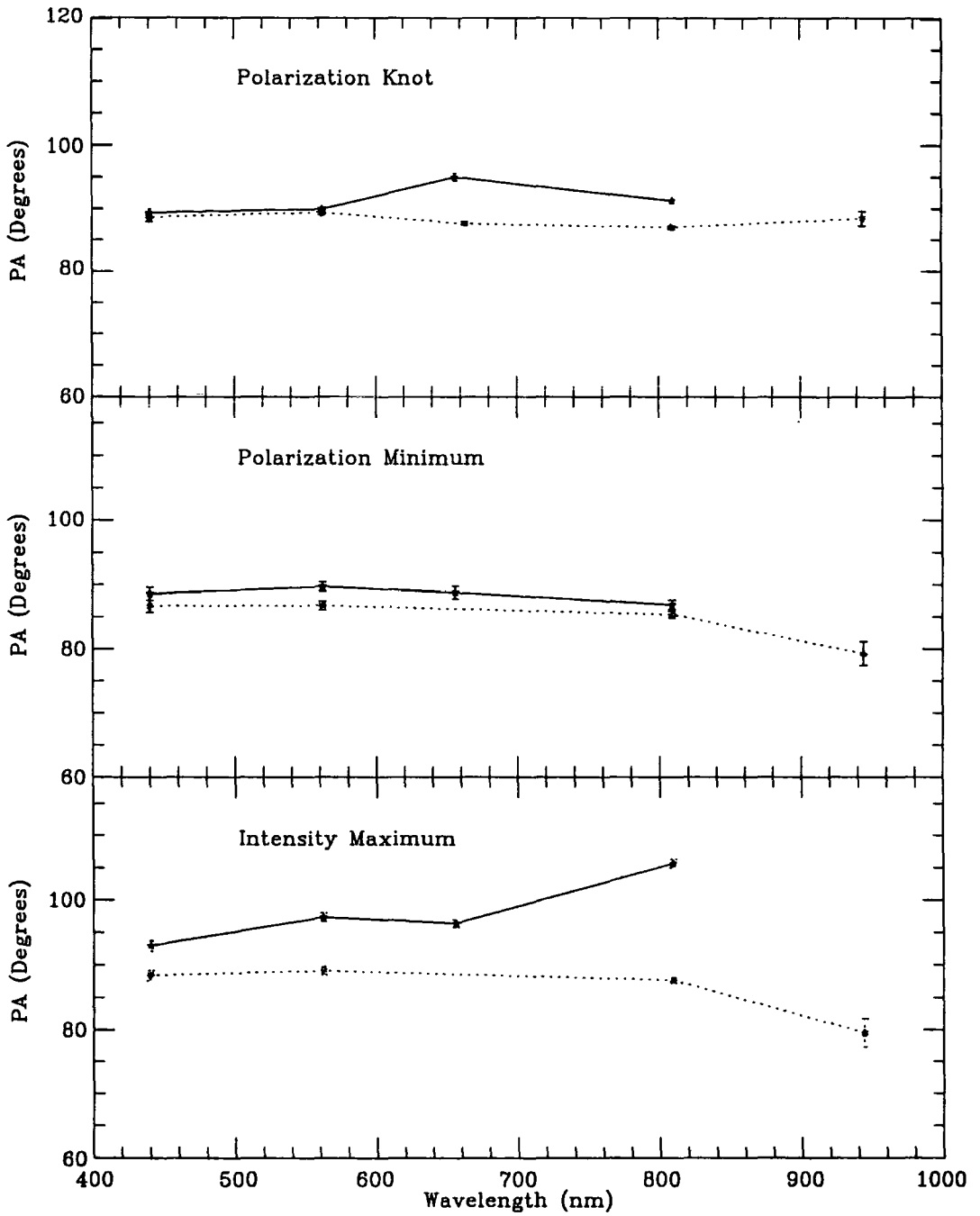


Figure 2.9: The variation of polarization position angle with wavelength using a 3" aperture at different points for the 1989 (dotted-line) & 1990 data.

The location of the polarization knot is at such a distance away from the intensity maximum that measurements made with the 3" aperture should be unaffected by the polarization of R Mon with respect to the seeing, and vice-versa for the 1989 and 1990 observations. The mean position for the polarization knot in the 1989 and 1990 datasets was found to be $\sim 4.8 \pm 1.0''$, and $\sim 4.7 \pm 1.0''$ north of the R Mon intensity maximum respectively. The location of this polarization knot was found to be constantly at the same position, within errors, in all the data looked at.

2.3.3 The Polarization Minimum

The plots of polarization against distance from the intensity maximum of R Mon shown for the 1989 datasets in figure 2.4 reveal two things. Firstly the polarization peaks some 5" or so north of R Mon, and this has been discussed earlier in this chapter. Secondly, the polarization does not drop to a minimum at the intensity maximum as expected. Instead the minimum is reached at some point, usually between 1" and 3" south of the intensity maximum of R Mon, in all the datasets that have been available to the author. It is also found that the position of this polarization minimum is not so clearly defined in the all datasets available, as is the position of the polarization knot.

Using data from the 1989 and 1990 datasets at the point of minimum polarization the angular dependence is pretty flat, changing, for example, from $88.6 \pm 1.0\%$ in B to $86.4 \pm 0.7\%$ in I in the 1990 datasets (see figure 2.9). (Like the measurements at the R Mon intensity maximum, the polarization measurements at the polarization minimum are generally wavelength independent. The polarization changes from $8.7 \pm 0.3\%$ in B in 1990, up to $9.7 \pm 0.2\%$ in I. In 1989 the values are also fairly constant, with a value in the B of $9.8 \pm 0.3\%$ changing to only $9.7 \pm 0.6\%$ in the Z waveband (See table 2.4)).

The mean location of the polarization minimum in the 1989 and 1990 datasets was found to be $\sim 1.4 \pm 1.9''$ and $\sim 2.8 \pm 1.9''$ south of the R Mon intensity maximum, respectively.

R Mon Polarization Minimum 3" aperture					
Observing Run	Waveband	P(%)	δP (%)	θ ($^{\circ}$)	$\delta\theta$ ($^{\circ}$)
January 1989	B	9.8	0.3	86.7	0.9
January 1989	V	9.0	0.2	86.8	0.7
January 1989	I	9.5	0.2	85.4	0.5
January 1989	Z	9.7	0.6	86.3	1.9
February 1990	B	8.7	0.3	88.6	1.0
February 1990	V	7.9	0.2	89.7	0.7
February 1990	H α	9.0	0.4	91.1	1.1
February 1990	I	9.7	0.2	86.4	0.7

Table 2.4: Aperture polarimetry measurements at the “polarization Minimum” using a simulated 3" circular aperture on the 1989 & 1990 datasets.

2.3.4 Polarization Measurements in NGC2261

Polarization measurements were made at a number of places, chosen fairly randomly, within the nebula NGC2261. Apertures of 10" in size were placed at positions 37" north, 50" north, and 50" north & 12" east of the intensity maximum of R Mon. These will be referred to hereafter, as position 1, position 2 and position 3. The reason for making measurements at more than one position in the nebula, was to be sure that any pattern or relationship that resulted from the measurements, occurred everywhere within the nebula. If it was found that different results were obtained at each point, then further investigations in order to explain these phenomena would need to be carried out. Measurements were also made using a 3" aperture at these three positions, and no significant difference was found between the measurements made with the 10" aperture, as might, perhaps be expected, since in the nebula we are dealing with large scale structure, which does not change drastically as the aperture size is changed. In some ways, a 10" aperture is a distinct advantage. With a smaller aperture size, if a bad pixel or a cosmic ray were to fall within the aperture, a more erroneous measurement could be made than a measurement where a larger aperture size, which has the effect of smoothing the data somewhat.

Naturally, in those measurements made upon the small scale microstructure around R Mon, any irregularities which resulted in these measurements were thoroughly investigated, and no bad pixels or cosmic rays are involved in any of the polarization measurements made upon R Mon and the polarization knot.

In figure 2.10 it can be seen that the polarization measurements made in the nebula all show some wavelength dependence.

The polarization increases with increasing wavelength, and the rise in polarization with wavelength is greatest at the furthest position from the intensity maximum of R Mon, where the polarization is most strongly wavelength dependent. At this position, (position 3, 50'' north & 12'' east), the polarization rises from $20.3 \pm 0.8\%$ in B, for the 1989 dataset to $33.6 \pm 1.5\%$ in I: a change in the polarization of over 13%. Measurements were not made upon the Z dataset from this observing run, due to the poor amount of signal in the nebula at this distance from R Mon. (For the 1990 datasets (not illustrated), the polarization rises from $20.1 \pm 0.7\%$ in B, to $32.2 \pm 0.9\%$ in I. These values almost exactly match the values calculated for the 1989 datasets). For an aperture placed only 37'' from the intensity maximum of R Mon (position 1), the polarization rises from $15.5 \pm 0.3\%$ in B, to $21.6 \pm 0.5\%$ in I for the 1989 datasets. The rise is therefore now only some 6%. (This situation is echoed in the 1990 datasets, with a rise in the polarization from $14.6 \pm 0.4\%$ in B, to $21.0 \pm 0.4\%$ in I).

The position angle, when measured at these 3 positions within the nebula (figure 2.10), remains generally constant and wavelength independent. There is again little difference in using a 3'' aperture in preference to a 10'' aperture, and the measurements quoted here were made using the latter aperture size. For the 1989 datasets, the mean position angle is 104.3° , with a standard error on the mean of 0.4° at position 3. (For the 1990 datasets (not shown), the mean position angle is $105.8 \pm 1.3^\circ$). At position 1, the mean values of the position angles are $89.4 \pm 0.8^\circ$ for 1989 (and $87.5 \pm 0.3^\circ$ for the 1990 datasets).

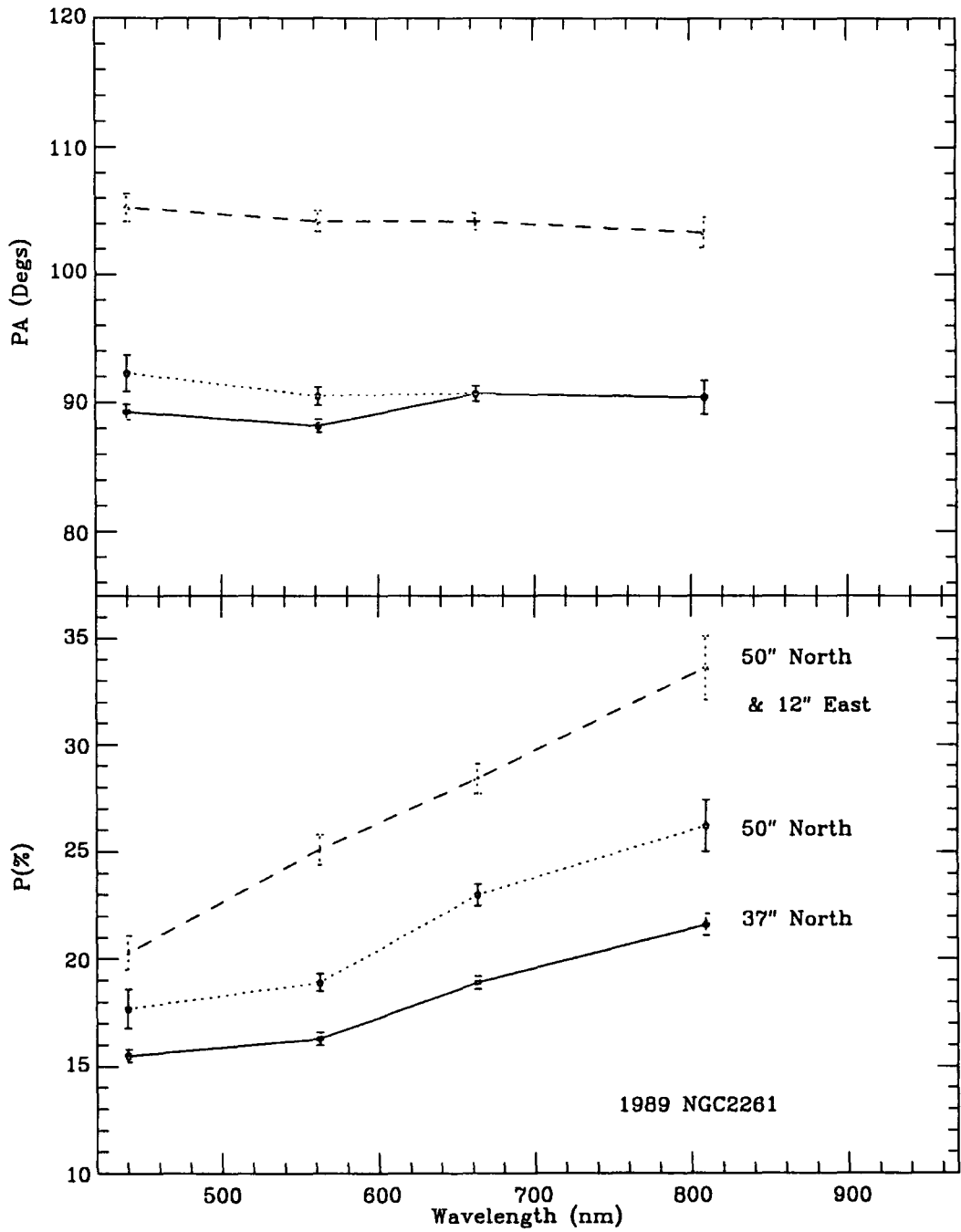


Figure 2.10: Variation of polarization with wavelength at three arbitrary points in NGC2261; measurements were made with a 10" aperture.

2.3.5 Time Variation of Polarization in NGC2261/R Mon

Draper (1988) presented an analysis of how the polarization and position angle of R Mon changed with time, using his own data and data gleaned from the many scientific papers that have been published on the polarization of R Mon. This work has been extended, using an aperture size of $10''$ as was used by those authors quoted by Draper, to include the 1989 and 1990 datasets reduced by the author. Data included here includes the work of Hall (1965); Zellner (1970); Vrba *et al.* (1979); Garrison and Anderson (1978); Jones and Dyck (1978); Aspin *et al.* (1985) and Draper (1988), and is presented in figure 2.11.

Far more interesting, however, is the opportunity to reanalyse all the polarization data collected by the Durham Polarimetry Group, in the light of the revelations concerning the aperture dependence of polarization of R Mon and the effect of the polarization knot, using a small aperture. How the degree of polarization and the position angle of the knot change with time will be eagerly studied.

Polarization measurements made upon all the data collated by the Durham Polarimetry Group in the V-waveband with a $3''$ circular aperture are presented in figure 2.12.

This illustrates that the polarization of R Mon rises from $9.4 \pm 0.4\%$ in January 1979, up to a maximum value of $16.6 \pm 0.4\%$ in January 1981. Measurements taken on data from January 1986 until February 1990 show a more uniform level in the polarization, with a mean value of $9.6 \pm 0.2\%$, before an increase to $12.4 \pm 0.3\%$ in January 1991. This seems to imply that the value in 1979 was the more normal value for the polarization at R Mon, and that something interesting happened around 1981. Measurements by Draper show a similar value for the polarization at this time, and a measurement by Aspin *et al.* (1985), also show that in November 1983 the polarization was at some higher value than the average calculated by the author for the years excluding 1981; (14.5% with a $10''$ aperture, and 13.9% with a $5''$ aperture). This would seem to confirm, that from data provided by a totally independent source, the polarization of R Mon peaked at the value quoted above somewhere

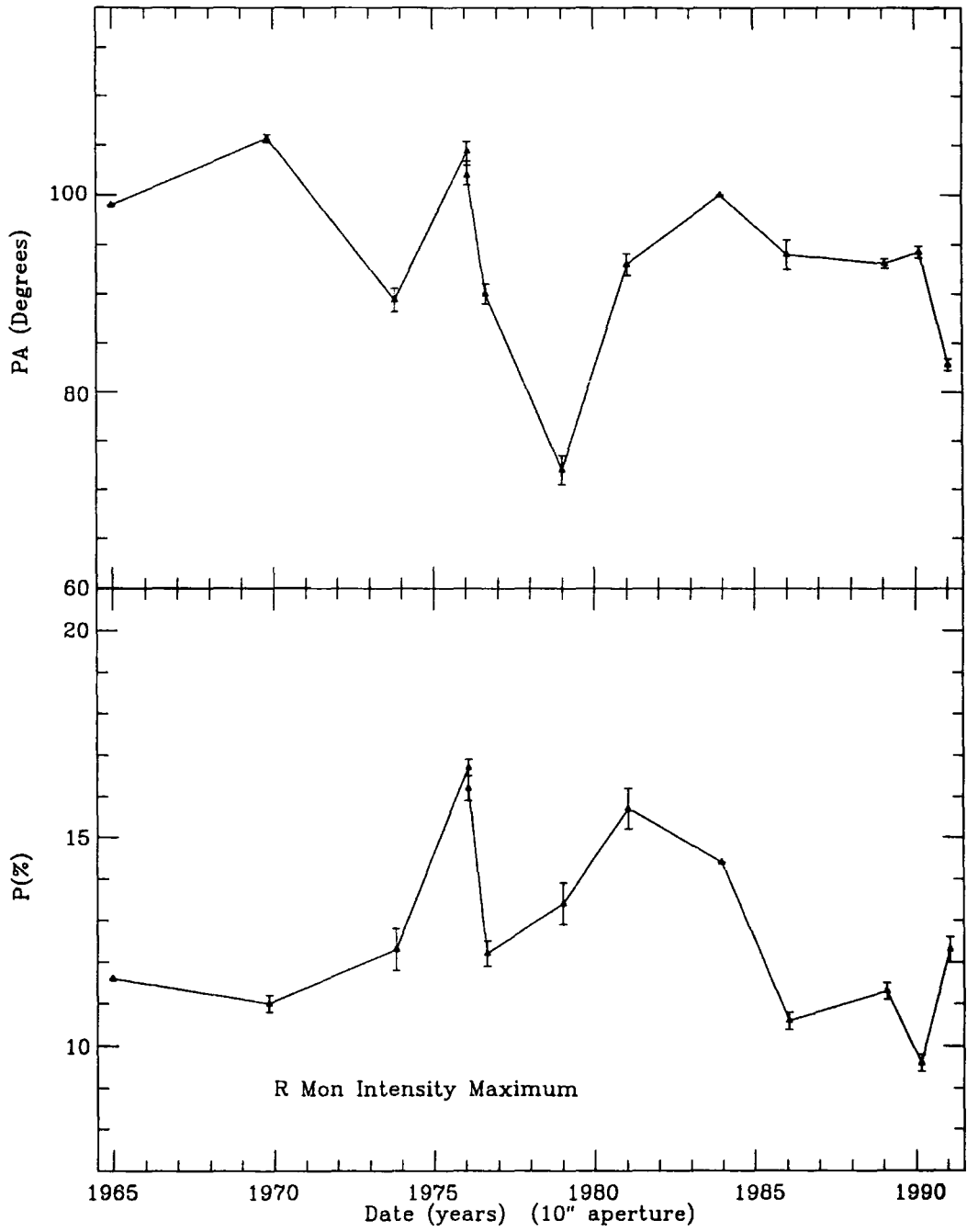


Figure 2.11: The variation in the measured polarization and position angle at R Mon with time using a 10'' aperture; data from various sources (see text).

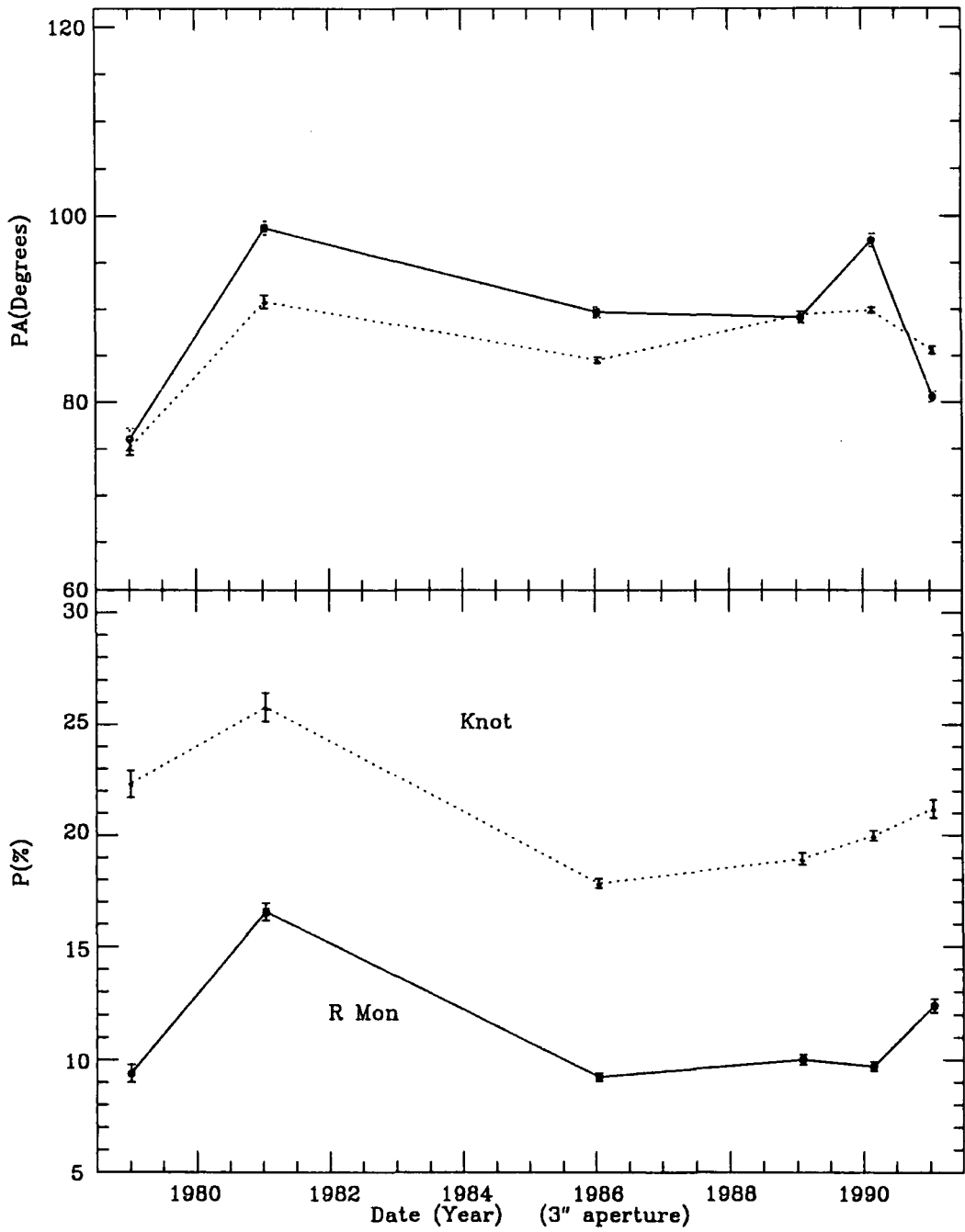


Figure 2.12: The variation of measured polarization and position angle with time at R Mon and the polarization knot in the V waveband.

between 1979 and 1986, for the Durham data.

If we now look at the value of the polarization found at the polarization knot in the V-waveband (see figure 2.12), we see a remarkably similar pattern to that obtained at the intensity maximum of R Mon. The polarization rises from $22.3 \pm 0.6\%$ in 1979, to a maximum value of $25.8 \pm 0.6\%$ in 1981. By 1986 the value has dropped down to $17.8 \pm 0.2\%$, and the value remains at an average polarization of $18.9 \pm 0.6\%$. The relationship between the two plots of polarization over this time period is striking. There is a very similar shape to the pattern of the change in the position angle with time at the knot and at R Mon. A maximum value for the position angle, is found again for 1981 at both positions, measuring $90.8 \pm 0.7^\circ$ at the knot, and $98.7 \pm 0.7^\circ$ at R Mon.

Figure 2.12 seems to suggest that there is a correlation between the polarization measured at R Mon and at the polarization knot. Further polarization measurements were made in steps of $5''$, along a line from the R Mon intensity maximum out to a position $\sim 50''$ north of R Mon, in an attempt to see if this correlation between the polarization at R Mon and the polarization in NGC2261 was maintained. The variation of polarization with time at each of these positions is illustrated in figures 2.13 and 2.14, whilst the variation in the measured polarization position angle is represented in figures 2.15 and 2.16; the results obtained from these diagrams are discussed in the next section.

2.4 Discussion and Interpretation

2.4.1 R Mon and The Polarization Knot

It has been shown how the knot is highly polarized, especially so at the longer wavelengths (see figure 2.8). It should also be clear that when a $10''$ or larger aperture is used in an attempt to measure the polarization of R Mon, the polarization knot is being included within the aperture, and the knot is contributing to the measured result. The measured polarization of R Mon becomes more inaccurate as longer

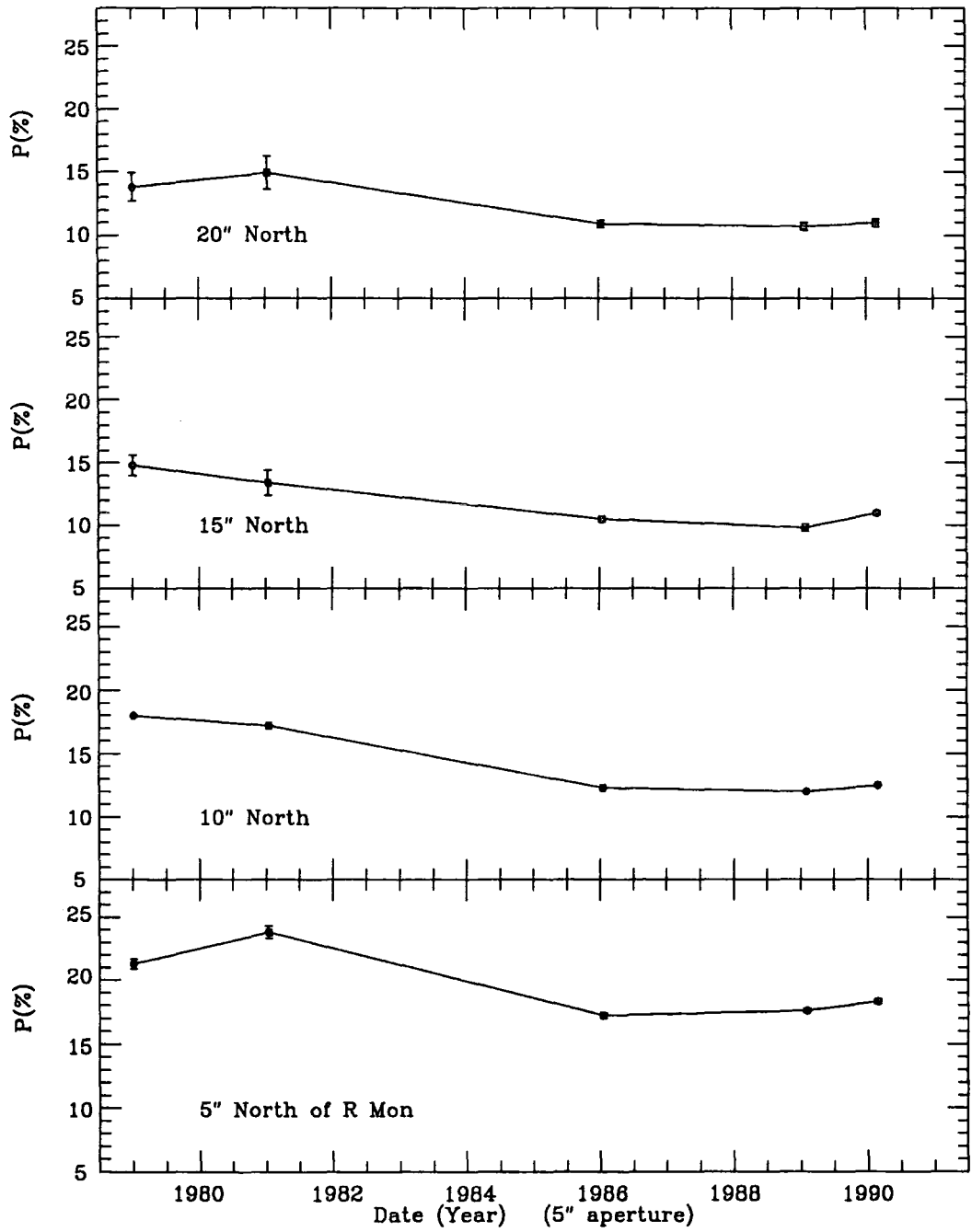


Figure 2.13: The change in polarization with time at a distance of 5–20" North of the R Mon intensity maximum.

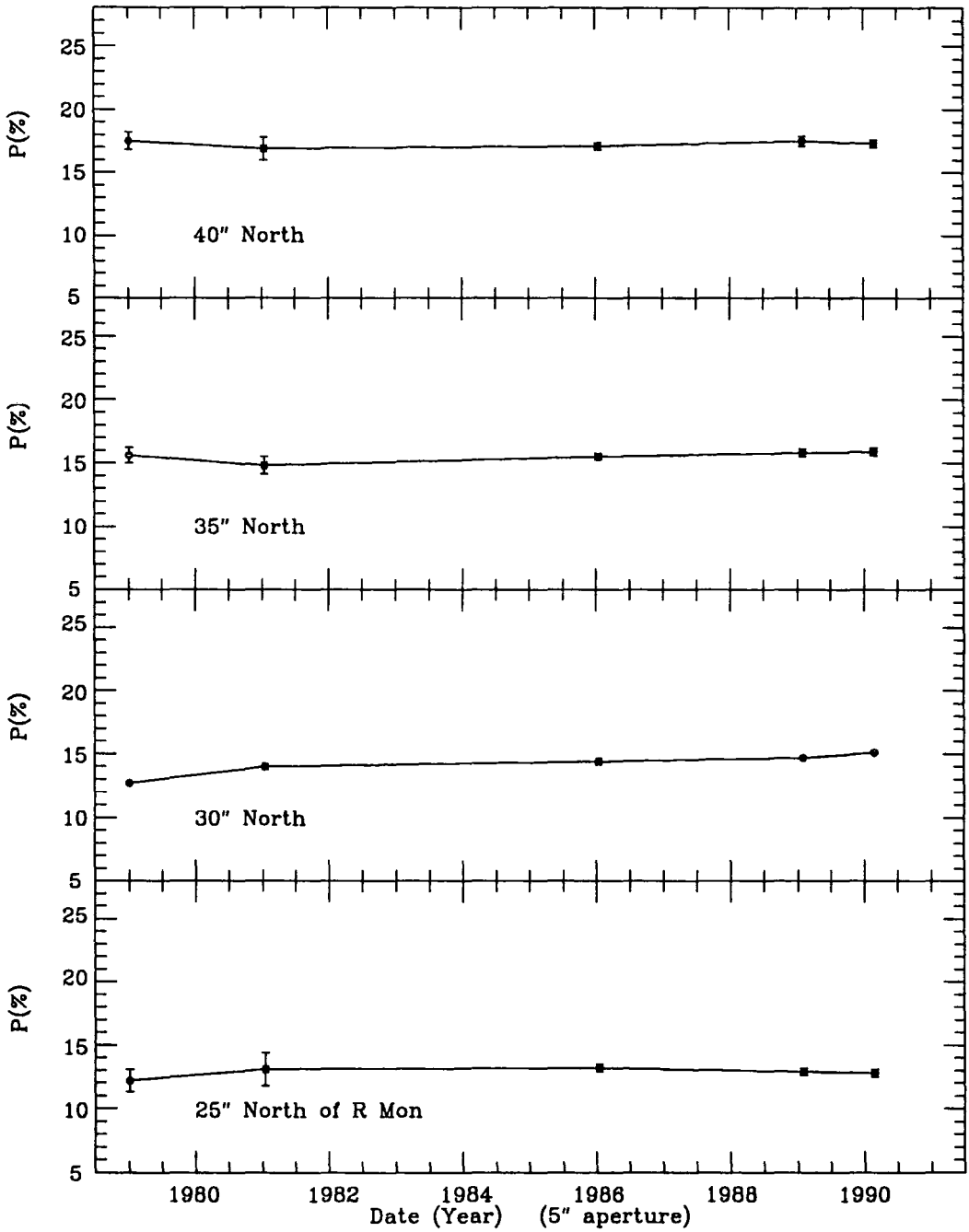


Figure 2.14: The change in polarization with time at a distance of 25–40" North of the R Mon intensity maximum.

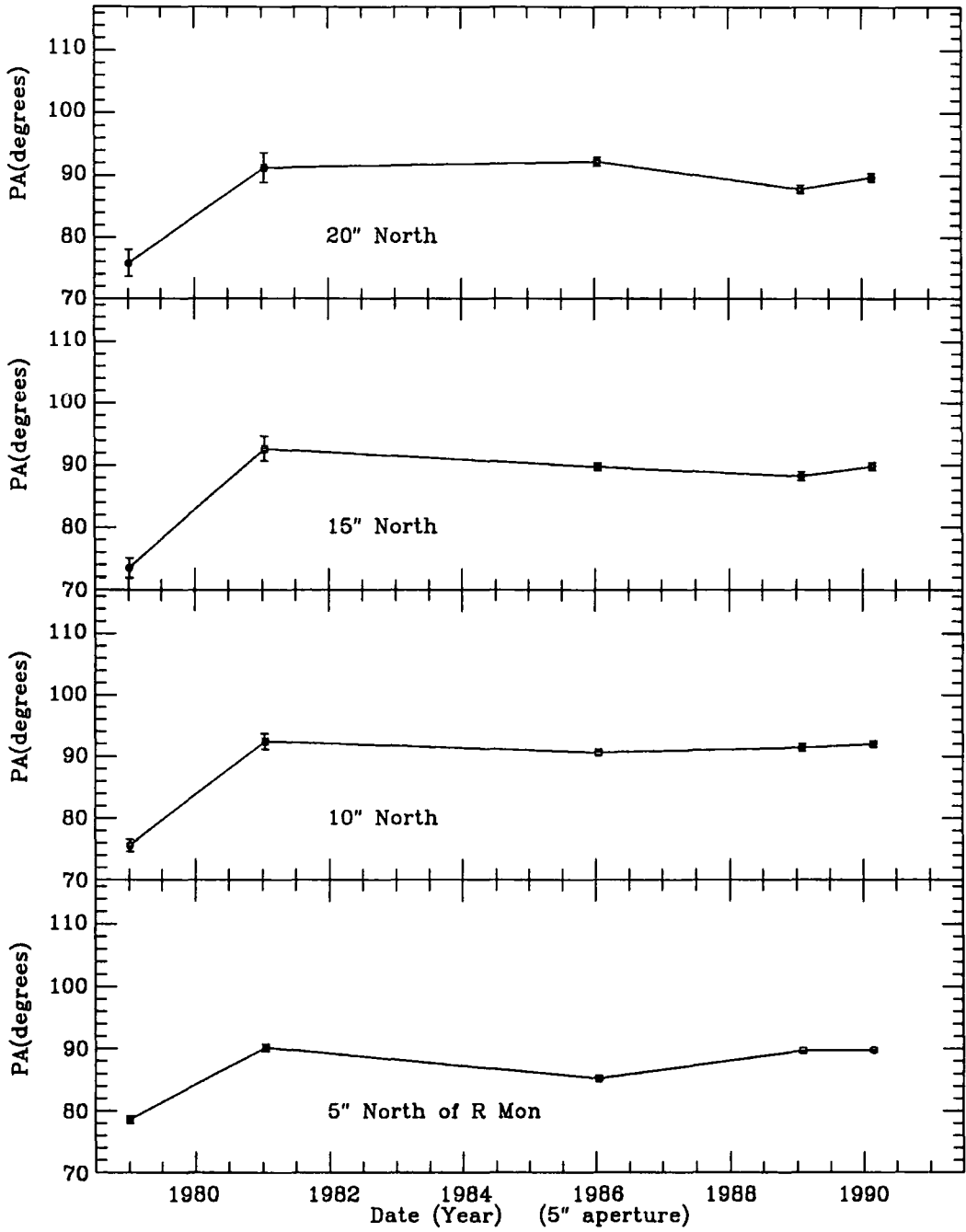


Figure 2.15: The change in position angle with time at a distance of 5–20" North of the R Mon intensity maximum.

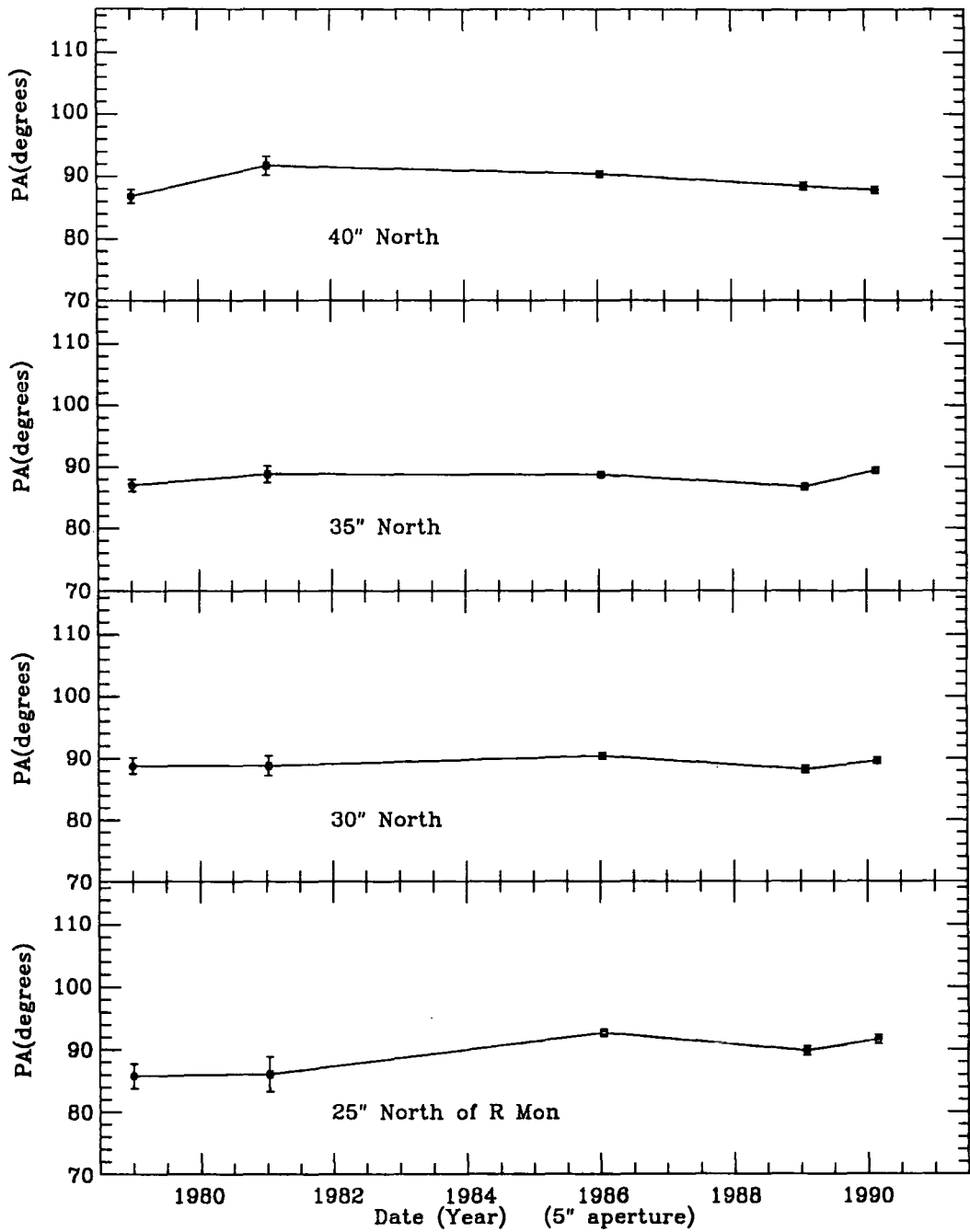


Figure 2.16: The change in position angle with time at a distance of 25–40" North of the R Mon intensity maximum.

wavelengths are reached. Thus, the only way to accurately measure the polarization of R Mon is to use an aperture size which is small enough to exclude the effects of the polarization knot. Recently, Minchin *et al.* (1991) have measured the polarization at the knot in J, H and K, and reveal that the measured polarization rises up to a value in excess of 50%, confirming results obtained by the author on the wavelength dependence of the knot. Minchin *et al.* put the position of the peak polarization at about 3" north of the R Mon in J and H, and some 5" north in K. The other important thing to be remarked upon, is that these authors then make measurements of the polarization of R Mon using an 8" aperture. The result of this, is that they again include polarization effects from the knot which is very highly polarized at these wavelengths. Thus, their assumption that the measured polarization reflects the true polarization due to R Mon is incorrect.

The Polarization of R Mon

Discs around such stars as R Mon are accepted, but the origin of the observed polarizations are not completely understood. Magnetically aligned grains have been proposed as the main polarizing mechanism by some authors, whilst a polarized source model and multiple scattering have been proposed by others. If the polarizations seen around young stellar objects arise from the alignment of dust grains in a magnetic field within a circumstellar disc, then assuming Davis-Greenstein alignment the inferred magnetic field is orientated parallel to the elongation of the disc. The observed circumstellar polarization could then be accounted for by the Davis-Greenstein mechanism, i.e. anisotropic extinction by elongated particles in a magnetic field, (discussed by Elsässer and Staude, 1978, for example. An excellent example of polarization attributed to this mechanism, but with respect to the magnetic fields in a number of galaxies is to be found in Scarrott, Rolph and Semple 1990). Such a mechanism (i.e. dichroic or selective extinction), which modifies the polarization state of light passing through the disc can then produce the observed pattern. As we move into the nebula, polarization due to scattering predominates.

The two competing mechanisms, (dichroic extinction and scattering), will cancel at some points where a change occurs between the predominating mechanisms, producing the observed null points which are found on either side of R Mon. However, this model fails to explain the rapid change in the observed position angle of R Mon that was found by Draper (1988) for example. The reason for this is that polarization by extinction assumes that the magnetic field is frozen-in to the plane of the circumstellar disc, and a change in the polarization position angle of the plane of the disc can then be interpreted as a change in the position angle of the disc itself. It is difficult to explain how such a circumstellar disc can reorientate itself in a time scale of years, months or even weeks. Bastien and Ménard (1988) also point out that dichroic extinction by aligned grains, cannot clearly explain the magnitude of the linear polarization that is found in such cases, without a very efficient alignment mechanism.

Simple Rayleigh scattering by small grains would yield a wavelength independent result for the measured polarization, and this was found in these measurements. Indeed it led Jones and Dyck (1978) to suggest that small particle sizes were in evidence in the vicinity of R Mon. However, and somewhat in contradiction of this explanation, Ménard, Bastien and Robert (1988) suggested that a wavelength independent relationship can be explained by scattering from relatively large particles with sizes comparable to the wavelength. It seems likely that a broad distribution of particles is to be found in the vicinity of R Mon and not merely particles of one particular size. If a power law size distribution is assumed then the effective grain size changes in proportion to the wavelength, giving wavelength independent polarization (see Warren-Smith 1979). Scarrott, Draper and Warren-Smith (1989) concluded that the observed polarization close to the star cannot arise from single scattering (of unpolarized light) from a central source. One of their reasons behind this, is that the pattern of polarization vectors lacks the required centrosymmetry that theory predicts, in the region close to R Mon itself. Such centrosymmetry is, however, what is observed within the extended nebula NGC2261.

Bastien and Ménard (1988) have also attempted to account for the polarizations observed in the past, by considering multiple scattering alone, within an optically thick disc with optically thin polar lobes. In the Bastien and Ménard model, radiation can only effectively escape from the source along the disc's polar axis. The radiation from the poles is then scattered by the optically thin lobes and illuminates the periphery of the disc where it is scattered again. This double, or multiple scattering model, will yield the band of polarization at R Mon which has been attributed to the presence of a disc. This interpretation helps to explain the simple aspects of most of the polarization maps so far obtained without resorting to using aligned grains and magnetic fields. Bastien and Ménard go on to conclude that such an explanation for the polarizing mechanism in operation, does not disprove the presence of magnetic fields around young stars, but they say, it shows that they are not efficient at aligning grains around stars such as R Mon. Ménard, Bastien and Robert (1988) detected circular polarization from the region around R Mon which helps confirm the idea that multiple scattering is indeed involved to some extent in the polarization process within the vicinity of R Mon. However, doubts are raised as to the validity of the Bastien and Ménard model, because Ménard *et al.* (1988) failed to detect the pattern of circular polarization around R Mon that the Bastien and Ménard model predicted. The model also appears to fail to explain the null points that are found in polarization maps of R Mon. This problem is not discussed by these authors, and yet it is an important phenomenon. A further problem with the model is that the change in the observed polarization position angle must be interpreted as a change in the disc orientation, which as we have already mentioned, is difficult to explain.

Gledhill (1991) has developed a model using a polarized source to interpret the polarization maps that are obtained from bipolar and cometary nebulae. He has been able to generate maps which yield the polarization pattern that we see in the extended nebula NGC2261. More importantly, the Gledhill model is able to explain such features as polarization null points, and the band of parallel polarization vectors

across the source star, (in this case R Mon). Such a model is developed without the need to consider polarization by aligned grains. Gledhill's model is also elegant enough, that it approximates to the polarized source model proposed by Elsässer and Staude (1978). The Elsässer and Staude model considers that light is funnelled into the lobes of an unresolvably small bipolar nebula, by an anisotropic distribution of dust very close to the source star. Gledhill is able to show that null points are found at the transition point between the region dominated by the polarized source, (the region of the parallel vectors), and the region where we find a centrosymmetric pattern of polarization vectors, (the nebula). The centrosymmetric pattern in the nebula can be explained as due to the scattering of light by dust grains in the nebula. Scarrott, Rolph & Tadhunter (1991) have also considered a polarized source model for the particular case of the PV Cephei/GM29 system and seem to be able to explain the polarizations that are seen in this cometary nebula.

How R Mon could be a polarized source must be examined. One explanation is that a mini-bipolar nebula is in evidence, too small to be resolved. This is a model first considered by Elsässer and Staude in 1978. The star itself is obscured by a dense disc, and so the illumination of the nebula comes from light from the lobes of this unresolved mini-bipolar. Gledhill suggests that this obscuration of the source star could be accomplished by a small scale circumstellar disc ~ 100 AU across. The important point here is not so much the size of the disc, but the fact that the disc is unresolvable. Models of YSOs which have a small-scale circumstellar disc around the YSO, and are located within a larger (interstellar) disc have been suggested by Cantó *et al.* (1981) for R Mon and Ward-Thompson *et al.* (1985) for R Cr A. Another possibility is that light from a "hot-spot" located close to the star illuminates the nebula. This hot-spot could be formed by a local concentration of matter. This matter could be in the form of small unresolvable clouds close to R Mon which as they orbit the source change the scattering geometry of light which appears to come from R Mon, causing changes in the observed polarization.

A polarized source interpretation also provides another important solution to the

problem of explaining R Mon. If R Mon is indeed behaving as a polarized source, then the observed polarization of R Mon, which was thought to be due to the circumstellar disc, can change on relatively short time-scales because the asymmetric illumination is restricted to small distances from the original source. How the disc could change its orientation so rapidly has been one of the main problems in designing a model which can explain the observed polarizations around R Mon. The polarized source model removes any need to consider that the polarizations seen close to the star are due to a large circumstellar disc, (though light already polarized close to object can naturally still be scattered off the disc). Thus we do not need to consider that the disc is changing its orientation at all.

The polarized source model is then the best for explaining many of the observed phenomena. The models of Gledhill (1991) and Scarrott *et al.* (1991) though use simplified cases, and do not take into account complex optical depth effects. Close to R Mon we expect to find an increased optical depth, the result of which will be to complicate the polarizing process, due to possible depolarization caused by multiple scattering, for example. What does seem certain though is that there are a number of factors influencing the final polarization that is measured around R Mon. Models which take into account such processes, need to be considered, but as yet have not been formulated. However, the models of Gledhill and Scarrott *et al.*, still provide the best explanation for what is occurring.

H α Results from R Mon

The H α measurements were found to be depolarized with respect to the continuum by only 0.1%, which within errors shows that the H α and continuum had the same polarization using a 10'' aperture, (see section 2.3.2). Such a result is fairly consistent with that obtained by Draper (1988) who also used a 10'' aperture in measurements of R Mon, and showed that the H α was depolarized with respect to the R waveband by only 0.7%, see table 2.5. (New measurements on Draper's data but using a smaller aperture confirm Draper's original result). Draper draws attention to the

fact that his measurements are based upon observations in $H\alpha$ and the R waveband which were taken two months apart so this *may* affect his final result, though the 1990 observations do not suffer from this problem.

In comparison however, Garrison and Anderson (1978) found the depolarization of the $H\alpha$ with respect to the R waveband of $\sim 3.5\%$. It is not clear though what size of aperture Garrison and Anderson used in these measurements. Aspin, McClean and Coyne (1985) also found a depolarization of $\sim 3.5\%$ with a rotation of $\sim 12^\circ$ in the position angle of the $H\alpha$ with respect to the continuum from spectropolarimetry. (The spectropolarimetry of Aspin, McClean and Coyne employed an aperture smaller to that of Draper, of $2.5''$ by $4''$ for their measurements).

Clearly then, the level of depolarization of the $H\alpha$ with respect to the continuum obtained by in this work is not consistent with that obtained by Aspin *et al.* (1985) or Garrison and Anderson (1978). Aspin *et al.* point out that the $H\alpha$, would have the same polarization position angle as the continuum if the hydrogen recombination region is close into R Mon and mixed with the polarization producing dust-grain region, which is what the data presented in this work seems to imply, in contrast to the result of Aspin *et al.* (1985).

If the data presented in this work and the results of Draper (1988) are still valid, then we may be detecting some change in the level of depolarization of the $H\alpha$ relative to the continuum. This could possibly indicate that the position of the hydrogen recombination front is moving, which may perhaps be explained if R Mon is experiencing a variable accretion rate as many T Tauri stars are believed to, (section 1.4.3). However this statement is highly speculative and non-conclusive given the problems with the 1990 observations and the gap in observations in Draper's work. The only way to confirm the results of Aspin *et al.* (1985) or to show a variability in the residual $H\alpha$ line polarization is for new observations in good and consistent seeing conditions to be made over a period of years.

R Mon H α and Continuum Measurements						
Reference	Waveband	P(%)	δP (%)	θ ($^\circ$)	$\delta\theta$ ($^\circ$)	Aperture (")
Garrison and Anderson (1978)	R	16.45	0.3	103.0	1.0	
	H α	13.12	0.6	106.0	1.0	
Aspin <i>et al.</i> (1985)	R	12.7	0.5	103.0		10
	H α	9.6	0.5	110		2.5 by 4
	Continuum	13	0.5	102		2.5 by 4
	Continuum	13	0.5	98		2.5 by 4
Draper (1988)	R	10.6	0.3	96.5	1.0	10
	H α	9.9	0.3	91.7	1.0	10
This work 1990 observations	Continuum	11.9	0.3	92.5	0.7	10
	H α	11.8	0.3	93.9	0.7	10

Table 2.5: H α measurements of R Mon with respect to the continuum or R waveband.

The Polarization Knot

The rapid rise and wavelength dependence of polarization found at the polarization knot is typical of that found in the reflection nebulae around many YSOs, and is consistent with the single scattering of light by predominantly small particles at the knot. Since the location of this knot is some 4–5" north of the intensity maximum of R Mon, the polarization mechanism in operation here may be less likely to be affected by the disc and optical depth effects associated with such a phenomenon, since the disc does not extend out this far.

The exact nature of this polarization knot is not as yet defined. It generally accepted by many previous authors that the cometary fan of NGC2261 is the northern lobe of a bipolar nebula, whilst the southern lobe remains essentially hidden. The presence of the knot, however, must still be accounted for, and maybe what we are seeing is the northern lobe of a second smaller bipolar nebula within the larger cometary fan. Aspin *et al.* have also found that there are small regions to the north and south of the intensity maximum, of higher polarizations than at R Mon itself, and have termed these the "mini-lobes". It is a pity then, that they did not

draw a different conclusion from their aperture dependence tests. Brugel, Mundt and Bührke (1984) have also discovered emission-line nebulosities situated north and south of R Mon. The northern outflow, which they define as extending from 4–14" north from R Mon, is shown to have a mean heliocentric velocity of $-67 \pm 10 \text{ km s}^{-1}$ in the [SII] line, indicating that it is moving towards us; the southern counterpart is found to be moving away from us with a velocity of $+168 \pm 10 \text{ km s}^{-1}$. This helps to confirm the hypothesis that what we are seeing is a second, smaller bipolar nebula. (This secondary bipolar must not be confused with the unresolved "mini-bipolar" which we have considered as a possible explanation for R Mon acting as a polarized source). Since extended nebulae such as NGC2261 are formed from the outflow phase of a pre-main-sequence star, the outflow will take place over some period of time. It will take time for matter to leave the star and become resolvable. Matter close to the star, just beginning its journey into space, will therefore be unresolvable. If there is more than one stage of outflow, then we might expect to see bipolar lobes with different sizes and different distances from the source star. This could therefore explain the polarized source, the knot and the cometary fan. In other words, unresolvably close to the star material forms what we consider to be the polarized source (perhaps in the form of a tiny mini-bipolar), whilst further out a larger mini-bipolar forms, whose northern lobe we observe as the polarization knot. Further out again, the earliest phase of outflow is seen as the cometary fan. This would thereby represent three discrete phases of bipolar outflow.

2.4.2 The Polarization Minimum

At the point of minimum polarization, and in agreement with findings of Zellner (1970), it is found that the polarization of R Mon is not seen to vanish, but to be near a value of 10%, almost independent of wavelength. Zellner though, centred his aperture on the intensity maximum of R Mon, which yields a slightly higher value for the polarization than an aperture placed directly upon the polarization minimum itself. However, since the value of the polarization does not change greatly as we

approach the minimum of the curve of polarization against distance from R Mon (figure 2.4), the basic conclusion given by Zellner is still valid.

The location of the polarization minimum is in the optically thick circumstellar disc close to R Mon. As such, the explanation for the polarization at R Mon may also be applied to those observed at the polarization minimum. The fact that the intensity maximum is not found at the polarization minimum could possibly be explained by the fact that the source of illumination of NGC2261, i.e. R Mon, is not located at the observed intensity maximum. Cohen and Schwartz (1983) discovered that an infrared source (IRS), was located $3.6 \pm 0.2''$ east and $2.2 \pm 0.6''$ south of the apex of the optical fan; this IRS is believed to be the true illuminator. Circular apertures of $3''$ in diameter were then placed on the datasets with the best seeing conditions and best image scale, (the March 1988 I dataset, and the January 1991 V dataset), at the approximate position of the IRS associated with R Mon. The measured polarizations were found to be $7.2 \pm 0.2\%$ at $101.9 \pm 0.8^\circ$ in the 1988 I dataset; and $8.7 \pm 0.5\%$ at $73.7 \pm 1.5^\circ$ in the 1991 V dataset. This compares with the values found at the minimum of the polarization against distance from R Mon curve, the “polarization minimum”, of $10.0 \pm 0.3\%$ at position angle $102.9 \pm 1.0^\circ$ in the 1988 I dataset; and $9.1 \pm 0.3\%$ at $78.1 \pm 1.0^\circ$ in the 1991 V dataset. Thus, the polarization at the IRS position is somewhat lower than that at the polarization minimum. The IRS is merely $\sim 3\text{--}4''$ east of the point that has previously been termed the polarization minimum. It therefore seems likely that the illuminating optical source which is identified with the IRS of Cohen & Schwartz, is located $\sim 4''$ south east of the intensity maximum. The likely explanation for the fact that polarization at the IRS is lower than that at the “polarization minimum”, is that we are seeing more of the source directly, and so are measuring less scattered light than would be in evidence elsewhere. Further investigations though are suggested to accurately confirm that a minimum polarization is indeed found for the IRS itself.

2.4.3 NGC2261

It is interesting to note that measurements made out in the nebula of NGC2261 follow the same intrinsic pattern as measurements made upon the polarization knot; i.e. wavelength dependent polarization which increases as we approach longer wavelengths, and a constant value for the position angle. Such a wavelength dependence of polarization is consistent with a population of scatterers whose effective size is less than the wavelength of the incident radiation (see Warren-Smith 1979). Thus as we go to longer wavelengths the effective cross-section of the particles appears smaller and a higher polarization results. The optical depth within the nebula is greater than might be expected at R Mon itself, where there has been much discussion on the presence of an optically thick disc. Thus, single scattering is a more likely result than the multiple scattering that might be expected if the density of material were greater. This centrosymmetric pattern breaks down as we approach R Mon. Null points are found close to, and either side of R Mon suggesting perhaps that more than one polarizing mechanism is in evidence within the nebula, and perhaps especially close to R Mon itself, and that these mechanisms are competing with one another and cancel each other out at certain points.

Figure 2.12 and figures 2.13 to 2.16 seem to suggest that close to R Mon there is a strong correlation between the polarization in NGC2261 and the polarization at R Mon. As we move further away from R Mon (30–40'') a more uniform level of polarization seems to be found, and no strong correlation is observed.

This may perhaps be explained by the fact that the parts of the nebula close to R Mon are unable to “see” the source directly due to obscuration, and a polarized source contributes to the observed polarizations. As a result, the nebula close to R Mon reflects changes in the illumination and polarization of the obscured region in the proximity of the illuminator. Further away from R Mon (up the nebula axis) however, the nebula is able to “see” more of the source directly, and the contribution from the polarized source component diminishes. As a result, the polarizations in the nebula tend towards simple scattering.

The existence of the extended nebulae NGC2261 can be explained by considering the outflow the R Mon has undergone over time. The material ejected from the pre-main-sequence object has eventually covered a large area. However, when considering the polarization knot, reference was made to the possibility that R Mon is itself a mini-bipolar. What this may show is that R Mon is continuing to undergo spasmodic or episodic outflow phases.

2.5 Conclusions

New observations of the peculiar variable cometary nebular R Mon/NGC2261 have been presented, both with observations and reductions made by the author, and comparing these datasets to datasets previously reduced at different times by different astronomers with the Durham Polarimetry Group. It has been shown that in previous works, the large sized apertures that have been used to make measurements upon R Mon are including the effects of a polarization knot, located some 4-5" north of the intensity maximum of R Mon. The knot is strongly wavelength dependent, which has never been discussed by previous authors, and measurements made which include effects from this knot become more inaccurate with increasing wavelength, as the effect of the knot grows. Most observations done with apertures centred upon the intensity maximum of R Mon have included this important feature. It can no longer be accepted, therefore, that the polarization of R Mon is aperture independent.

The polarization of R Mon has been shown to change rapidly with time, whilst the polarization in the nebula does not appear to. The polarization at the knot and within the nebula is strongly wavelength dependent, which is consistent with simple scattering from particles whose effective size is less than the wavelength. It seems likely that the polarization at and around R Mon is due to competing polarizing mechanisms, perhaps from a polarized source and from scattering. A polarized source model not only removes the need to consider extinction in a circumstellar disc by aligned grains as the main polarizing mechanism, it also helps to explain

the rapid change in the observed polarization of R Mon with time, and thereby also explain the rapid change in the apparent position angle of the disc. It further seems likely that R Mon is itself a mini-bipolar, and that the polarization knot is the actually the northern lobe of a small-bipolar. R Mon has thereby undergone at least three phases of outflow perhaps due to the sort of variable accretion rate that many YSOs are believed to undergo, and which may still be continuing. Attempts to validate the explanations provided in this work to explain the polarization knot and the polarization minimum, are best investigated by observers who are able to obtain data on R Mon in excellent seeing conditions, and preferably with the better image scales that would be available on larger telescopes. It seems likely, however, that the polarization minimum is due to the presence of the infrared source that is the true illuminator of the R Mon optical intensity maximum, which is located in a south-easterly direction from R Mon.

Chapter 3

THE POLARIZATION OF R CrA

3.1 Introduction

The Corona Australis dark cloud complex is located at a relatively nearby distance of some 129 parsecs (Marraco and Rydgren 1981), and covers an area of more than one square degree of the sky. The CrA cloud also contains many of the signposts to recent star formation, such as Herbig-Haro objects, compact HII regions and T Tauri stars. Many of these T Tauri stars also show large infrared excesses (Glass and Penston 1975), a phenomenon explained by many as due to circumstellar clouds of dust around these stars which reradiate energy from the embedded star in the far infrared, and are indicative of a recent and on going star formation process. Deep infrared surveys, such as those of Taylor and Storey (1984) and Wilking *et al.* (1985), have detected a whole cluster of young embedded stars within the Corona Australis dark cloud which confirm that star formation is still taking place.

The region is dominated by two reflection nebulae. The larger nebulosity is NGC6726/7 which is illuminated by the stars TY CrA and HD176386 (Warren-Smith 1979), and the other is the cometary nebula NGC6729. Most of the mass of this cloud is thought to be in the ^{12}CO cloud which is centred on the region surrounding the star R CrA, and has a radius of some 1.3 parsecs (Vrba *et al.* 1976a).

Vrba *et al.* (1976a) put the mass of this cloud at $\sim 10^5 M_{\odot}$, with the cloud extending over 6pc in length. Knacke *et al.* (1973) obtained optical and infrared photometry of known stars in the region and suggested that the unusually large infrared excesses in some of the stars in the Corona Australis dark cloud indicate extreme youth, and that they are less than 10^6 years old. The ^{12}CO maxima is located at TY Cr A, with a weaker peak at R Cr A. H_2CO , CS, HCN and HCO^+ peaks are located at R Cr A, which yields a high core density of some $250\text{--}520 M_{\odot}$, Cruz-Gonzalez *et al.* (1984).

The pre-main-sequence emission line variable star, R Corona Australis, is located at the apex of the fan-shaped cometary nebula NGC6729; position $\alpha = 18^{\text{h}}58^{\text{m}}32^{\text{s}}.5$, $\delta = -37^{\circ}2'8''$ (1950). Schmidt discovered the variable star R Cr A, and T Cr A, and suspected that the the nebula NGC6729 was itself variable. Knox-Shaw (1916) observed structural changes within the nebula with time, and indeed both he and Reynolds (1916) had little doubt by this time that the nebula was indeed variable like the cometary nebula NGC2261 associated with the variable star R Mon. Bellingham and Rosano (1980) examined some 200 photographic plates of NGC6729 in the Harvard plate collection taken in Peru from 1898 to 1948. They were able to establish from these that the structures within the nebula irregularly repeat themselves, and the source of illumination must therefore be random. This discovery is interesting when it is compared to the deductions of Lampland (1931), on the variability of NGC2261.

The major source of illumination within the nebula NGC6729 is R Cr A, as is illustrated polarimetrically by Ward-Thompson *et al.* (1985), (and maps presented later in this chapter), though some contribution from the associated star T Cr A is found near to the star T Cr A. The spectrum of the cometary nebula also closely mimics that obtained from R Cr A, classified as an Ae star, (Herbig 1960), adding further evidence to the hypothesis that R Cr A is the illuminator of NGC6729. Graham and Phillips (1987) go on to show how the slight differences between the spectrum of the nebula and that taken from R Cr A can be explained by taking into account the increased light travel time for the reflection of light from R Cr A off the dust

in the nebula. When observing the nebula they conclude, one is observing the star as it was two or three days earlier. The most extensive luminous dust emission in the Corona Australis dark cloud is excited by R Cr A (Wilking *et al.* 1985; Cruz-Gonzalez *et al.* 1984). Wilking *et al.* estimate the far infrared luminosity of R Cr A at $\sim 40L_{\odot}$ (20–100 μm), and derive a bolometric luminosity of $120L_{\odot}$ (with an error of $\pm 40\%$), which is in agreement (within errors) to the luminosity of $140L_{\odot}$ calculated by Cruz-Gonzalez *et al.* (1984).

Bellingham and Rosano (1980) looked at the long-period variations in brightness for a number of T Tauri-like stars, including R Mon and R Cr A. The data for R Cr A, and indeed other stars in the Corona Australis dark cloud, was taken from The New Zealand Variable Stars Circulars, for a time period between 1928 and 1971, yielding some 2100 observations on R Cr A. Their conclusions are that R Cr A has a periodic variation of about 1500 days in length and about 0.5 magnitudes in amplitude. This variation is then superimposed upon a decrease of 0.75 magnitudes over the entire period of the observations. They interpret the results as due to variations in the diffuse envelopes or circumstellar shells surrounding the star. Bellingham and Rosano go on to state that it would be useful to follow the day-to-day variations in R Cr A, and indeed in other similar variable stars, to understand better the shorter term variations. The data available to them at the time allowed no such analysis. Graham and Phillips (1987) made CCD observations of R Cr A and NGC6729 over a 23 day period from March to April 1984. They show that measurable changes in the surface brightness of the reflection nebula occur over intervals as short as 24 hours. During these 23 days of observations, R Cr A brightened by some 1.3 magnitudes. In one 24 hour period, structures within the nebula changed in brightness by 20–30%, whilst spectroscopically the red/blue emission peaks changed within a period of only 24 hours. Thus R Cr A is a rapidly varying star.

Early polarization measurements within the R Cr A region were made by Whitney and Weston (1948), in July 1946. They deduced that most of the scattered light within NGC6729 comes from R Cr A, and measured a general maximum polariza-

tion in the nebula of 20%, with a mean polarization of some 15%; (though some points went up as high as 35%). Serkowski (1969b) noted a rapid change in the polarization of R Cr A over a period of 5 weeks, changing from 9% to 18% in the blue spectral region. Such a change should not be so unexpected when the results of Graham & Phillips and Bellingham & Rossano are taken into account. Serkowski also shows that the polarization of R Cr A seems to increase towards shorter wavelengths. Though some of these results are important, Serkowski uses apertures ranging between 11" and 47" for his polarization measurements, a fact which must cause polarization contamination from the nebula in any measurement which is supposed to be based on R Cr A alone. Ward-Thompson *et al.* (1985) in making their polarization measurements, used a circular aperture of 5" diameter to avoid such contamination, and measurements of the polarization of R Cr A by the author in the work presented here will follow this lead and also use an aperture of 5" in size.

Vrba, Strom and Strom (1976a) mapped the magnetic fields of five dark cloud complexes including the Corona Australis dark cloud. This was done by taking measurements of the linear polarization of background stars, which totalled some 76 for the Corona Australis cloud survey. Their conclusion was that there is a rather uniform degree of alignment throughout the cloud, with the magnetic field and the cloud material being closely associated. There is however, one drastic twist in the magnetic field, where the field undergoes a sharp 30° turn. This twist occurs in the region of star formation associated with R and T Cr A, with the field having a position angle near 90° west of R Cr A, changing to near 120° east of the two stars. It is interesting that the twist in the magnetic field is found at a point of star formation, which is also the point in the cloud nearest to the galactic plane where the highest visual obscuration and gas density in the entire complex is to be found.

Vrba (1977) using the results from Vrba *et al.* (1976a) and also Loren (1979), have concluded that the star formation within the Corona Australis dark cloud has resulted primarily from the self-gravitational collapse of the cloud, guided by the magnetic field, until it reaches the part of the cloud nearest to the galactic plane, into

what is known as a magnetic Rayleigh-Taylor instability, (see Shklovskii (1978) for example, and section 1.2.1). The basic scenario though, is as follows. A depression has occurred in the galactic magnetic field, creating a dip in the field-lines. Under the influence of gravity, matter moves into the dip in a direction which is towards the galactic plane. The inflowing matter cannot move across the field lines because it is highly ionized, and it cannot move back out of the dip because of gravity. The density of matter increases in the dip, and star formation, or more particularly in this case, the birth of R Cr A can take place. This theory of star formation in molecular clouds, seems to be confirmation that the hypothesis of Vrba (1977), is indeed correct, and that a magnetic field is responsible for the formation of the Corona Australis star forming region. This is most clearly demonstrated by the sharp turn in the magnetic field lines, which we identify as the magnetic well found in the Cr A cloud close to the galactic plane, in the linear polarization mapping of Vrba *et al.*, (1976a). The fact that the most dense region of the cloud is also located at R Cr A (the magnetic well) is further evidence.

The Herbig-Haro object, HH100 is located some 80" southwest of R Corona Australis. Strom, Strom and Grasdalen (1974a,b) found a bright near-infrared source some 20" east of HH100, which is a good candidate for the HH100 exciting star. However, R Cr A itself has been suggested as a viable candidate for the exciting star of HH100 (Wilking *et al.*, 1985) since R Cr A, HH99, HH100 and HH101 all lie roughly collinear with each other. Hartigan and Graham (1987) disagree with the interpretation of Wilking *et al.* pointing out that the HH objects HH99, HH100 and HH101 all lie on a line which is highly inclined to the direction of outflow from R Cr A, and instead suggest that HH100IR is the exciting source for HH99, HH100 and HH101. Hartigan and Graham do, however, point out that R Cr A is the likely exciting source for HH104 which lies to the east of R Cr A and is therefore associated with the blueshifted outflows more so than the other HH objects.

3.2 Observations

Observations were made of R Corona Australis and subsequently part of the associated nebula NGC6729, at the f/15 Cassegrain focus of the 1 metre Jacobus Kapteyn Telescope (JKT), on the island of La Palma in The Canary Islands over a period of some 6 days from 30th May to 4th June 1990. Observations were made in the B, V, R and I wavebands using the Durham Imaging Polarimeter. The FWHM seeing at the time the observations were made has been measured as 2.1–2.8". The author has reduced the above datasets, and also data taken at the f/18 Cassegrain focus of the 1.9 metre telescope of The South African Astronomical Observatory on 25th May 1985 in H α by observers from The Durham Polarimetry Group, but which had never been previously reduced. The seeing at the time the observations were made was some 1".

3.3 Results

3.3.1 Polarization Maps

Figures 3.1 to 3.3 show the distribution of linear polarization as measured for R Cr A and part of NGC6729 in the V and R wavebands.

The integration bins for the polarization map are 3 pixels square, (3.6" square), and moved on in steps of 2 pixels in each direction. The most striking feature is the centrosymmetric pattern of polarization vectors which is found within 30" of R Cr A. Across the intensity maximum of R Cr A, we find a band of polarization vectors running in a north to south direction, whose degree of polarization is clearly not zero. To the north and south of R Cr A, at a distance of $\sim 10''$ from R Cr A (see figures 3.1 and 3.2), there are points where the polarization falls off towards zero. These *null* points are very reminiscent of R Mon. Moving into the nebula of NGC6729, the polarizations are seen to rise in parts to levels in excess of 30%. The intensity contours on the maps are shown to be elongated away from R Cr A, in a south-easterly direction. This is due to the presence of what has been interpreted

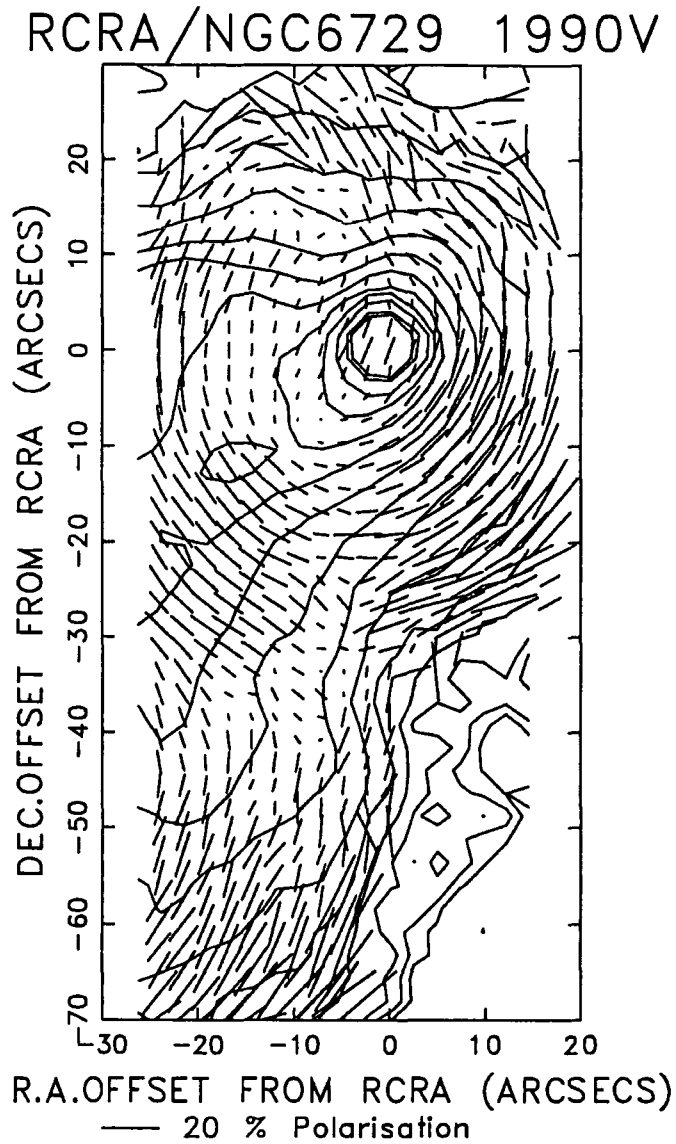


Figure 3.1: An intensity contour and polarization map of the RCrA/NGC6729 cometary nebula from the 1990 V dataset.

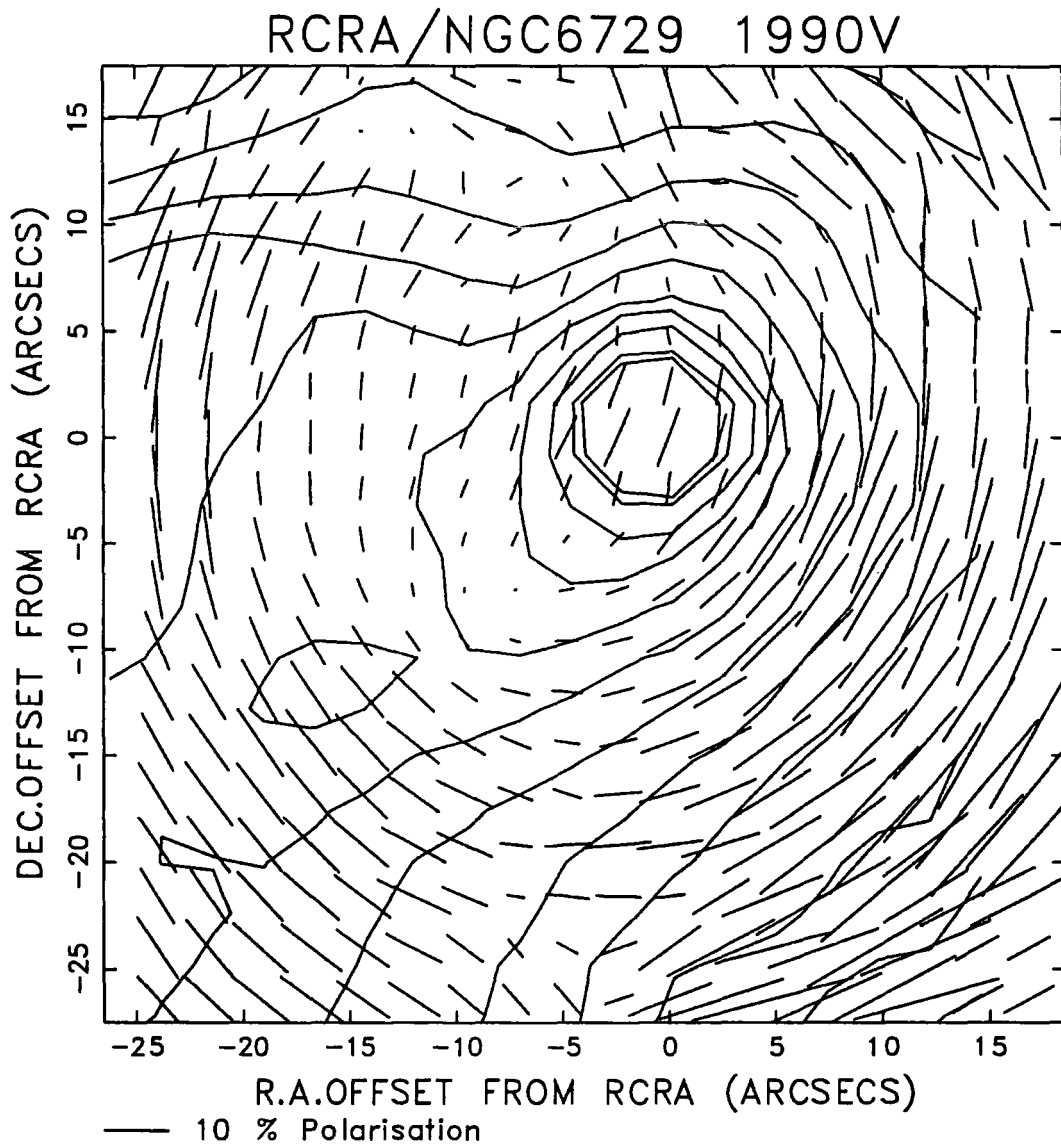


Figure 3.2: An intensity contour and polarization map of the R Cr A/NGC6729 region close to R Cr A. (1990 V dataset).



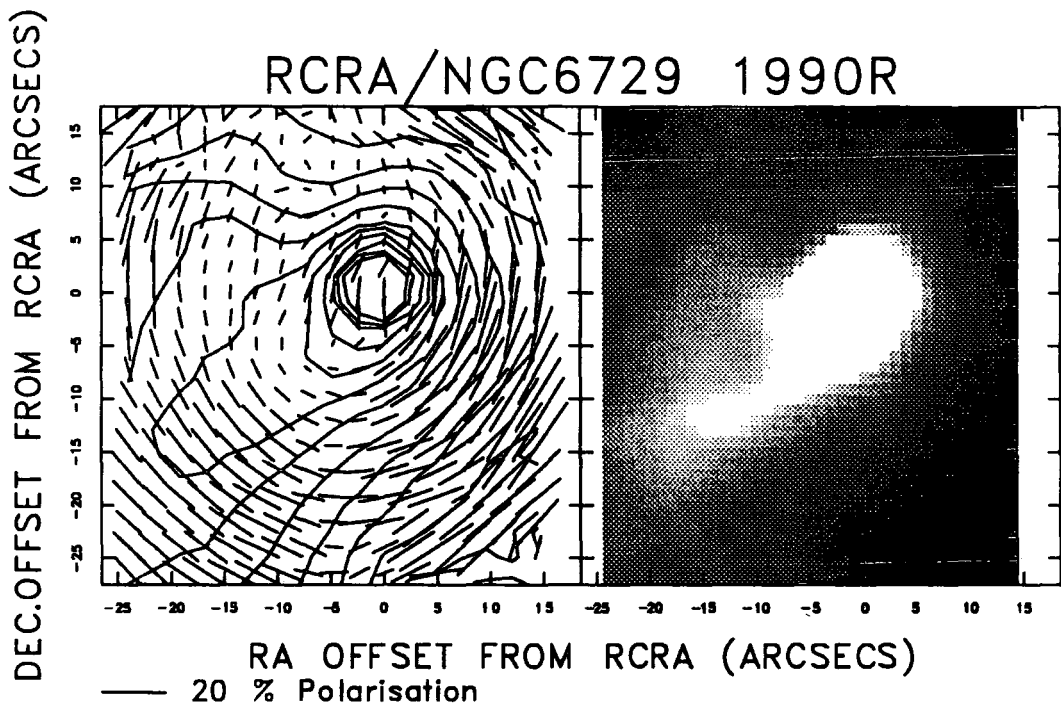


Figure 3.3: An intensity contour and polarization map of the R CrA/NGC6729 cometary nebula from the 1990 R dataset, together with a greyscale intensity image of the same region.

in the past as a jet-like nebulosity. As we move further south and east from R Cr A, a new centrosymmetric pattern is located.

Much of the work by Ward-Thompson *et al.* (1985) was concerned with jet-like structures that were seen emerging from both R and T Cr A. These authors obtained a far larger field in observations of NGC6729 than the author was able to obtain in the datasets which are discussed here, and so a greater degree of emphasis could be placed on the nebulosities between the two YSOs by Ward-Thompson and his co-authors. The main jet-like nebulosity is seen to emerge east of R Cr A and extend away from the object in a south-easterly direction. Ward-Thompson *et al.* deduced from their observations that the region between R and T Cr A consists of a series of “continuous loop-like structures” which “appear to to be attached to the jet R1”. (Where R1 is the main south-easterly running jet-like nebulosity that is observed both in the greyscale intensity image presented (figure 3.3), and from the intensity contour plots on the polarization maps (figures 3.1 to 3.3). Figure 5 of Cohen *et al.* (1984) clearly shows the complex nebulosity and loop-like structures that that envelope R and T Cr A. This plate is also good for showing the relative positions of R & T Cr A, and HH100.

3.3.2 Synthesised Aperture Polarimetry

When measuring the polarization of R Mon in chapter 2, much emphasis was placed upon the size of the aperture used to make measurements. It was shown that a highly polarized knot, possibly the northern lobe of a mini-bipolar nebula, was to be found $\sim 4\text{--}5''$ north of the R Mon intensity maximum. (This mini-bipolar must not be confused with any smaller, unresolvable mini-bipolar, that has been suggested in polarized source models to account for the observed polarizations). The accuracy of measurements made upon R Mon when using $10''$ sized apertures was put into question because the knot was included within the aperture. In order to check if any such phenomena is present in the proximity of R Cr A, simulated circular apertures of $5''$ in diameter were placed upon the data and moved in steps of 2 pixels in

the x-direction, and 2 pixels in the y-direction (2.44" by 2.44"), along the axis of the cometary nebula. This was taken initially to be approximately north-east to south-west according to the description of the R Cr A system by Ward-Thompson *et al.* (1985). Plots of polarization against distance from R Cr A in arcseconds are presented in figure 3.4 in the V, R and I wavebands.

Apertures of 5" in size were also placed in a line running in an east-west direction, again placed 4 pixels apart, as a further check of the data (in figure 3.5). This was done, for as will be shown in section 3.4.3 the true nebula axis runs in an east-west direction.

The results of figures 3.4 and 3.5 show that unlike R Mon there is no evidence of a highly polarized feature within the close proximity of the intensity maximum of R Cr A. Therefore it is safe to adopt an aperture size for measuring R Cr A in the range of $\sim 3\text{--}5''$ (or larger), without the fear of including some other polarization feature. In figure 3.4 which shows the change in polarization along the axis defined by Ward-Thompson *et al.* in the V and R wavebands for example, the polarization at the intensity maximum is found to be generally higher than in the surrounding nebula within 15" of R Cr A, whilst in the I waveband the polarization is more on a par with the local background nebula polarization. As we look to the southwest, the polarization drops to some level close to zero at $\sim 10''$ south-west of R Cr A in the V waveband (for example). When we look at the polarization map of the V data, for example, a null point in the polarization is clearly seen at this distance from the intensity maximum of R Cr A. In figure 3.5 which shows the polarization change along the east-west nebula axis defined in section 3.4.3, it is seen that the polarization is fairly uniform within $\pm 5''$ of the R Cr A intensity maximum. At a distance of $\sim 5''$ west of R Cr A the polarization begins to increase gradually to levels of $\sim 20\%$ as we move west of the R Cr A intensity maximum.

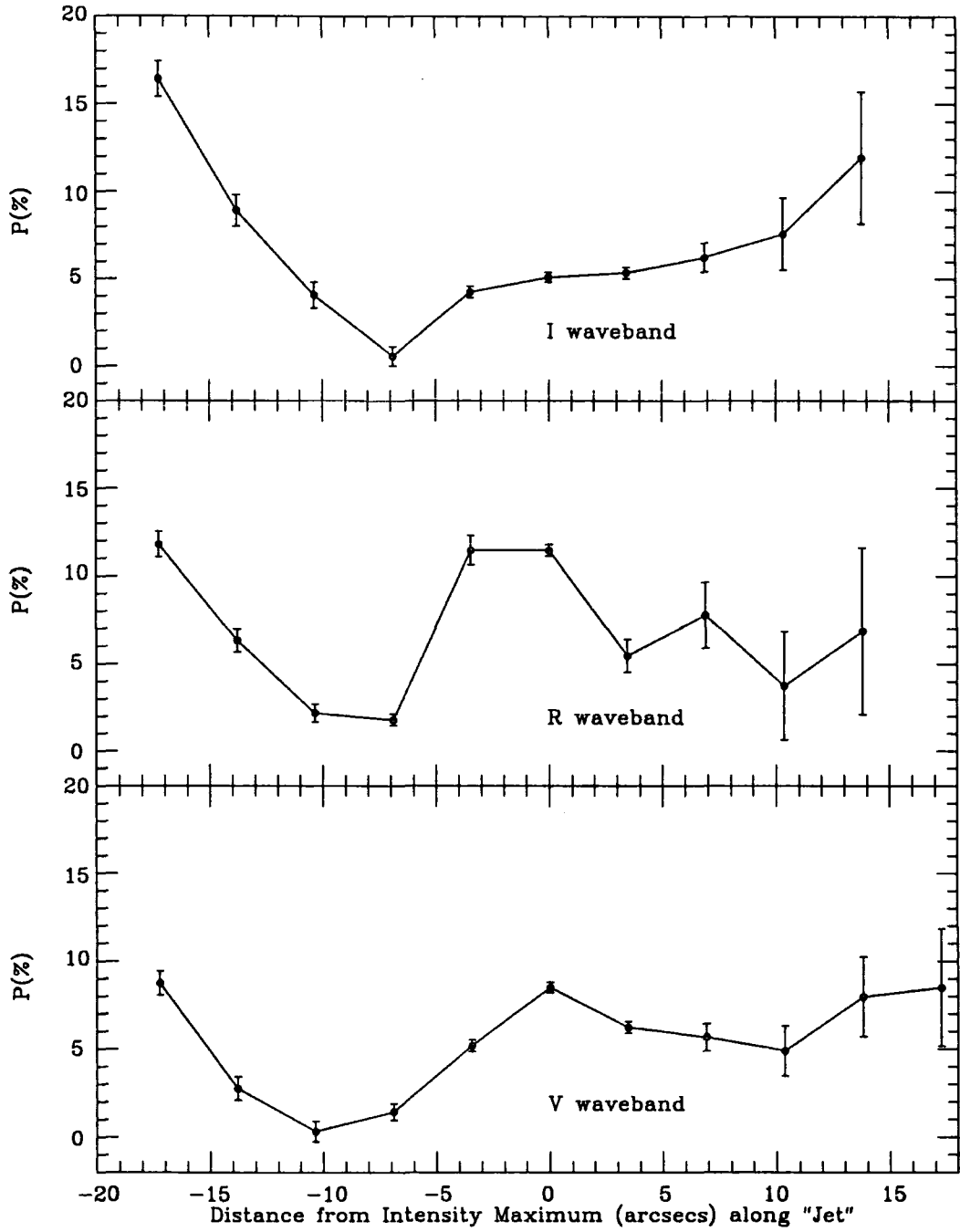


Figure 3.4: The variation of polarization with distance from R Cr A (along the "jet") from north-east to south-west of R Cr A.

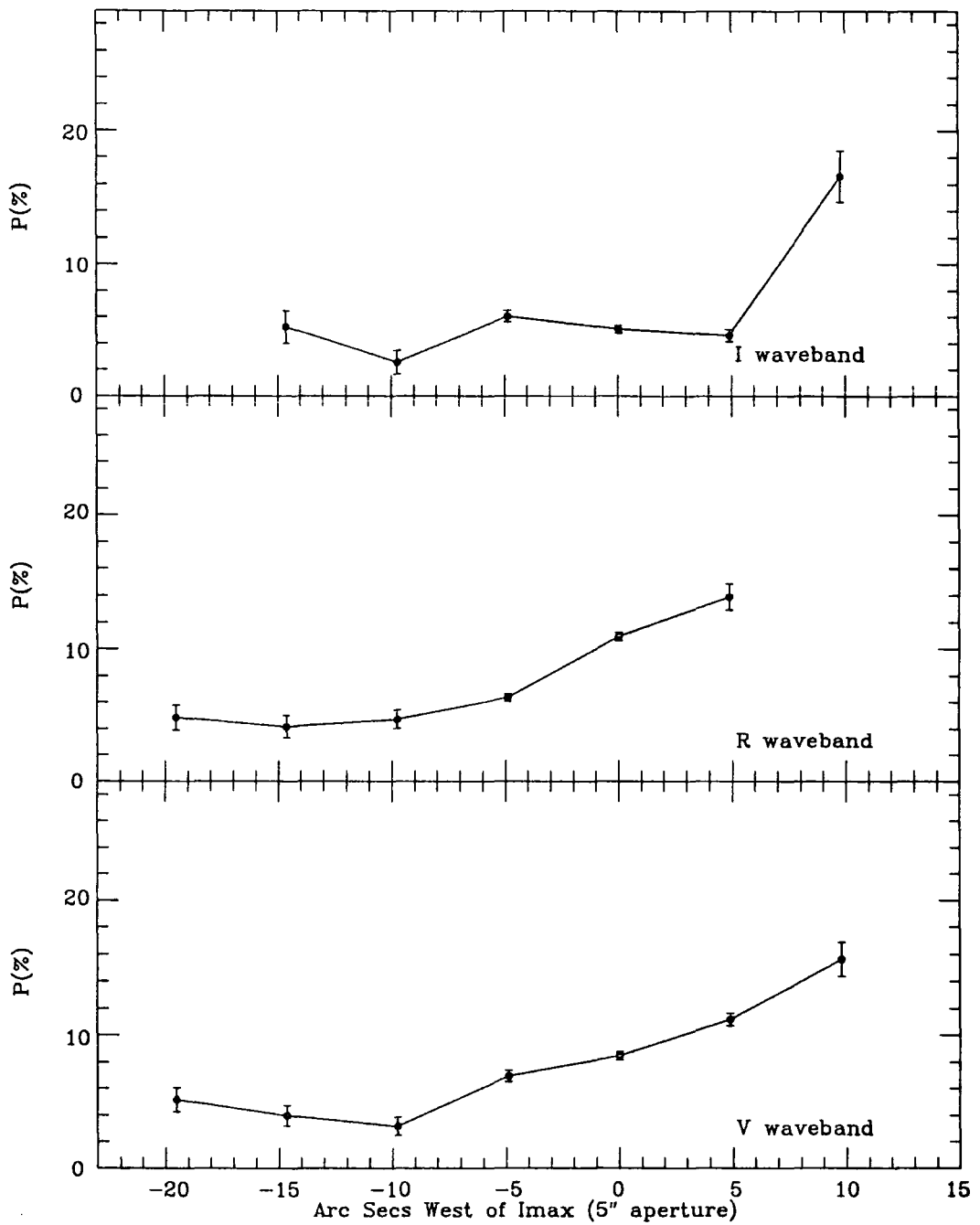


Figure 3.5: The variation of polarization with distance from R Cr A along a line east-west of the R Cr A intensity maximum (I_{\max}).

The Polarization of R Cr A

In the chapter related to the analysis of data concerning R Mon and its associated cometary reflection nebula NGC2261, much emphasis was placed upon how critical the size of aperture used was, when making polarization measurements upon R Mon. To some extent the same philosophy must be applied when considering the polarization of R Cr A. Ward-Thompson (1984) pointed out how one author had made measurements of R Cr A using an aperture of as much as 47" in size. Such a large aperture will include large parts of the nebula, and due to cancellation effects, or superposition, invalid measurements of R Cr A will result. So as to exclude large nebular effects, and so as to be able to compare the new data with Ward-Thompson's, an aperture size of 5" will be used throughout the data, (since this was also the aperture size used by Ward-Thompson).

In order to check to see whether this R Cr A reveals any aperture dependence of polarization, and also in an attempt to confirm the results obtained from figures 3.4 and 3.5, apertures ranging from some 3" up to 20" were placed upon all the available datasets, and the results in three of the datasets are presented in figure 3.6.

When changing from measurements of the polarization of R Cr A with a 3" circular aperture, to those measurements made with a 5" aperture, figure 3.6 shows that there is some small decrease in the resultant polarization. As the aperture size is increased from 5" up to 10", the resultant polarization is found to be generally constant with aperture size. In fact we find that a change in the polarization of less than 1.1% resulted throughout the datasets. For example, in the B waveband obtained on 4th June 1990, the polarization changed from some $9.0 \pm 0.4\%$ with a 5" aperture, to $7.9 \pm 0.4\%$ with a 10" aperture; a change of 1.1%. This was the largest measured change, and is itself not greatly significant. At the longer wavelengths, in this case the I waveband obtained in 1990, a change of only 0.4% resulted. The polarization in the V and R wavebands changed by only 0.3% and 0.4% respectively. In other words, the polarizations are essentially the same when the errors are taken into consideration. This result is also consistent with the information gained from

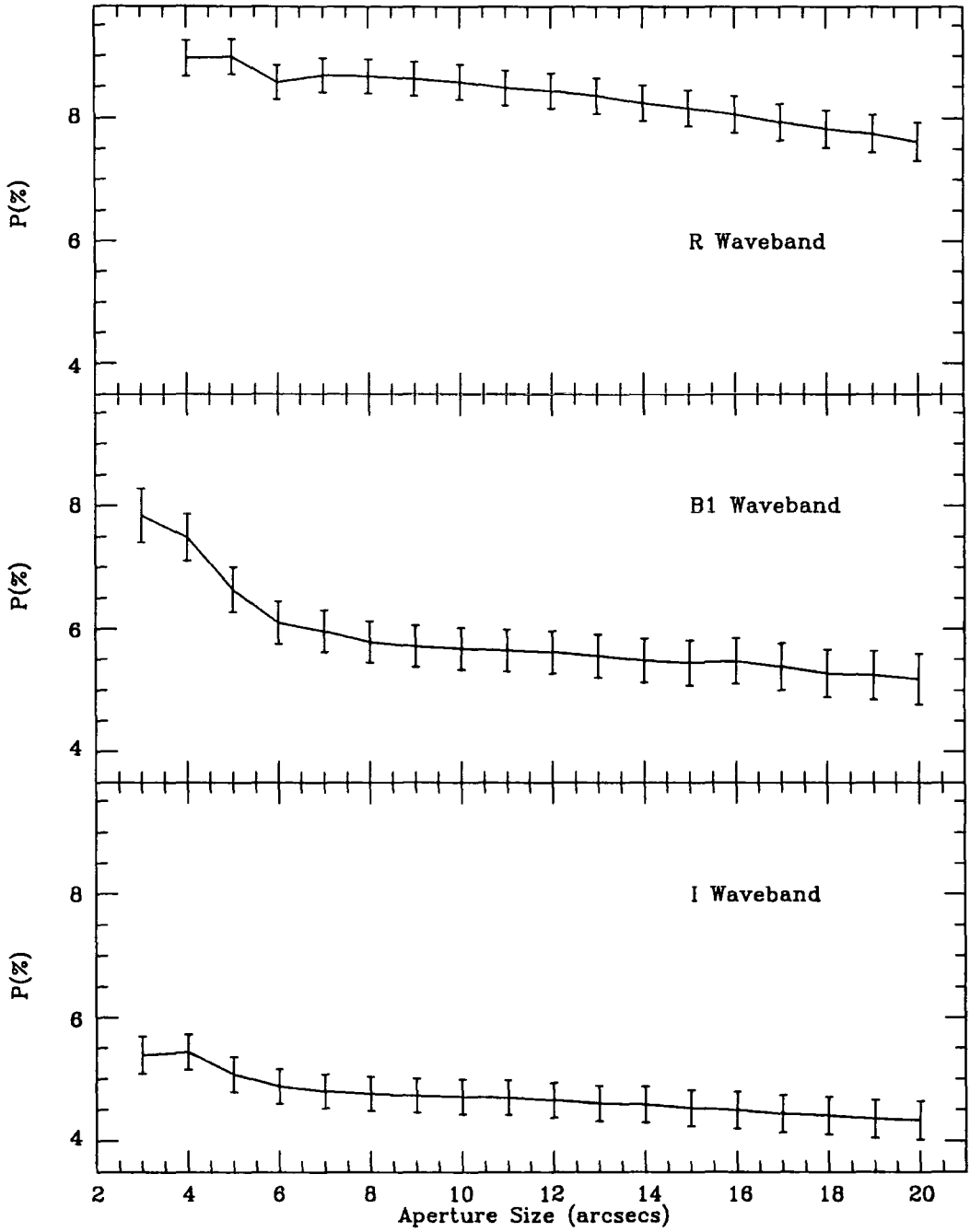


Figure 3.6: The variation of measured polarization at the R Cr A intensity maximum with aperture size.

the plots of polarization against distance from R Cr A, i.e. that no polarization features near R Cr A are contributing to the measured polarization of R Cr A.

The H α data from 1985, meanwhile, had a change of some 0.3% when changing from a 5" to a 10" size. It seems clear then, that there is little difference between the polarization measured in a 5" aperture, and that measured in an 10" aperture. Thus, it may be declared that measurements upon R Cr A are aperture independent over the range of aperture sizes used, and in further confirmation of the results obtained from figures 3.4 and 3.5, it is safe to adopt the use of a 5" aperture in polarization measurements of R Cr A.

Measurements were thus made with a 5" diameter circular aperture centroided on the intensity maximum of R Cr A. The most remarkable thing to come from these polarization measurements, is the large change in polarization which is found in the B waveband over in period of almost 24 hours (see table 3.2 and table 3.1). A measurement made in the B on the 3rd June 1990 (hereafter B1) yields a polarization of $6.6 \pm 0.4\%$, at a position angle of $166.5 \pm 1.6^\circ$. The observations made almost 24 hours later in the B waveband (hereafter B2) have a measured polarization of $9.0 \pm 0.4\%$ at a position angle of $160.8 \pm 1.3^\circ$.

Any relationship between wavelength and the measured polarization for R Cr A, is not so easy to define because of this rapid change that has occurred between the measurements B1 and B2. The B waveband was the only waveband where observations were made on different nights, and so it is not possible to check the data to see if changes occur at other wavelengths as well. It does seem interesting though, that there is an almost a wavelength independent relationship between the B2 observations and the R & V observations, which have a mean polarization of $8.8 \pm 0.2\%$. The polarization measured in the I waveband is somewhat less than that obtained in the R & V, at $5.1 \pm 0.4\%$.

R Cr A: Observational Details		
Date of Observations Total Exposure (secs)	Waveband	Approx Local Start Time
30th May 1990	R	04:49
1st June 1990	I	05:02
2nd June 1990	V	04:48
3rd June 1990	B(1)	05:08
4th June 1990	B(2)	04:08
26th June 1985	H α	05:00

Table 3.1: Details the 1990 (& 1985) observations of R Cr A.

R Cr A Intensity Maximum 5'' aperture				
Waveband	P(%)	δP (%)	θ ($^{\circ}$)	$\delta\theta$ ($^{\circ}$)
R	9.0	0.3	179.4	0.9
I	5.1	0.3	179.2	1.6
V	8.5	0.3	159.6	1.0
B(1)	6.6	0.4	166.5	1.6
B(2)	9.0	0.4	160.8	1.3
H α	6.4	0.3	206.5	1.9

Table 3.2: Aperture polarimetry with 5'' apertures centred at the R Cr A intensity maximum.

The Reflection Nebula NGC6729

The polarization maps are concentrated in the region around R Cr A, and as a result of this a large portion of the nebula has not been mapped in these observations. The length of the polarization vectors on the maps shown indicate that the polarization rises up to levels of over 30% in certain parts of the nebula, though levels of 10%–20% are more normal. Apertures of 5" in size were placed at a position of $\sim 18''$ (15 pixels) south of the R Corona Australis intensity maximum, in order to obtain measurements of the polarization here. This action, now places the aperture into the the centrosymmetric pattern of polarization vectors which is found around R Cr A. The measured polarization was then found to be $\sim 34\%$ in the B waveband, for example.

3.4 Discussion and Interpretation

3.4.1 NGC6729

The most striking feature of the polarization maps is the centrosymmetric pattern of polarization vectors which are found surrounding R Cr A (figures 3.1 to 3.3). Normals to these vectors indicate R Cr A as the chief illuminating source in the extended nebula NGC6729. This confirms what has been suggested by many authors before, and shows that the statement of Dibai (1971) is in error when he classifies NGC6729 as a nebula which has no star associated with it. (See section 1.7).

To the south-east of figure 3.1 a second centrosymmetric pattern is seen. Normals drawn from these vectors would point to an illuminating source other than R Cr A, and this is in fact T Cr A. T Cr A is not itself present in the data obtained at the JKT in 1990. However, the maps presented by Ward-Thompson in 1985 show a larger proportion of the nebula NGC6729, and the relative contributions to the observed polarization patterns by R Cr A and T Cr A are more easily compared. In some of the maps shown, there are points in the extended nebula where the polarization seems to fall towards zero; for example in the V-waveband map made from the 1990

observations (figure 3.1) at points $\sim 35''$ south of R Cr A. This is somewhat the midpoint between the two centrosymmetric patterns which we have attributed to R & T Cr A. It is likely that the two centrosymmetric patterns are cancelling each other out at this point.

As we move to points which lie $\sim 8''$ south and $\sim 15''$ north of R Cr A, there is a drop in the polarization towards zero. The V waveband dataset clearly shows a null point at a position $\sim 7''$ east & $\sim 7''$ south of R Cr A (figure 3.2). Moving further from the illuminating star a centrosymmetric pattern then predominates, and the polarization has been interpreted as due to simple scattering from an optically thin cloud where the population particles has an effective size less than the incident wavelength. The null points themselves can be explained by considering that two polarizing mechanisms are in evidence within the nebula. Close to R Cr A, polarization due to extinction (perhaps), predominates in the circumstellar disc region, and bands of parallel polarization vectors are seen. Further out in the nebula polarization due to scattering is the dominant mechanism, and a centrosymmetric pattern of polarization vectors is observed. Points are then found where there is a transition between regions where the two types of mechanisms dominate. At these points the polarizations cancel to produce the observed null points.

3.4.2 R Cr A

Running across the the intensity maximum of R Cr A a parallel band of polarization vectors are clearly seen, running in a north–south direction. This is a feature which is commonly seen across the illuminating star in many cometary reflection nebulae, NGC2261 being an excellent example. A popular explanation for this type of phenomenon which is seen at the exciting source in many reflection nebulae is that a circumstellar disc is present, and dichroic extinction by elongated dust particles aligned in a magnetic field (which is frozen-into the plane of the circumstellar disc), is responsible for the observed polarization. Assuming this interpretation is correct, a measurement of the position angle of the polarization at R Cr A, will yield a value

for the position angle of the magnetic field, and thereby the position angle for the plane of the circumstellar disc.

The most striking thing to come from the 1990 measurements of the polarization of R Cr A by the author, is the $\sim 3\%$ change in polarization and $\sim 6^\circ$ change in polarization position angle which is found in the B waveband in one 24 hour period. Rapid variations have been seen before both photometrically and polarimetrically in many T Tauri stars. In a few days R Cr A was observed to vary in magnitude by 1.3 magnitudes, (see section 3.1 and Graham & Philips 1987). Serkowski (1969b) has seen the polarization change by some 9% for R Cr A in only a few weeks in the B waveband. Serkowski (1969a) has also observed small changes in the polarization and magnitude of other T Tauri stars such as T Tau for example, in observations made 24 hours apart. The change in polarization for these observations though, was usually $< 1\%$ in 24 hours. Rotational periods of as high as 1 day have been suggested for some T Tauri stars, due to the rapid modulation of the stellar light curves perhaps by large dark spots on the stellar surface, (section 1.4.3). Photometric variability has also been seen for T Tauri stars on scales as short as 15 minutes! As a result, any rapid change in the measured polarization of R Cr A should, perhaps, be not so surprising. What is surprising though, is that no change in polarization as large as 3% has ever been reported in observations of R Cr A over such a short time period before.

If the measurements made upon R Cr A are compared to those obtained by earlier authors, it is found that there is a marked difference in results. For example, in the V waveband and using a 5" aperture, Ward-Thompson (1984 & 1985) showed R Cr A to be polarized to $7.6 \pm 0.5\%$ at a position angle of $189 \pm 5^\circ$. This compares to a value of $8.5 \pm 0.3\%$ at a position angle of $159.6 \pm 1.0^\circ$ for the 1990 V dataset. This seems to suggest then, a marked change especially in the measured polarization position angle of R Cr A in the period 1980 (when Ward-Thompson's data was taken) to 1990. The change in polarization between these two measurements is consistent with the changes reported by Serkowski in 1969(b) (almost 10% change in a few weeks) so the

change here is nothing extreme. However, the position angle has changed by $\sim 30^\circ$ in this time period. If dichroic extinction by aligned grains is the correct model for the R Cr A system, then we are saying that a large circumstellar disc must change its orientation very rapidly. Such an argument can no longer be seen as reasonable, since a model which predicts the rapid change in orientation of a circumstellar disc is difficult to explain. Even if a larger sized aperture is used in measurements of R Cr A in order to better match measurements made by other authors, large changes in the measurements still result. For example: Serkowski (1969b) finds a polarization of 17.8% at a position angle of 189.4° in the V band with an 11" aperture; Vrba *et al.* (1979): $5.6 \pm 0.2\%$ at $175.4 \pm 0.9^\circ$, with a 12" aperture; the 1990V dataset here yields $8.8 \pm 0.3\%$ at $156.4 \pm 0.9^\circ$ with a 10" aperture. Since there is a clear change in both polarization and position angle, and since dichroic extinction by aligned grains cannot satisfactorily explain the phenomena, this must now be neglected as a possible solution for the main polarizing mechanism found at R Cr A.

As with R Mon, the works of Gledhill (1991) on a polarized source model can also be applied to a consideration of the mechanisms responsible for the polarization at R Cr A, and in the extended nebula NGC6729. This author has been able to show that the observed band of parallel polarization vectors at the illuminating source star, (in this case we apply the work to R Cr A), can be explained simply by considering the illuminator as a polarized source, and without recourse to the alignment of dust grains in a magnetic field found in a circumstellar disc. (Gledhill's conclusions are drawn from mathematical modelling). The work is also able to explain the observed null points, as we move from a region dominated by a polarized source (R Cr A), to a region dominated by scattering alone (NGC6729). The polarized source model allows for rapid changes in illumination of a nebula, and can account for the rapid changes in the measured position angle close to the star, without the need to assume that the circumstellar disc itself is actually changing its position angle rapidly. Only the source of the illumination is actually changing. This has important consequences for R Cr A as well. Besides the fact that the Gledhill

polarized source model (and the Scarrott *et al.* (1991) polarized source model for the PV Cephei system) provide an alternative method for producing the observed parallel band of polarization vectors at the source, the polarized source model also allows for a rapid change in the measured polarization at the source. This is exactly what has been noted about R Cr A; the rapid change in polarization, polarization position angle and magnitude. Thus the polarized source model provides a better explanation for the observed polarization of R Cr A than other models.

If material is located unresolvably close to R Cr A, so that light leaving this clouded, obscured, or partially obscured R Cr A region becomes linearly polarized, then the result is that R Cr A acts like a polarized source. This concept was first discussed by Elsässer and Staude in 1978. A change in the distribution of material unresolvably close to R Cr A will change the scattering geometry close to R Cr A, thus altering the observed polarization of the star. This material may be in the form of clouds of dust orbiting the YSO, and this is discussed at greater length in section 2.4.1. Rapid changes in polarization could then occur as clouds of material move between the source of illumination and the observer. They would simultaneously have the effect of changing the degree of polarization of the object and changing the measured luminosity of the object. Bouvier and Bertout (1989) and Bertout (1989), have proposed that rapid changes in the luminosity of T Tauri stars can be accounted for by large dark spots on the stellar surface, which modulate the stars light-curve on short time scales due to the rapid rotational periods of the objects they looked at, (1-9 days). It is therefore possible that such a phenomenon combines with the presence of circumstellar clouds of material (unresolvably close to R Cr A) to change the polarization of R Cr A in the time scales we are dealing with. The polarized source model, in the loose way in which it is defined, also leaves open the way for the spot-light-curve modulation to be included within the model.

Rudnitskij (1987) proposed a model to account for the variability seen in many cometary nebulae, by considering a change in the illumination of a nebula due to a small-scale circumstellar disc. The disc he envisages has a radius of 10^{14} cm

(~ 7 AU), and is tilted at some angle (30°) to a larger interstellar disc, of the kind proposed by Cantó *et al.* (1981). The illumination of the nebula is then from light emerging from the poles of the T Tauri star and small disc. This disc precesses, illuminating preferentially different parts of the interstellar disc walls, and causing the nebula variability. Such a precession should cause cyclical variations to be seen in the nebula. As yet there is no firm proof that the cyclical aspect model is correct for the R Cr A/NGC6729 complex. Illumination patterns have been found to repeat themselves in NGC6729, but Bellingham and Rosano (1980) found them to be irregular. The variability of the object on the scale of days, weeks and years, only helps to hinder such searches. It should also be noted that the scale of the inner-disc in the Rudnitskij model is such that it would be unresolvable, and would therefore approximate to the polarized source interpretations discussed above and in section 2.4.1.

3.4.3 The Jets

The intensity contours on the polarization maps clearly show the position of the main jet, which runs in a south-easterly direction away from R Cr A. (This is the jet labelled R1, by Ward-Thompson *et al.* in 1985). This jet can be seen to extend at least $40''$ away from R Cr A (to the south-east), to the edge of the available dataset. The centrosymmetric pattern pattern of polarization vectors which is seen around R Cr A is not disturbed as the pattern crosses the intensity contours which signify the presence of the jet nebulosity. The pattern seen is typical of the polarizations found in reflection nebulae, which has been explained by other authors as being due to simple scattering of light within the nebula. The jet itself is shown to be significantly polarized to levels of 20%. Ward-Thompson (1984) has revealed that spectra taken of the jet reveal some shock excitation. However the polarization patterns seen illustrate that the jet, like the rest of the cometary nebula, is seen mainly by reflected light which originates at R Cr A. This is not the case for example, with the jet in HH83/Re17 (section 1.4.4), which is shown to be seen by its own

intrinsic emission (Rolph 1990).

One explanation to account for the presence of the jet is that it is a large outflow originating at the illuminating source R Cr A. The jet remains fixed in direction between observations in 1980 & 1982, (Ward-Thompson 1984) and 1990, and so it may be hypothesised that what we are seeing is outflow along the axis of rotation of R Cr A. If we are indeed seeing one half of a bipolar outflow, then a second outflow in the opposite direction might be seen. Such an outflow is not obvious in the data obtained and analysed here by the author. However, this does not prove the hypothesis incorrect, since the opposite outflow to the observed jet may be obscured by the circumstellar disc. This is a common situation that is found with cometary nebulae, that one lobe of the bipolar structure is hidden due to the tilt of the object and the presence of a disc. This has also been seen with R Mon/NGC2261, as well as in the Chamaeleon Infrared Nebula. Ward-Thompson *et al.* (1985) were able to obtain a United Kingdom Schmidt Telescope plate, (R6076), which seems to show a faint jet which is seen emerging from R Cr A in a direction which is essentially opposite to the more luminous jet R1. Their conclusion from this evidence was that we are indeed observing bipolar outflow from this R Cr A, which manifests itself in the form of a nebulous jet structure.

The main jet (R1 of Ward-Thompson *et al.*), is inclined at an angle of $\sim 60^\circ$ to the measured position angle of polarization at R Cr A. If by measuring the polarization position angle at R Cr A, we are also measuring the position angle of the circumstellar disc found there, then it must be concluded that the jet is inclined at some angle to the plane of the circumstellar disc.

Ward-Thompson *et al.* (1985) attempted to explain the jets seen emanating from R Cr A. Their explanation was that the optical jet is collimated by an inner-circumstellar disc inclined with respect to an outer disc, whilst the large scale molecular outflow is collimated by the outer-circumstellar disc. Such a system was found with NGC2261/R Mon, where a large scale interstellar ^{12}CO disc was found and mapped by Cantó *et al.* (1981). The formation of such inner- and outer-circumstellar

discs is discussed by Ward-Thompson *et al.* (1985) for the R Cr A system. Their model is summarized as follows:

The rotation of the interstellar disc proposed by Cantó (1980), causes the interstellar magnetic field in the cloud to decouple and lie in the plane of the disc. The dense central inner-regions of the disc which centre upon the protostar R Cr A, decouples from the magnetic field in the outer regions. The rapid rotation of the inner-regions of the interstellar disc cause the formation of the inner-circumstellar disc. This inner-disc is responsible for the jet collimation (they say), whilst the interstellar disc of Cantó *et al.* is responsible for the large scale CO collimation. Ward-Thompson *et al.*, then explain that the jets observed would initially be collimated by the inner-disc and field, until beyond the effective influence of their progenitor, at which point the outer-disc becomes the dominating collimator. Further work on a more general case for outflows is done by Pudritz and Norman (1986). These authors also postulate that optical jets develop as a natural part of protostellar development. Warren-Smith, Draper & Scarrott (1987a) also discuss an interesting case in the pre-main-sequence object SVS2 in the Serpens Nebula. Here, spiral structures are observed in the cloud material around SVS2, which is interpreted as the remnant of the protostellar condensation from which the object formed.

Such models which consider inner- and outer-circumstellar disc systems that are tilted relative to one another, are not totally unique. Campbell *et al.* (1988) have discussed an inner and outer disc model in attempting to explain observations of L1551-IRS5. Mundt and Fried (1983) have cited four more examples of jet-like nebulosities associated T Tauri stars. The examples they use are DG Tau, DG Tau B, HH30 and HL Tau, and they propose that these jets are highly collimated mass outflow from the young stellar objects in question. HH30 also shows evidence for the kind of “counter-jet” which other observers have found associated with R Cr A.

Cantó, Sarmiento and Rodríguez (1986) proposed a model whereby many jet-like structures are in fact not jets at all, but optical projections of the emitting wall of the bipolar or cometary cavity. This is discussed in section 1.4.5. The authors

apply their model to R Cr A, and find that it is possible to reconstruct the optical jet without the need to adopt a second inner-disc *tilted* relative to the outer-interstellar disc. Both discs can simply be orientated with their axes in an approximate east-west direction, and the “jet” is simply light emitted or reflected by the southern edge of the eastern cavity. Continuing on this argument, the faint counter-jet which was found on the Schmidt plate could then be accounted for by considering it as the emitting or reflecting wall of the obscured counterlobe. If the main jet (R1) were a purely emission feature then we would not expect to find the jet significantly polarized due to the depolarization effect of an unpolarized emission flux. In fact the main jet-like feature *is* found to be polarized to levels of 20% or more, and the centrosymmetric pattern of polarization vectors around R Cr A does not show a drop in the level of the polarization at the jet. This implies that the jet is mainly seen by reflected light from R Cr A. A jet-like feature to the south-west of R Mon was found to be significantly polarized by Warren-Smith *et al.* (1987b). Warren-Smith *et al.* concluded that what they were seeing was not a jet at all, but the illuminated western rim of the obscured southern bipolar cavity in line with the model of Cantó *et al.* (1986) as discussed in chapter 2. It therefore seems likely that the jet-like feature R1 associated with R Cr A is not a jet either, but merely the illuminated southern rim of the blueshifted eastern cavity. An intensity image of the region around the jet-like feature (figure 3.3) seems to confirm this conclusion. Nebulosity can be seen extending away to the east of R Cr A with the contours clearly defining the northerly and southerly limits of the blueshifted eastern lobe. The southern rim of the blueshifted cavity is seen preferentially no doubt, because material close to R Cr A is causing a situation to arise whereby the southern rim is illuminated preferentially. Also, it may be the case that the northern rim of the blueshifted lobe is experiencing a somewhat higher degree of obscuration.

3.5 Conclusions

R Corona Australis has been shown to be the chief illuminating star of the cometary reflection nebula NGC6729; this is clearly illustrated by the centrosymmetric pattern of polarization vectors surrounding R Cr A. Polarizations measured in the nebula of NGC6729 are typical of those found in reflection nebulae. The rapid change in the polarization and position angle of R Cr A observed in the blue spectral region in one 24 hour period has not been reported before, though larger changes on the time scale of weeks have been reported. It seems then, that the rapid change in the polarization and position angle of the star, as with the R Mon/NGC2261 and the PV Cephei/GM29 systems, seems to be best explained if we consider R Cr A to be a polarized source, where matter unresolvably close to the star is scattering, and thereby polarizing, light from it. Other polarizing mechanisms may also contribute to the observed polarization but they cannot explain the rapid changes with time. The high degree of polarization found at the jet-like feature illustrates that the feature is mostly seen by scattered light from R Cr A and not by emission. It has further been shown that what has been interpreted as an optical jet by previous authors can simply be explained as the illumination of the southern rim of the eastern blueshifted lobe.

Chapter 4

THE POLARIZATION OF THE CHAMAELEON IRN

4.1 Introduction

One of the regions of the sky which has been found to contain the signs of recent and continuing star formation is the Chamaeleon T-association. The Chamaeleon dark cloud like other dark cloud complexes is important to studies of low-mass star formation and pre-main-sequence evolution, because it is perhaps one of the closest such regions to our own sun. Whittet *et al.* (1987) have calculated the distance to the cloud to be 140 ± 12 parsecs, which is in agreement with the calculations of Rydgren (1980). The cloud also appears to have many of the signs of continuing star formation including ~ 60 optically identified young stellar objects (Assendorp *et al.* 1990), T Tauri stars (Whittet *et al.* 1987, 1991) and several Herbig-Haro objects (Schwartz 1977). Further candidate pre-main-sequence objects have been identified in the near-infrared surveys of Hyland, Jones & Mitchell (1982). The most luminous members of the association are HD97048 (Ced 111) and HD97300 (Ced 112), which both lie within reflection nebulae. These two objects are also surrounded by extended far-infrared emission, (Wesselius, Beintema & Olsson 1984). Rydgren (1980) has calculated the total mass of the Chamaeleon dark cloud complex as $\sim 670M_{\odot}$.

In 1983, Schwartz and Heinze discussed the discovery and UBVR photometry

of what they termed the “infrared nebula” (IRN), in the southern part of the Chamaeleon association. This nebula was so named because of the striking red colours the object was found to have. It also became an object of interest because the IRN had “no obvious illuminating star.” The IRN has dimensions of $\sim 125''$ by $35''$, and its axis is orientated almost east-west. Cohen & Schwartz (1984) showed the bulk of the IRN’s structure to the east to consist of complex wispy nebulosities. They also revealed that a faint nebulosity was seen in the west separated from the main body of the nebula by a clear “gap” in the nebular brightness. (This western nebulosity will be referred to hereafter as the counterlobe). The “gap” has been attributed to the presence of a circumstellar dust disc by Cohen & Schwartz and Scarrott *et al.* (1987). (Cohen *et al.* (1984) compare the presence of this gap and the general structure of the Chamaeleon IRN (Cham-IRN), with the geometry associated with the nebula around HH46). An optical knot was found at the western end of the main nebular body, whose position was calculated as $\alpha = 11^{\text{h}}07^{\text{m}}15^{\text{s}}.1$, $\delta = -77^{\circ}27'35''$ (1950), with uncertainties of $\sim \pm 2''$. This basic structure with a disc obscuring a faint counterlobe because the astronomical object is tilted to some degree from the observer, is common to cometary nebulae such as the R Mon/NGC2261 complex for example; (see chapter 2).

Given the location of the Chamaeleon Infrared Nebula in a dark cloud containing many young stellar objects (YSOs), Cohen & Schwartz believe that an infrared source (IRS) which was found close to the optical knot (see section 4.4.1) is most likely to be a YSO, and probably a T Tauri star. Using a distance of 140 parsecs to the Chamaeleon dark cloud, Cohen & Schwartz calculate that this source has a total bolometric luminosity of $14.4L_{\odot}$. They estimate that the object undergoes a visual extinction of some 10.3 magnitudes, which is consistent with the calculations of Schwartz and Heinze in 1983.

In this chapter new multicolour imaging polarimetry of this cometary reflection nebula is presented. The discussion and interpretation of the data which follow will lead to a better understanding of an object which has to date been the subject of

few astronomical observations.

4.2 Observations

4.2.1 The Aquisition of Data

Observations were made of The Chamaeleon Infrared Nebula over a period of 4 nights from January 27th to January 30th 1989 inclusive, by observers including the author. This was done at the f/18 Cassegrain focus of the 1 metre telescope of The Australian National University, at the Mount Stromlo and Siding Springs Observatory, Siding Springs, New South Wales, Australia. The Durham Imaging Polarimeter was used with a coated GEC CCD as a detector, to take a total of 24 CCD images in 3 wavebands, R, I and Z, with a total exposure time over these 24 images of 3 hours, and an image scale of $1.02''$ per pixel. The FWHM seeing experienced during the time obtaining these images was $\sim 2-3''$, whilst the combined FWHM seeing was slightly better than $3''$: ($\sim 2.5''$ in the case of the R waveband dataset; $\sim 2.3''$ for the Z).

4.3 Results

4.3.1 Polarization Maps

Linear polarization and intensity contour maps made from the data obtained are presented in figure 4.1, figure 4.2 and 4.5 for the I waveband data. In figure 4.1 the polarization has been calculated in 5 pixel ($5.1''$) square bins moved in steps of 3 pixels; in figure 4.2 the bin size was 3 pixels square moved in steps of 3 pixels.

The intensity contours in figure 4.1 and the greyscale intensity images in figures 4.3 and 4.4, clearly illustrate the east–west elongation of the nebulosity, which is dominated by the extensive eastern lobe.

The northern boundary of the eastern lobe forms a bright rim that curves away from a bright optical knot that is seen to the west of the main nebular body. Some

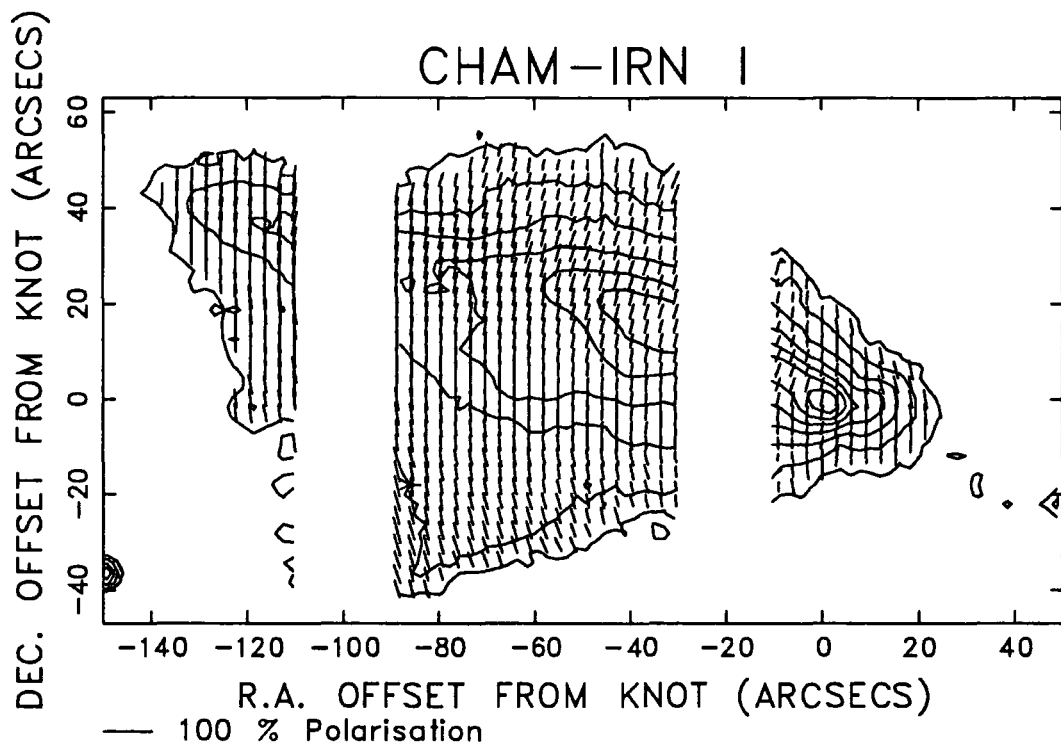


Figure 4.1: An intensity contour and polarization map of the Cham-IRN in the I waveband. The origin is at the optical knot intensity maximum.

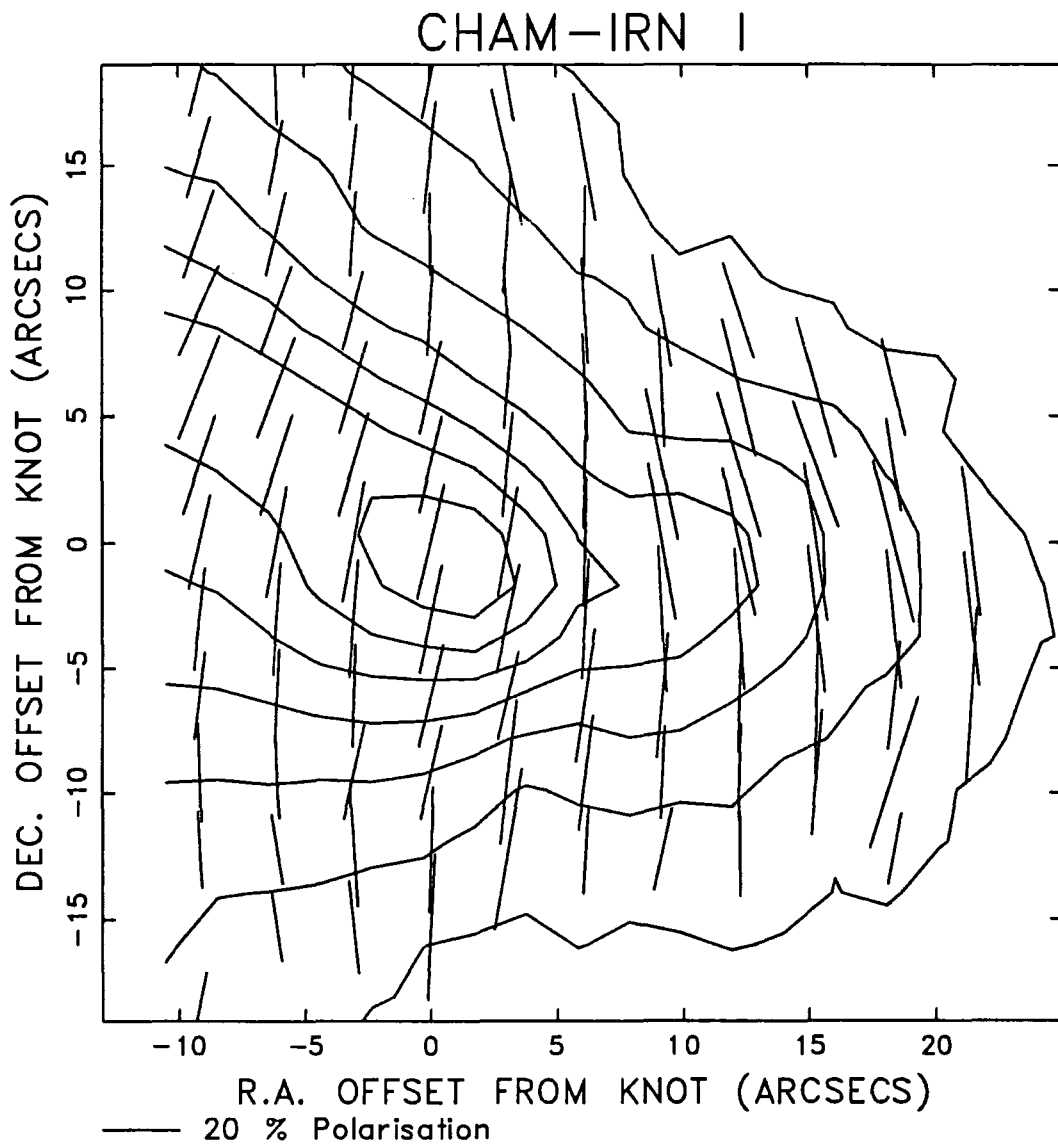


Figure 4.2: An intensity contour and polarization map of the Cham-IRN in the I waveband for the region close to the optical knot (the origin).

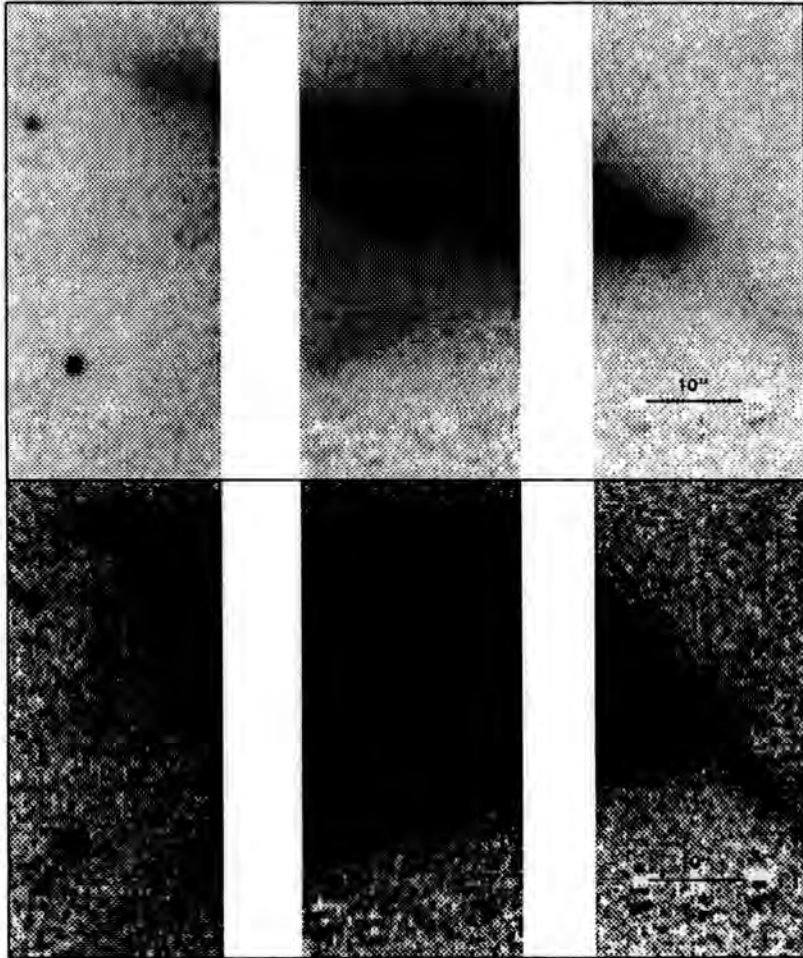


Figure 4.3: Greyscale intensity images of the Chamaeleon Infrared Nebula in the I waveband at different contrast and brightness levels. Note the jet-like structure in the bottom image.

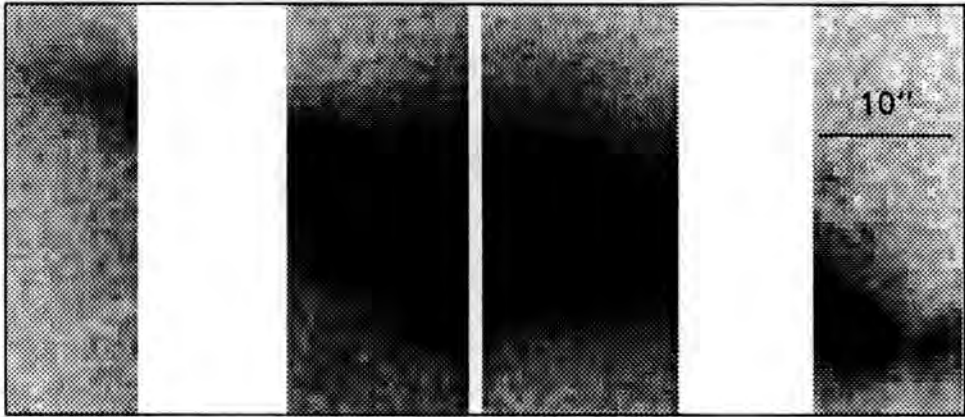


Figure 4.4: A greyscale intensity image of the Chamaeleon Infrared Nebula in the R waveband. Note the western counterlobe separated from the main nebula body by a “gap” in the nebular brightness.

10'' west of this knot a faint counterlobe is seen, which is separated from the main body of the nebula by a gap. This is clearly visible in the R waveband dataset greyscale intensity image shown in figure 4.4.

The maps presented show high levels of polarization in both lobes ranging from 20% to more than 40% in parts of the nebula. The polarization vectors form a centrosymmetric pattern that is typical of bipolar and cometary reflection nebulae. In the vicinity of the optical knot however, there is some deviation from the centrosymmetric pattern; this is also typical of some nebulae illuminated by point-like sources. This was discussed by Scarrott *et al.* (1987), who were the first to obtain polarization maps of the Cham-IRN from observations undertaken in 1985. The polarization map presented in figure 4.2 showing a field close to the optical knot reveals that the centre of the centrosymmetric pattern lies at a point $\sim 6 \pm 3''$ west of the optical knot intensity maximum.

The polarimetric data presented by Scarrott *et al.* in 1987 was taken without the use of a filter, and so consequently the data presented here is the first to be presented showing the variation of polarization with wavelength. It should also be noted that due to the lack of signal that was obtained for the Z data in the nebula, polarization measurements made far from the optical knot in this waveband have been neglected.

A greyscale intensity image was produced of the region to the west of the Cham-IRN in the I waveband, at levels which show the fainter nebulosities associated with the IRN. The bottom image in figure 4.3 reveals a jet-like structure which runs along on a line in a south-westerly direction away from the optical knot intensity maximum region. The existence of this jet-like structure has not been commented upon in previous observations by other authors. This faint nebulosity seems to be curved in its morphology and is strongly reminiscent of the jet-like feature which was found to the south-west of R Mon (see chapter 2). The polarization in this region is at levels in excess of $\sim 40\%$ (see figure 4.5).

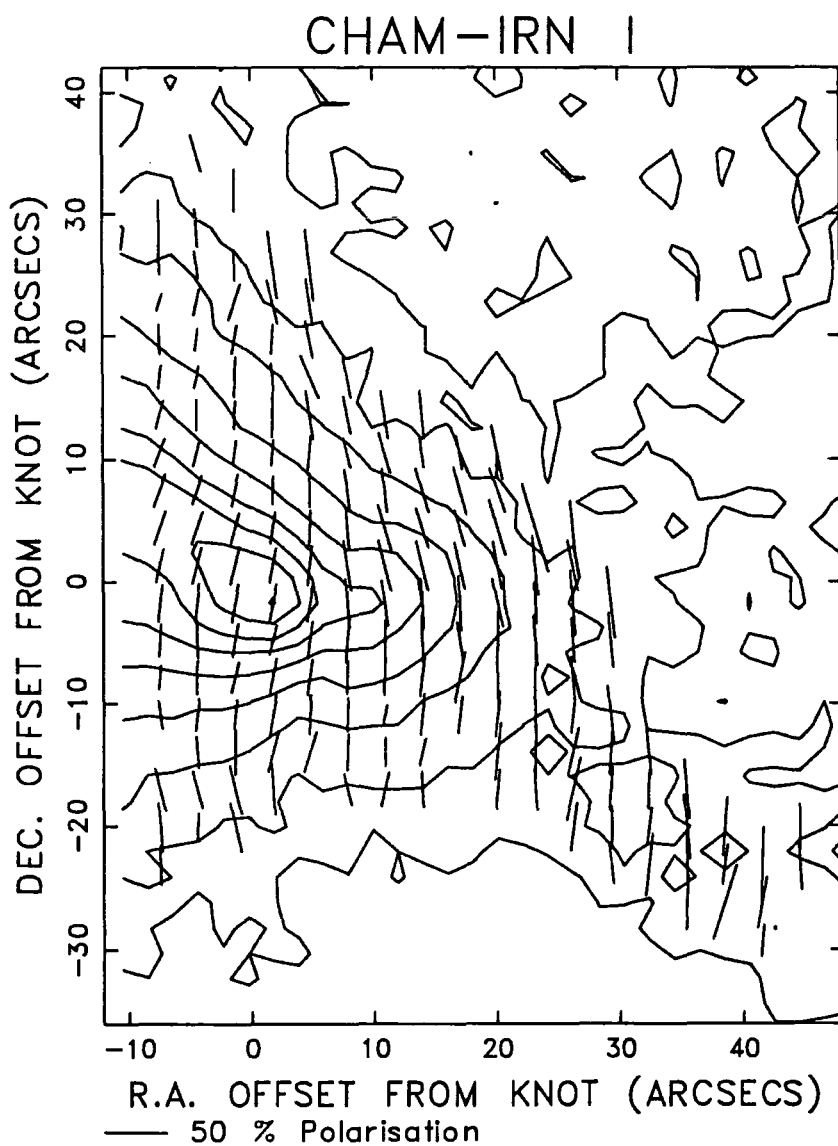


Figure 4.5: An intensity contour and polarization map of the Cham-IRN in the I waveband clearly showing the western jet-like feature.

4.3.2 Synthesised Aperture Polarimetry

Polarization measurements were made upon the Cham-IRN, with simulated circular apertures of 3'' in diameter placed 2 pixels (2.04'') apart, in a line running east–west through the optical knot to a distance of $\sim 10''$ east of and west of the optical knot (see figure 4.6).

The resulting profiles of polarization against distance from the intensity maximum (the optical knot), reveal some interesting phenomena. Firstly, the polarization seems to drop to some minimum value $\sim 3 \pm 2''$ west of the optical knot intensity maximum. Secondly, $\sim 5''$ west of the knot, the polarization begins to increase to a value of $\sim 40\%$ in the R and I wavebands at $\sim 8\text{--}10''$ west of the knot. This is at the position of the counterlobe. (In the Z waveband at this point measurements are omitted due to the increasing error on the measurements that results from lack of signal). The plots then seem to show a constant level of polarization ($\sim 40\%$) for another 5'' west until the westerly boundary of the available datasets is encountered.

In order to successfully attempt to measure the polarization of the optical knot, the counterlobe and the polarization minimum (between the optical knot and the counterlobe), apertures of a size small enough to exclude effects from the other features discovered must now be employed. Due to the results of these measurements, together with the aperture dependence of polarization tests which are discussed below, it was decided to employ an aperture of 3'' in diameter for measurements; this size is larger than the seeing disc, but it is also small enough to be able to exclude the effects of one of the Chamaeleon IRN's microstructural features (the optical knot, the polarization minimum) by another feature.

The Polarization of The Optical Knot

Simulated circular apertures ranging from 3'' in diameter up to $\sim 20''$ in diameter were centred at the optical knot.

The results are presented in figures 4.7 illustrate that there is a drop in the polarization of under 2% between that measured with a 3'' aperture and that mea-

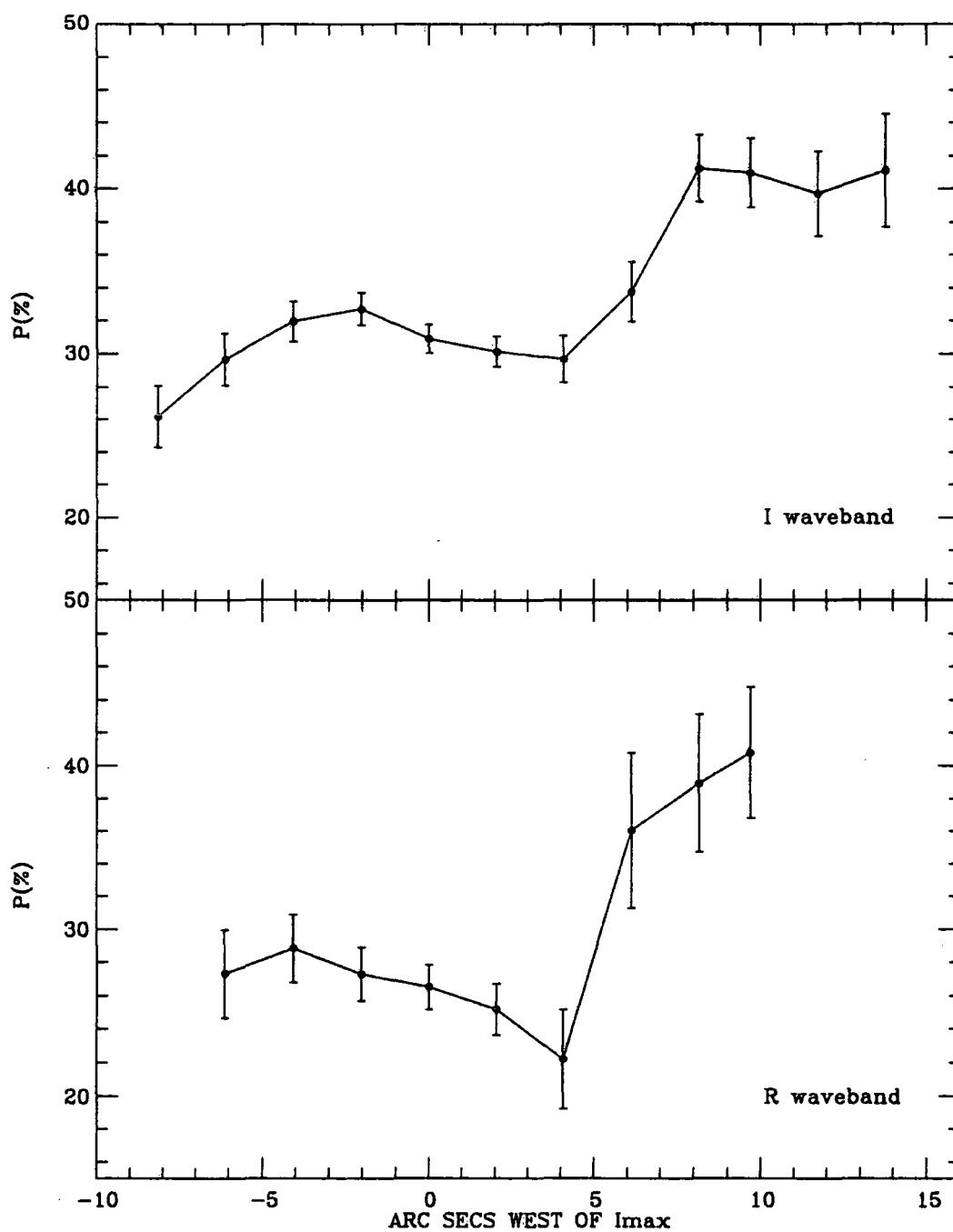


Figure 4.6: Polarization profiles made along a line east-west through the optical knot intensity maximum (I_{\max}), using a measurement aperture of $3''$ in diameter.

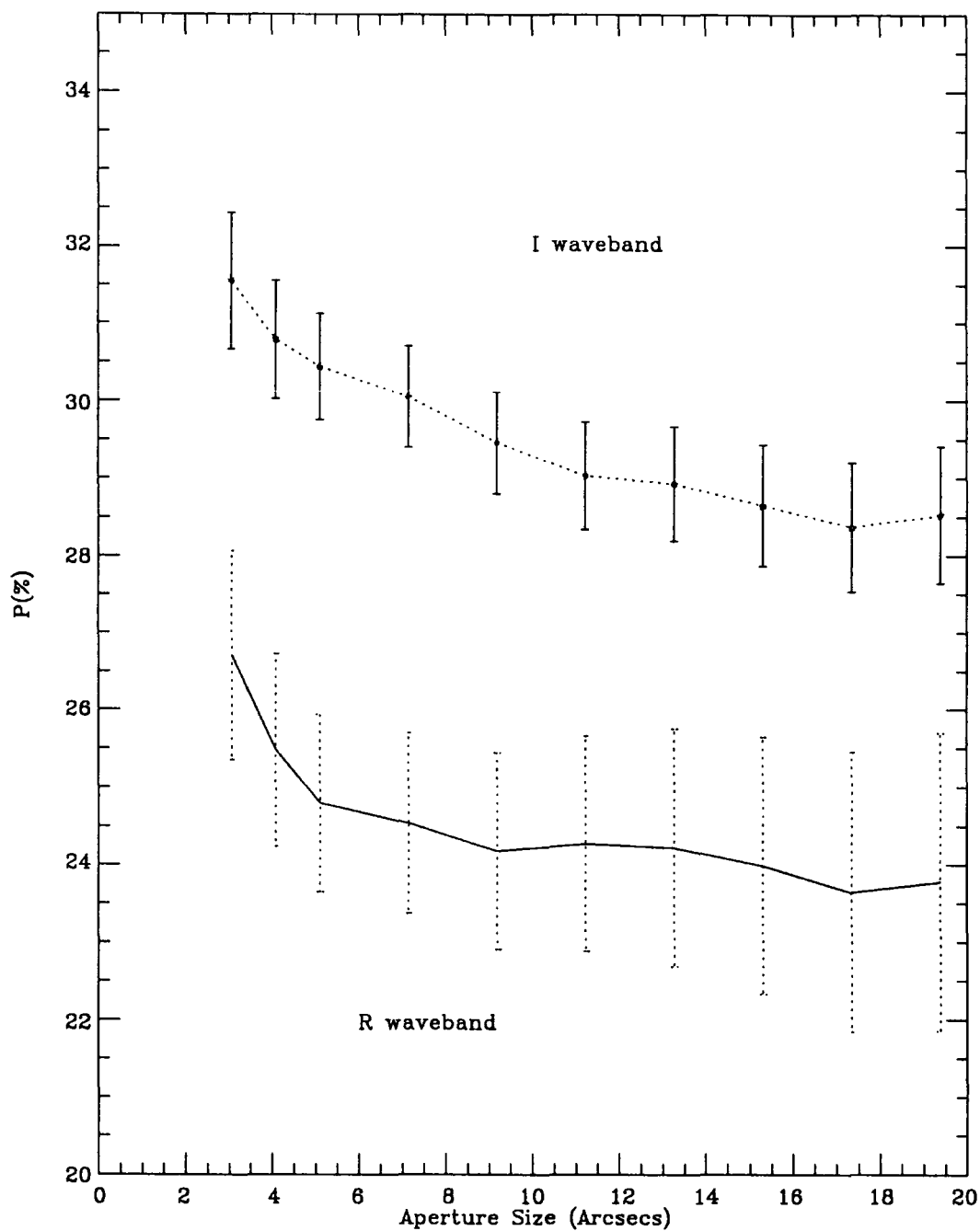


Figure 4.7: The variation of measured polarization at the optical knot with aperture size.

Chamaeleon Optical Knot 3" aperture				
Waveband	P(%)	δP (%)	θ ($^{\circ}$)	$\delta\theta$ ($^{\circ}$)
R	26.5	1.4	167.2	1.4
I	31.4	0.9	167.0	0.8
Z	29.7	3.1	163.2	2.9

Table 4.1: Aperture polarimetry with 3" apertures centred at the optical knot intensity maximum.

sured with a 5" aperture. It seems likely that this drop in measured polarization is due to the dilution of the measurement by the presence of the point of minimum polarization west of the knot discussed above. The largest change occurred in the R waveband where the measured polarization changes by 1.9%, whilst the change in the I waveband is only 0.7%. As the aperture size is increased to larger than 5" the polarization remains fairly constant, though some small decrease is found. The errors on the measurements are such that one could argue that there is little difference between measurements made with a 3" aperture and a 5" aperture. However, the very fact that a number of different features have been found in close proximity (i.e. the optical knot and the polarization minimum) encourages the use of the smaller aperture diameter (i.e. $\sim 3''$).

It was found that the optical knot was considerably polarized in the range of 25–30%. There seems to be a sharp rise in the polarization as we change wavelength from the R waveband to the I waveband, which would suggest wavelength dependence of polarization. However, when the Z waveband polarization is taken into account together with the errors, there is some possibility that the optical knot can be interpreted as showing a polarization wavelength-independent relationship. The position angle seems almost constant with wavelength at the knot, yielding a mean position angle of $\sim 166^{\circ}$ ($165.8 \pm 1.3^{\circ}$). These facts are illustrated in figure 4.8 and table 4.1.

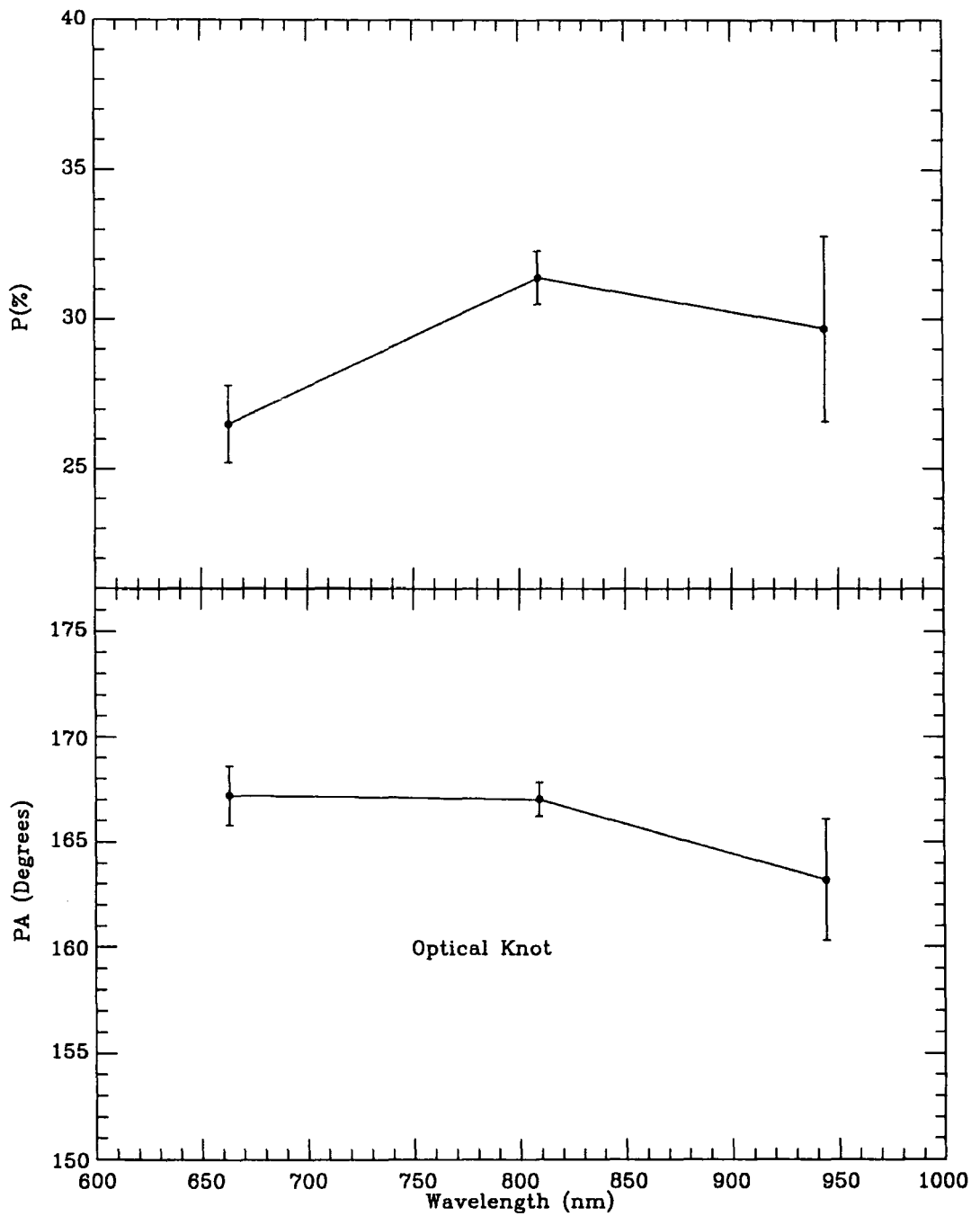


Figure 4.8: The variation of polarization and position angle at the optical knot intensity maximum, using a 3'' aperture.

Chamaeleon Polarization Minimum 3" aperture				
Waveband	P(%)	δP (%)	θ ($^{\circ}$)	$\delta\theta$ ($^{\circ}$)
R	23.4	2.0	172.7	2.4
I	29.6	1.1	169.6	1.0

Table 4.2: Aperture polarimetry at the polarization minimum.

Chamaeleon Counterlobe 3" aperture				
Waveband	P(%)	δP (%)	θ ($^{\circ}$)	$\delta\theta$ ($^{\circ}$)
R	41.6	3.8	193.9 (13.9)	2.5
I	40.1	1.9	188.4 (8.4)	1.3

Table 4.3: Aperture polarimetry with apertures centred at the Chamaeleon counterlobe.

The Polarization Minimum

Measurements were made at the approximate position of the polarization minimum (within 0.5"), with the 3" aperture. The polarization here was found to be of the order of 25–30% (see table 4.2).

The Counterlobe

Measurements made with apertures centred on the intensity maximum of the western counterlobe (see table 4.3) yielded values for the polarization in excess of 40% (see table 4.3).

The Nebula

The polarization maps presented earlier indicate that the whole of the Chamaeleon Infrared Nebula is highly polarized at levels in excess of 20%. There is little difference in the measured polarizations whether using a 5" or a 10" aperture in the nebula. The same result was echoed and discussed in polarization measurements within the

Cham-IRN 5" aperture					
Location	Waveband	P(%)	δP (%)	θ ($^{\circ}$)	$\delta\theta$ ($^{\circ}$)
35" east & 14" north	R	20.8	1.4	165.5	2.0
	I	26.3	1.0	166.0	1.1
71" east & 28" north	R	33.4	2.9	167.6	2.4
	I	43.3	1.9	168.0	1.2
79" east & 29" north	R	34.1	3.0	167.6	2.5
	I	41.7	2.5	169.4	1.6

Table 4.4: Aperture polarimetry in the Cham-IRN at a number of arbitrary points.

extended cometary nebula NGC2261 in the chapter on R Mon, (see section 2.3.4). When measurements are made at a number of arbitrary points within the IRN (see table 4.4), the measurements all yield the same pattern; the polarization was always measured to be greater in the I waveband than in the R, a result which is typical for a simple reflection nebula, NGC2261 being an excellent case in point. As an example, at a position in the IRN $\sim 35''$ east of the knot & $\sim 14''$ north, the polarizations (with a 5" aperture) were found to be $20.8 \pm 1.4\%$, and $26.3 \pm 1.0\%$ in the R and I bands respectively, (with position angles of $165.5 \pm 2.0^{\circ}$ and $166.0 \pm 1.1^{\circ}$ respectively). The polarization position angles seem consistent with them being wavelength independent over the available range (within errors), though it is difficult to draw a firm conclusions since we are dealing with only two data points. These results will be discussed in section 4.4.2.

4.4 Discussion and Interpretation

4.4.1 The Optical Knot, The Polarization Minimum and The IRS

From the appearance of the greyscale intensity images (figures 4.3 and 4.4) and the intensity contour plots on the polarization maps, it may appear that the optical knot is the illuminator of the nebula. If this is not the case then the question which must

be asked is what is causing the illumination of the optical knot? It seems that the most likely explanation is that an IRS which is found in the vicinity of the optical knot is responsible for this illumination.

Infrared photometry by Cohen & Schwartz (1984) identified a single bright infrared object at $\alpha = 11^{\text{h}}07^{\text{m}}15^{\text{s}}.1$, $\delta = -77^{\circ}27'37''$ (1950), with uncertainties of $\pm 1''$, which they deem is coincident with the position of the optical knot. Schwartz & Heinze (1983) calculated that an infrared object designated C9-2 by Hyland *et al.* (1982) was also coincident with the knot, though Schwartz and Heinze put an estimated accuracy of $\pm 5''$ on their calculations. Looking at the work of Hyland *et al.*, the position of their object C9-2 is: $\alpha = 11^{\text{h}}07^{\text{m}}12^{\text{s}}.2$, $\delta = -77^{\circ}27'37''$ (1950), with uncertainties of $\pm 10''$. Using the *IRAS Point Source Catalogue* (1988), an *IRAS* source is found to be located at $\alpha = 11^{\text{h}}07^{\text{m}}14^{\text{s}}.1$, $\delta = -77^{\circ}27'28''$ (with an error ellipse of $8''$ by $3''$, and a position angle of 169°), which is designated as *IRAS11072-7727*. There is some discrepancy between the position of these three infrared sources, but it seems likely that the IRS found by Cohen & Schwartz, C9-2 of Hyland *et al.*, and *IRAS11072-7727* are all in fact the same source. It is the conclusion of Cohen & Schwartz (1984) that within errors the position of the IRS is coincident with the position of the optical knot. However, this is not necessarily the case. Firstly it must be noted that because of the size of the errors on the IRS position, the optical knot may not be coincident with the IRS. Secondly Scarrott *et al.* (1987) go on to point out that if the elongation of the isophotes of the two lobes are projected back to a common point of intersection, then this occurs some $2''$ west and south of the intensity maximum of the optical knot. This is likely to be a pointer to the true position of the IRS. Further pointers to the position of the IRS are discussed below from results obtained at the polarization minimum and from the polarization maps.

The source star for such a cometary or bipolar nebula might be expected to be located within a circumstellar disc, and evidence for outflow should then be seen along the disc axis (see section 1.7.3). If the optical knot and the IRS are the same object, then we would need to have a line of sight close to the disc's axis in

order to see the source directly. It does not *seem* that the Cham-IRN is at such a large angle as would be needed to accomplish this feat since the opening angle of the (eastern) outflow cone is $\sim 30^\circ$, and the opening angle of the outflow cone would need to be $\geq 90^\circ$ to see the source directly down the disc axis. It seems most likely that the IRS is in fact located within the “gap” of Cohen & Schwartz; i.e. it is embedded within the circumstellar disc that surrounds the IRS, which is undoubtedly a pre-main-sequence YSO. This theory is perfectly consistent with the measurements made by Cohen & Schwartz (1984) and Hyland *et al.* (1982), because the errors quoted on their measurements are also perfectly capable of situating the IRS within the dark lane between the two nebulosities. This conclusion is realistic when we take into account the standard model of a cometary nebula (section 1.7.3), (which places the illuminator of the nebula in a circumstellar disc located between two outflow lobes). (Furthermore, the increase in polarization from the R to the I waveband is consistent with the knot being seen by reflected light from the IRS, (since this is a typical result found in simple reflection nebula). However, such interpretations would benefit greatly from observations made at a broader spread of wavelengths in order to accurately determine whether the polarization at the knot is wavelength-dependent or wavelength-independent). By tilting the nebula through an angle which is just large enough to ensure that the eastern lobe appears brighter than the western lobe because of the obscuration of the western lobe by the disc/molecular cloud, the observed illumination can easily be explained, and the IRS will still be obscured at optical wavelengths. The optical knot can be explained as being a preferentially illuminated part of the eastern cavity wall. As a result of this argument, measurements made up to $5''$ west of the optical knot intensity maximum are now representative of measurements in the circumstellar disc. These measurements drop to some minimum value which is attained $\sim 3'' \pm 2.0''$ west of the optical knot intensity maximum. It is likely that this minimum polarization point is indicative of the presence of the actual source of illumination of the Chamaeleon IRN: the IRS. If measurements are made in the close proximity of the IRS it is

possible that a greater degree of unpolarized flux will reach the observer and thereby cause some depolarization. Therefore a polarization minimum might be expected at the position of the IRS. Such a polarization minimum was found in relation to R Mon, and deemed indicative of the presence of a similar IRS. The results from polarization measurements in the data indicate the approximate position of the IRS as $\alpha = 11^{\text{h}}07^{\text{m}}12^{\text{s}}$, $\delta = -77^{\circ}27'36''$ (with errors on the position of $\pm 2''$ in declination and $\pm 2''$ in Right Ascension) in the I waveband. (Further evidence that an IRS is to be found in this disc region is found in the polarization maps in section 4.3.1, where the centre of the centrosymmetric pattern of polarization vectors seems to be located $\sim 6 \pm 3''$ west of the optical knot intensity maximum).

As has been discussed in section 2.4.1 and section 3.4.2, models which include dichroic extinction by the Davis-Greenstein mechanism as the main polarizing mechanism close to a YSO are unable to account for the rapid change in polarization and position angle observed close to R Mon and R Cr A respectively. Polarized source models such as proposed by Gledhill (1991) (and see section 2.4.1) seem better at explaining the observed phenomena.

With the Cham-IRN few polarimetric observations have been made. In fact, observations of any sort on this object are sadly lacking. As a consequence of this it is difficult to look for the sort of rapid position angle changes with time that R Mon is seen to undergo for the Cham-IRN. The only polarimetric observations to date were made by Scarrott *et al.* (1987) in 1985, without the use of a filter. It is therefore difficult to compare the percentage polarization results here (in R, I and Z) with those of Scarrott *et al.* (1987). However it should still be possible to compare the polarization position angle obtained by Scarrott *et al.* in their data, with the position angle obtained in the data presented in this chapter for the optical knot (because the polarization position angle in a simple reflection nebula is not wavelength dependent; and models of cometary nebulae would suggest that the knot is illuminated by the reflection of light from an IRS situated between the two outflow lobes). There is another problem that should be noted: the aperture polarimetry measurements were

made by Scarrott *et al.* at the optical knot *alone* (with a 5'' aperture), and no aperture measurements are presented for the polarization minimum (which has been located for the first time in the data presented in this work). Comparing measurements made at the optical knot may be inconclusive, but if any large change in position angle were observed this might be an indicator that the source of illumination is changing drastically. The R waveband dataset is the closest to the mean wavelength of the unfiltered Scarrott *et al.* data, and so these two datasets will be compared. Scarrott *et al.* find the optical knot to be polarized to 22% at a position angle of 22°. However, the measurement in the text is inconsistent with the orientation of the polarization vectors in their polarization map. It is therefore suggested that there is an error in the text, and the position angle is actually -22° (in other words 158°). This would then compare fairly favorably with the R waveband results presented in this work: $26.5 \pm 1.3\%$ at $167.2 \pm 1.4^\circ$ with a 3'' aperture, and $24.8 \pm 1.2\%$ at $166.7 \pm 1.5^\circ$ with a 5'' aperture. These comparisons draw no real conclusion. Though a change in the position angle is found, the change is not as significant as has been observed for R Cr A optical intensity maximum (chapter 3) for example. If a position angle can “change” in one direction, it can turn back again. Thus, the rapid changes found with R Mon and R Cr A cannot be ruled out, and therefore neither can the necessity for the sort of polarized source model that was required to explain the observed polarization close to R Mon.

If it is correct that the true source of illumination for the Cham-IRN is an IRS embedded in an optically thick circumstellar disc, then by the arguments of Bastien and Ménard (1988) (see section 2.4.1) dichroic extinction by aligned grains in a magnetic field cannot explain the levels of polarization (25–30%) that are observed in the “gap”/disc of the Cham-IRN. The difficulty that the Bastien and Ménard (1988) multiple scattering model has in explaining any rapid change in (polarization) position angle of the disc (see section 2.4.1) is not valid in this case, because no rapid change in the polarization position angle at the disc has been conclusively observed for the Cham-IRN. Therefore the Bastien and Ménard model cannot be ruled out as

an explanation for the polarization found in the Chamaeleon IRN. Polarized source models (see Gledhill (1991) and section 2.4.1) are also able to explain the levels of polarization observed at the disc, and further observations of the Cham-IRN are required in order to decide which model is the most appropriate for explaining the polarization at the “gap”/disc.

4.4.2 The Nebula

A typical centrosymmetric pattern of polarization vectors has been observed in the IRN. Measurements indicate that the I waveband polarization in the nebula was typically higher than the R waveband polarization at the same points. This is typical of the polarization-wavelength relationship found in many reflection nebulae including NGC2261 (chapter 2), NGC6729 (chapter 3) and the Serpens nebula (Warren-Smith *et al.* 1987a), to name but three examples. Though it is not usually advisable to draw conclusions from observations taken in only two wavebands, these results do seem consistent with considering a population of scatters whose effective size is less than the wavelength (for the reasons discussed in section 2.4.3). Further observations in a broader range filters should no doubt test the validity of this interpretation.

The Jet-Like Feature

As was mentioned in section 4.3.1 a faint jet-like structure can be seen extending away from the region of the optical knot and the IRS in a south-westerly direction. This is a new feature which has not been commented on before and is polarized to levels of $\sim 40\%$. Few observations have been made of the Cham-IRN and no spectra have been taken of the object to the author’s knowledge. However, the levels of linear polarization suggest that the “jet” is mainly seen by reflected light from the embedded IRS. The most likely explanation for this phenomenon is that what we are actually seeing is the illuminated southern rim of the obscured western cavity of the nebula. This interpretation of the jet-like features is the same as that proposed by Cantó *et al.* (1986) for a number of other objects. This explanation has also

been used by Warren-Smith, Draper and Scarrott (1987b) for similar features in the R Mon/NGC2261 complex (chapter 2) and by this author for structures emanating from R Cr A (chapter 3).

4.5 Conclusions

New observations of the cometary Cham-IRN have been presented which confirm the suggestion that the illuminating source for the nebula is an IRS embedded in a circumstellar dust disc at the location of the “gap” in the intensity images presented by Cohen and Schwartz (1984). The level of polarization which is found at the IRS position cannot be easily explained by dichroic extinction of light from the IRS by magnetically aligned grains within the disc, and so some other explanation must be found. Models which invoke the scattering of light close to the source seem better for explaining the degree of polarization found at the IRS, and polarized source models seem able to account for this; see Elsässer and Staude (1978), Gledhill (1981) and Scarrott *et al.* (1991) for example. The multiple scattering model proposed by Bastien and Ménard (1988) also seems able to account for the observed polarizations in the nebula, and the model predicts a level of polarization in the disc region which is of the correct order of magnitude.

A faint plume of nebulosity is located to the south-west of the optical knot intensity maximum and the IRS, which has never been reported in observations before the data presented here. This phenomenon seems to be best explained if we consider the feature as being the illuminated southern rim of the obscured western bipolar cavity, an interpretation which is supported by the fact that the nebulosity is seen mainly by reflected light.

The Chamaeleon IRN is a bipolar nebula whose axis is tilted such that the western counterlobe of the object is obscured by the circumstellar disc and material in the molecular cloud. Observations made in CO emission would be interesting in order to further confirm that this object does indeed have two outflow lobes. The lack of observations of the Cham-IRN makes it difficult to see if the Cham-IRN is

variable like Hubble's variable nebula NGC2261. The similarity in form between the Cham-IRN and other objects such as PV Cephei and R Mon also suggests that the polarization and position angle of the illuminating source may also change rapidly with time. As yet no evidence has been found to support this idea but further observations are undoubtedly needed to answer this question.

Chapter 5

SUMMARY AND CONCLUSIONS

It is now generally accepted that most if not all young stellar objects pass through a phase of energetic mass loss before their eventual evolution onto the main-sequence. Lada (1985) showed that of the objects he catalogued which had been mapped in molecular outflow over 70% had a bipolar morphology. Though the mechanisms which create such molecular outflows are not completely understood, it is believed that material is accelerated away from a protostar in order to reduce the angular momentum of the rotating molecular cloud core so that the star formation process may properly begin, (see section 1.3 and 1.4). This angular momentum prohibits the collapse of the cloud.

The streams of outflowing material which may be collimated by circumstellar discs and/or magnetic fields sweep up molecular cloud material in their path as they expand away from the YSO creating two roughly conical cavities. Light from the central object then illuminates these cavities creating the observed bipolar appearance at optical wavelengths. Where the object is tilted with respect to the plane of the sky, so that one lobe is seen preferentially and the other lobe is obscured by molecular material the outflow takes in the appearance of a cometary nebula (at optical wavelengths); see section 1.7.3.

In the work presented in earlier chapters, it has been shown that NGC2261,

NGC6729 and the Chamaeleon IRN are seen as cometary nebulae at optical wavelengths. There is evidence to support the ideas that they are all actually bipolar in their morphology, but one lobe is seen preferentially. These three objects contain many of the signposts characteristic of star formation such as: Herbig-Haro objects; IR excesses and T Tauri-like stars. In addition it has also been shown that there is evidence for circumstellar discs, episodic outflows and jet-like features associated with some or all of these objects.

5.1 Aperture Dependence of Polarization

One of the most important results arising from the work presented in the preceding chapters regards the aperture dependence of polarization measurements of the illuminating sources of cometary nebulae. After measurements of the polarization of R Mon in the B, V and R wavebands by Aspin, McClean and Coyne (1985) these authors concluded that the aperture size was unimportant in measurements of the polarization of R Mon. However aperture dependence tests which were reported in section 2.3.2, revealed that this conclusion is incorrect; the difference between the polarization measurements made with a 3" and 10" apertures was found to increase with increasing wavelength. This was found to be due to the contaminating effect of a highly polarized knot, possibly the northern lobe of a "mini-bipolar" nebula, when larger aperture sizes were used. This knot reaches 35% polarization in the Z waveband (section 2.3.2) and in excess of 50% in the infrared (Minchin *et al.* 1991). It is therefore suggested that in future any polarimetric measurements made upon the exciting sources of bipolar and cometary nebulae are made only after such aperture dependence of polarization tests are carried out. There is no reason why other YSOs should not also have highly polarized mini-lobes (or other features) close to them which might invalidate polarization measurements if the wrong sized aperture were used. Measurements made upon the optical knot in the Cham-IRN (chapter 4) revealed how increasing the aperture size from 3" up to 5" in size, caused some dilution of the measured polarization due to the effect of a nearby

microstructural feature (the polarization minimum which is an indicator of the true source position). However, measurements of R Cr A using a range of aperture sizes revealed no important features close to the star.

5.2 Polarized Source Interpretations

As has been discussed in chapter 2 and chapter 3, one of the popular explanations for the observed polarization found at the illuminating source of cometary and bipolar nebulae, namely dichroic extinction caused by the Davis-Greenstein effect, can no longer be accepted as the main polarizing mechanism in such sources. One of the problems that this model has is explaining the rapid change in polarization and position angle observed at YSOs like R Mon and R Cr A.

Polarized source models such as those initially proposed by Elsässer and Staude and expanded upon by Gledhill (1991) seem able to account for the observed polarization in a much more satisfactory way. The polarized source interpretation removes the need to consider a circumstellar disc that rapidly changes its orientation. The model simply considers that matter is situated unresolvably and anisotropically around the source. Changes in the geometry of the distribution of material close to the star will then change the observed polarization of the source on short time scales. This is the model adopted for explaining the polarization observed at R Mon and R Cr A, and may also explain the polarization in the Cham-IRN. It is proposed that this model could be applicable to a large number of star forming regions at similar evolutionary stages; further polarization measurements of likely candidates would be required to demonstrate this.

5.3 Jets

It was shown in chapter 3 that in confirmation of the model of Cantó *et al.* (1986), the “jet” seen emanating close to R Cr A and extending in a south-easterly direction away from the YSO can simply be interpreted as the illuminated southern rim of

eastern bipolar cavity. The jet-like feature is significantly polarized and does not suffer any of the obvious depolarization that would be expected if the jet were seen mainly in emission. This structure is seen mainly by reflected light from R Cr A. Similarly, a jet-like feature to the west of the IRS in the Cham-IRN seems to be seen predominantly in reflected light. It was therefore postulated in section 4.4.2 that the feature is the southern rim of the western cavity, though further observations of the Cham-IRN are needed to confirm this.

The conclusions obtained in chapter 3 for R Cr A, chapter 4 for the Cham-IRN, and independently by Warren-Smith *et al.* (1987b) for R Mon, illustrate that observations of jet-like nebulosities using polarimetry reveal that no emission jet is seen emanating from these objects.

5.4 Future Observations

Although the cometary nebula NGC2261 and its illuminator R Mon have been studied in great depth, the other two objects examined in this work could be more easily understood if additional observations were carried out. In particular the following observations are suggested:

1. Chamaeleon IRN

- Maps of the CO emission are required to confirm that the Chamaeleon IRN is truly bipolar in morphology .
- Polarimetry and photometry over an extended time period are needed to test if the IRN and IRS are variable in the same way that R Mon and R Cr A have been found to be. If this were found to be so, then a polarized source interpretation would be needed to better explain the observed polarizations.
- Spectroscopy is needed to test if the IRS is a T Tauri star. The spectrum of the nebula can be examined to see if it shows typical T Tauri emission-line characteristics due to reflection of light from the source.

2. R Cr A

- Frequent polarimetric observations over an extended period are needed. Does R Cr A show any regular pattern in the change of its polarization with a period of weeks or even days?

3. Other Cometary Nebulae Other cometary nebulae and their exciting sources need to be closely examined to see if they undergo to the sort of rapid changes in luminosity and polarization that might be indicative that a polarized source mechanism is in operation.

5.5 Final Remarks

Polarimetry has been shown to be an effective tool in mapping, and understanding the environs, of reflection nebulosities. The technique can be used in the identification (or confirmation) of the positions of the illuminating sources in various cometary nebulae. It is also clear that polarimetry can make an important contribution to the understanding of the physical process that a young stellar object experiences during its pre-main-sequence evolution.

Cometary nebulae represent an important stage in the star formation process, and further studies of them should reveal more information about the transition between protostar and zero age main sequence.

Appendices

Appendix A

Polarization Maps of R Mon/NGC2261

In this appendix polarization maps of the R Mon/NGC2261 cometary nebula which do not appear in chapter 2 are presented. The datasets presented are many of those from the 1989 and 1990 observing runs (see chapter 2).

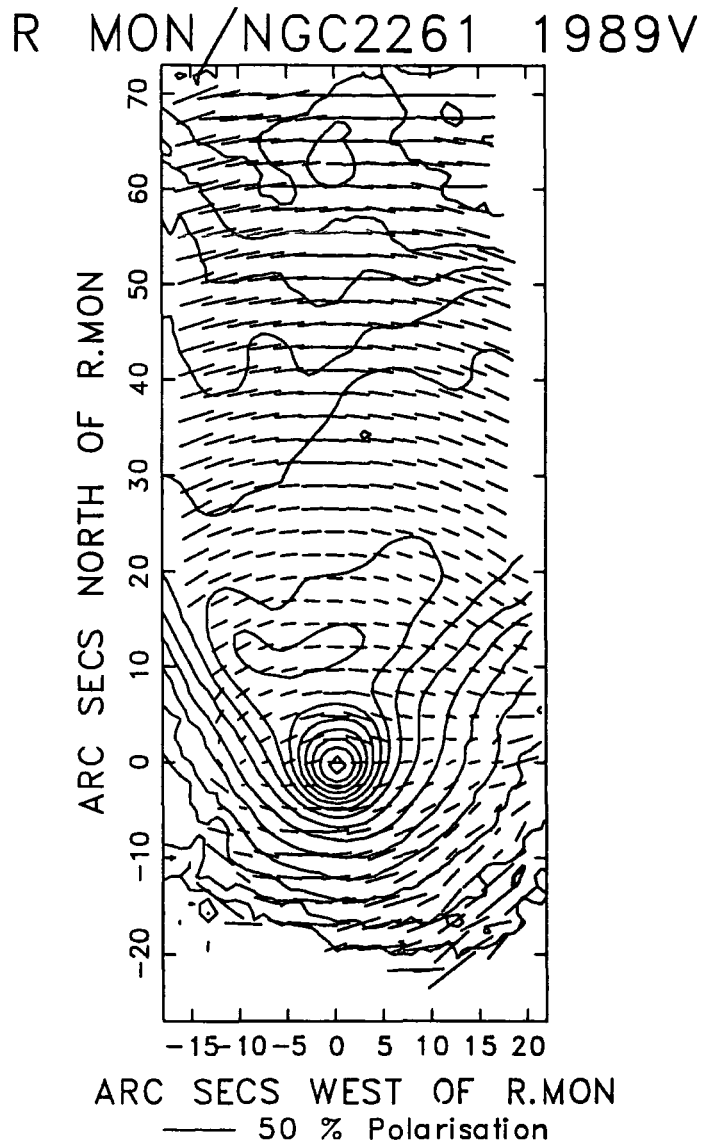


Figure A.1: R Mon/NGC2261 1989 V dataset.

R MON/NGC2261 1989R

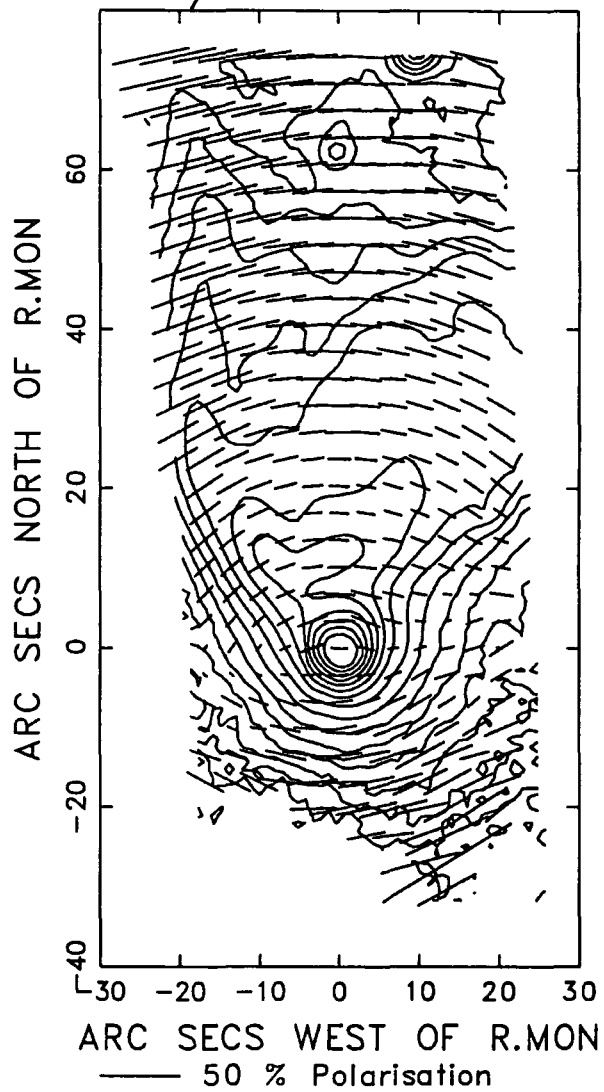


Figure A.2: R Mon/NGC2261 1989 R dataset.

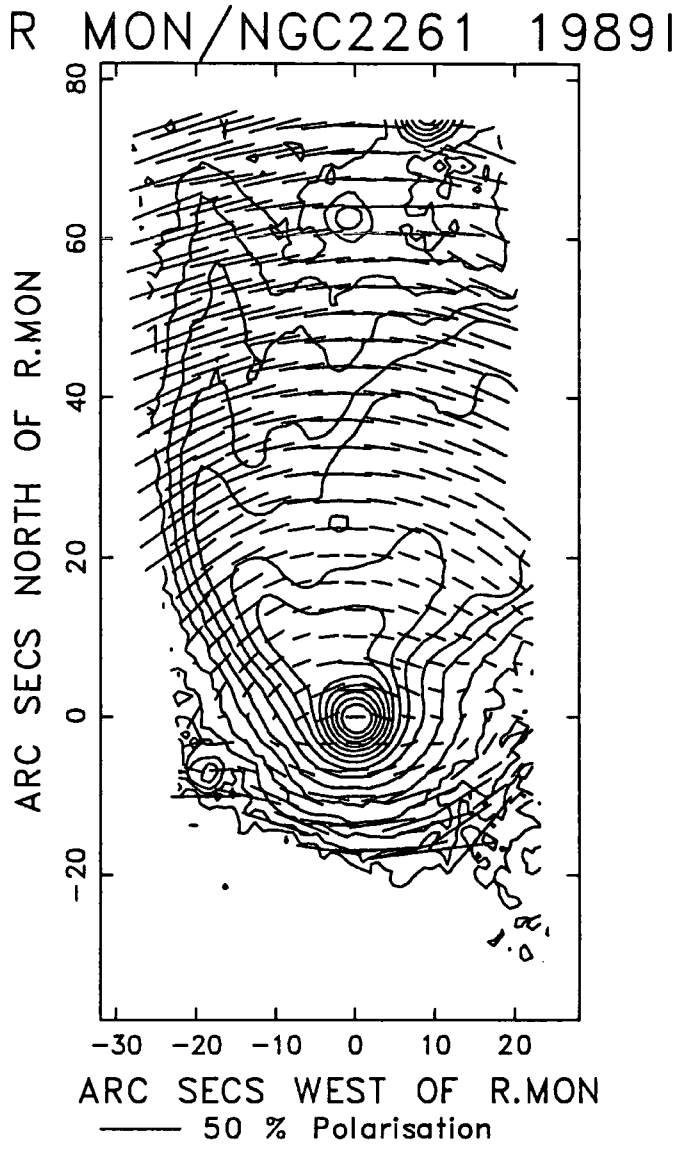


Figure A.3: R Mon/NGC2261 1989 I dataset.

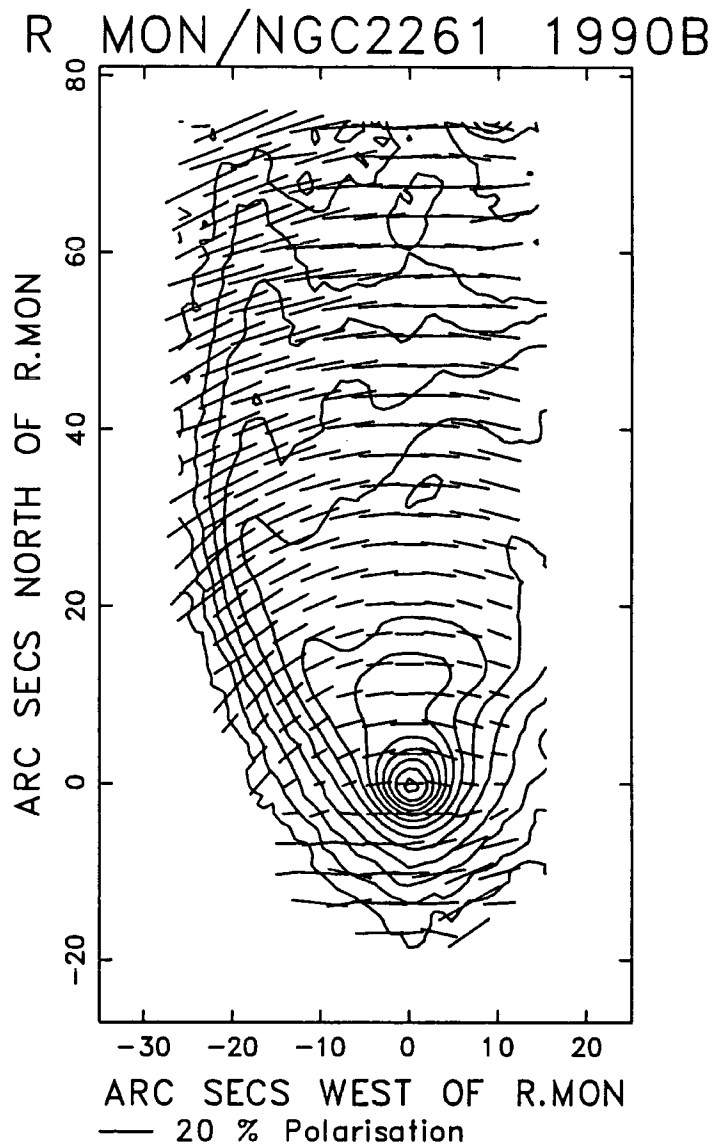


Figure A.4: R Mon/NGC2261 1990 B dataset.

R MON/NGC2261 1990V

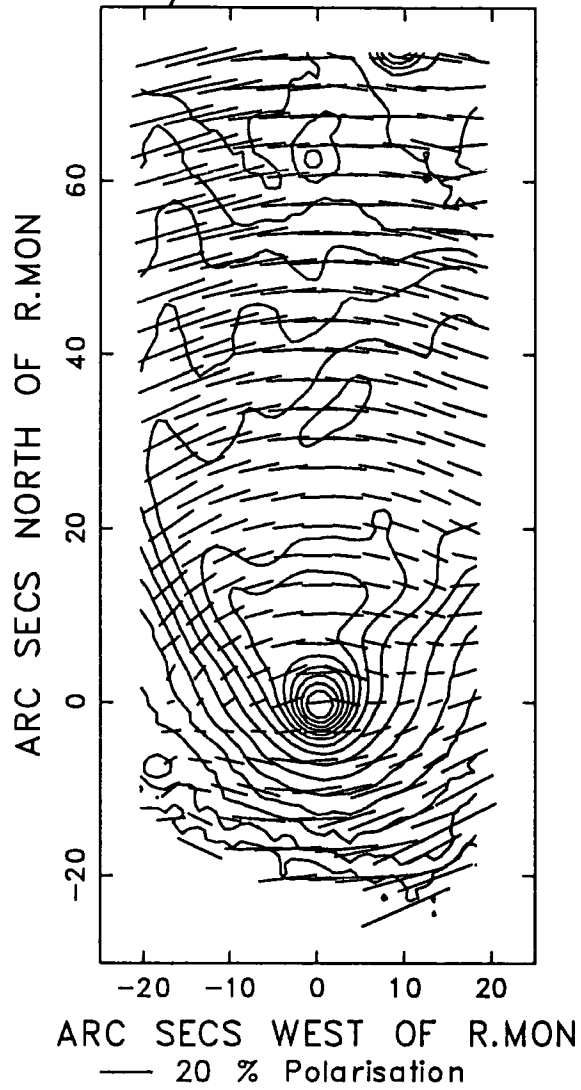


Figure A.5: R Mon/NGC2261 1990 V dataset.

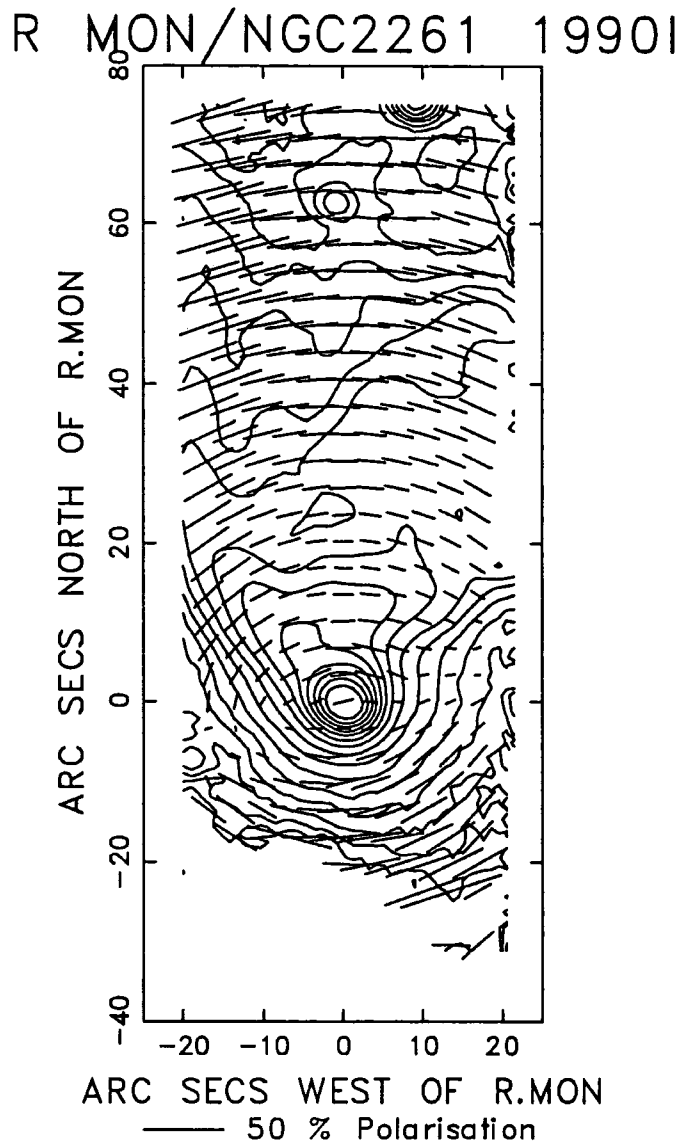
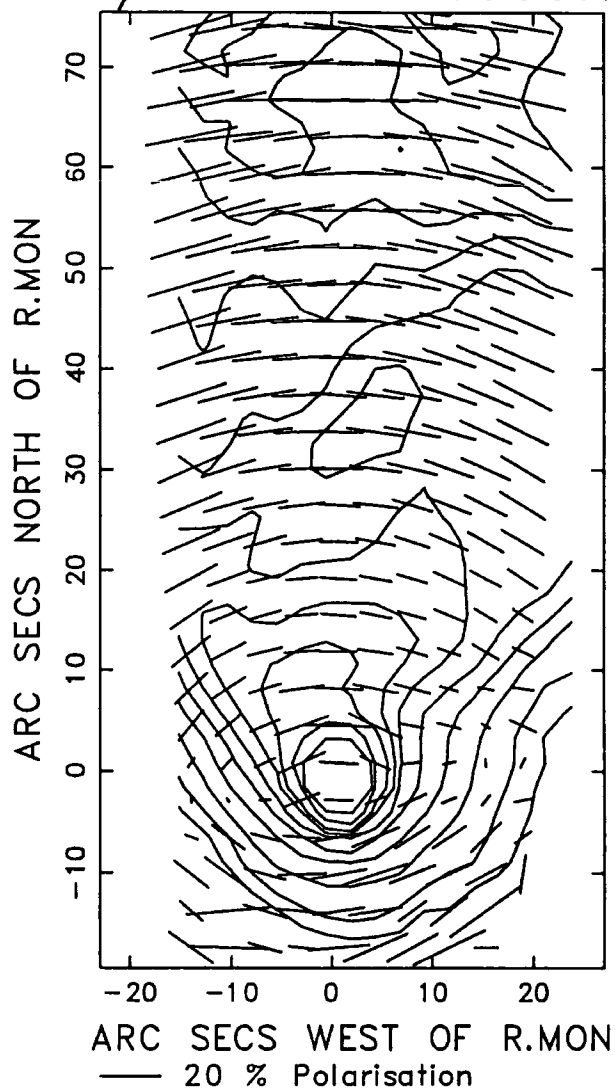


Figure A.6: R Mon/NGC2261 1990 I dataset.

R MON/NGC2261 1990HALPHA

Figure A.7: R Mon/NGC2261 1990 H α dataset.

Appendix B

Filter Responses

Filter response when convolved with CCD			
Filter	Peak λ (nm)	Mean λ (nm)	Bandwidth $\delta\lambda$ (nm)
B	438	440	103
V	550	552	86
R	629	663	164
I	758	809	141
Z	951	944	100
No filter	675	651	387
H α	656.0	655.6	5.9
Continuum	665.2	664.4	4.9

Table B.1: Filter response when convolved with the coated GEC CCD as a detector for the Durham Imaging Polarimeter, for data taken since 1988. Data provided by Dr. C. D. Rolph. For data previous to this see Draper (1988).

References

- Aspin, C, McClean, I.S. & Coyne, G.V., 1985. *Astr. Ap* **149** 158.
- Asendorp, R., Wesselius, P.R., Whittet, D.C.B. & Prusti, T., 1990. *M.N.R.A.S.* **247** 624.
- Bastien, P., 1987. *Ap. J.* **317** 231.
- Bastien, P. & Ménard, F., 1988. *Ap. J.* **326** 334.
- Beckwith, S., Sargent, A.I., Scoville, N.Z., Masson, C.R., Zuckerman, B. & Philips, T.G. 1986. *Ap. J.* **309** 755.
- Bellingham, J.G. & Rossano, G.S., 1980. *Astr. J.* **85** 555.
- Bertout, C., 1989. *Ann Rev. Astr. Ap.* **27** 351.
- Bouvier J., & Bertout C., 1989. *Astr. Ap.* **211** 99.
- Brugel, E.W., Mundt, R. & Bührke, 1984. *Ap. J.* **287** L73.
- Campbell, B., Persson, S.E., Strom, S.E. & Grasdalen, G.L., 1988. *Astr. J.* **95** 1173.
- Cantó, J. & Rodríguez, L.F., 1980. *Ap. J.* **239** 982.
- Cantó, J., Rodríguez, L.F., Barral, J.F. & Carral, P., 1981. *Ap. J.* **244** 102.
- Cantó, J., Sarmiento, A. & Rodríguez, L.F., 1986. *Rev. Mexicana Astr. Af.* **13** 107.
- Cantó, J. & Raga, A.C., 1991. *Ap. J.* **372** L646 .
- Cohen, M., 1974. *Pub. A.S.P.* **86** 813.
- Cohen, M., 1982. *Pub. A.S.P.* **94** 266.
- Cohen, M. & Schwartz, R.D., 1983. *Ap. J.* **265** 894.
- Cohen, M. & Schwartz, R.D., 1984. *Astr. J.* **91** 277.
- Cohen, M., Schwartz, R.D., Harvey, P.M. & Wilking, B.A., 1984. *Ap. J.* **281** 250.

- Cruz-Gonzalez, I., McBreen, B. & Fazio, G.G., 1984. *Ap. J.* **279** 679.
- Cudworth, K.M. & Herbig, G.H., 1979. *Astr. J.* **84** 548.
- Dibai, É.A., *Sov. Astron. A.J.* 1971 **14** 785.
- Draper, P.W., 1988. Ph.D. thesis, Univ. of Durham.
- Draine, B.T., 1983. *Ap. J.* **270** 519.
- Elsässer, H. & Staude, H.J., 1978. *Astr. Ap.* **70** L3.
- Garrison, L.M. & Anderson, C.M., 1978. *Ap. J.* **221** 601.
- Gething, M.R., Warren-Smith, R.F., Scarrott, S.M., Bingham, R.G., 1982. *M.N.R.A.S.* **198** 881.
- Glass, I.S. & Penston, M.V., 1975. *M.N.R.A.S.* **172** 227.
- Gledhill, T.M., 1991. *M.N.R.A.S.* (in press).
- Graham, J.A. & Philips, A.C., 1987. *PUB. A.S.P.* **98** 91.
- Hall, R.C., 1965. *Ap. J.* **77** 158.
- Hartigan, P. & Graham, J.A., 1987. *Astr. J.* **93** 913.
- Herbig, G.H., 1968. *Ap. J.* **152** 439.
- Herbig, G.H., 1960. *Ap. J. Suppl.* **4** 337.
- Hubble, E.P., 1916. *Ap. J.* **44** 190.
- Hyland, A.R., Jones, T.J. & Mitchell, R.M., 1982. *M.N.R.A.S.* **201** 1095.
- Jones, B.F. & Herbig G.H., 1982. *Astr. J.* **87** 1223.
- Jones, T.J. & Dyck, H.M., 1978. *Ap.J.* **220** 156.
- Joy, A.H., 1945. *Ap. J.* **102** 168.
- Knacke, R.F., Strom, K.M., Strom, S.E., Young, E. & Kunkel, W., 1973. *Ap. J.* **179** 847.
- Knox-Shaw, H., 1916. *M.N.R.A.S.* **76** 646.
- Königl, A., 1982. *Ap. J.* **261** 115.
- Kuhi, L.V., 1978. in *Protostars and Planets* ed. Gehrels T., University of Arizona Press.
- Lada, C.J., 1985. *Ann. Rev. Astr. Ap.* **23** 267.
- Lampland, C.O., 1926. *Popular Astr.* **34** 621.

- Lampland, C.O., 1931. *Pub. A.S.P.* **43** 296.
- Lampland, C.O. & Ashbrook, J., 1949. *Astr. J.* **54** 91.
- Levreault, R.M., 1984. *Ap. J.* **277** 634.
- Levreault, R.M., 1984. *Ap. J.* **277** 634.
- Lightfoot, J.F., 1989. *M.N.R.A.S.* **239** 665.
- Loren, R.B., 1979. *Ap.J.* **227** 832.
- Low, F.J. & Smith, B.J., 1966. *Nature* **212** 675.
- Marraco, H.G. & Rydgren, A.E., 1981. *Astr. J.* **86** 62.
- Ménard, F., Bastien, P. & Robert, C., 1988. *Ap. J.* **335** 290.
- Mendoza, E.E., 1966. *Ap. J.* **143** L1010.
- Minchin, N.R., Hough, J.H., McCall, A., Aspin, C., Yamashita, T. & Burton, M.G., 1991. *M.N.R.A.S.* **249** 707.
- Mouschovias, T. Ch., 1980. *IAU Symp.* **93** .
- Mundt, R., 1985. in *Protostars and Planets II* ed. Gehrels. T., University of Arizona Press.
- Mundt, R. & Fried, J.W., 1983. *Ap. J.* **274** L83.
- Norman, C. & Silk, J., 1979. *Ap. J.* **228** 197.
- Reynolds, J.H., 1916. *M.N.R.A.S.* **76** 645.
- Rudnitskij, G.M., 1987. *IAU Symp.* **115** 398.
- Rydgren, A.E., & Vrba, F.J., 1983. *Ap. J.* **267** 191.
- Pudritz, R.E., & Norman, C.A., 1983. *Ap. J.* **274** 677.
- Pudritz, R.E., 1985. *Ap. J.* **293** 216.
- Pudritz, R.E., & Norman, C.A., 1986. *Ap. J.* **301** 571.
- Rolph, C.D., 1990. Ph.D. thesis, Univ. of Durham.
- Rolph, C.D., Scarrott, S.M. & Wolstencroft, R.D., 1990. *M.N.R.A.S* **242** 109.
- Rydgren, A.E., 1980. *Astr. J.* **85** 444.
- Sato, S., Nagata, T., Nakajima, T., Nishida, M., Tanaka, M. & Yamashita, T., 1985. *Ap. J.* **291** 708.

- Scarrott, S.M., Warren-Smith, R.F., Pallister, W.S., Axon, D.J., & Bingham, R.G., 1983. *M.N.R.A.S.* **204** 1163.
- Scarrott, S.M., Warren-Smith, R.F., Wolstencroft, R.D. & Zinnecker, H., 1987. *M.N.R.A.S.* **228** 827.
- Scarrott, S.M., Draper, P.W. & Warren-Smith, R.F., 1989. *M.N.R.A.S.* **237** 621.
- Scarrott, S.M., Rolph, C.D. & Semple, D.P., 1990. *IAU Symp.* **140** 245.
- Scarrott, S.M., Rolph, C.D. & Tadhunter, C.T., 1991. *M.N.R.A.S.* **249** 1131.
- Schwartz, R.D., 1977. *Ap. J. Suppl.* **35** 161.
- Schwartz, R.D., 1978. *Ap.J.* **223** 884.
- Schwartz, R.D., 1983. *Ann. Rev. Astr. Ap.* **21** 209.
- Schwartz, R.D., & Heinze, K.G., 1983. *Astr. J.* **88** 1665.
- Schwartz, R.D., Jones, B.F., Sirk, M., 1984. *Astr. J.* **89** 1735.
- Schwartz, R.D., 1985. in *Protostars and Planets II* ed. Gehrels. T., University of Arizona Press.
- Serkowski, K., 1969a. *Ap. J.* **156** L55.
- Serkowski, K., 1969b. *Ap. J.* **158** L107.
- Shibata, K., & Uchida, Y., 1987. *IAU Symp.* **115** 385.
- Shklovskii, I.S., 1978. *Stars: Their Birth, Life and Death* W.H. Freeman and company, ISBN 0-7167-0024-7.
- Shu, F.H., Adams, F.C. & Lizano, S., 1987. *Ann. Rev. Astr. Ap.* **25** 23.
- Smith, B.A. & Terrile, R.J., 1984. *Science* **226** 1421.
- Snell, R.L., Loren, R.B., Plambeck, R.L., 1980. *Ap. J.* **239** L17.
- Strom, S.E., Strom, K.M., Grasdalen, G.L., 1975. *Ann. Rev. Astr. Ap.* **13** 187.
- Strom, K.M., Strom, S.E., Grasdalen, G.L., 1974a. *Ap. J.* **187** 83.
- Strom, S.E., Grasdalen, G.L., Strom, K.M., 1974b. *Ap. J.* **191** 111.
- Strom, K.M., Strom, S.E. & Kinman, T.D., 1974c. *Ap.J.* **191** L93.
- Tayler, R.J., 1978. *The Stars: Their Structure and Evolution* Wykeham Publications (London) Ltd, ISBN 0-85109-11-0-5.
- Taylor, K.N.R. & Storey, J.M.V., 1984. *M.N.R.A.S.* **209** 5p.

- Uchida, Y. & Shibata, K., 1985. *Pub. Astr. Soc. Japan* **37** 515.
- Uchida, Y., Kaifu, N., Shibata, K., Hayashi, S.S., Hasegawa, T., 1987. *IAU Symp.* **115** 287.
- Vrba, F.J., 1977. *Astr. J.* **82** 199.
- Vrba, F.J., Strom, S.E. & Strom, K.M., 1976a. *Astr. J.* **81** 958.
- Vrba, F.J., Strom, S.E. & Strom, K.M., 1976b. *Astr. J.* **81** 317.
- Vrba, F.J., Schmidt, G.D. & Hintzen, P.M., 1979. *Ap. J.* **227** 185.
- Vrba, F.J., Coyne, G.V. & Tapia, S., 1981. *Ap. J.* **243** 489.
- Walsh, J.R. & Malin, D.F., 1985. *M.N.R.A.S.* **217** 31.
- Ward-Thompson, D.W., 1984. M.Sc. thesis, Univ. of Durham.
- Ward-Thompson, D.W., Warren-Smith, R.F., Scarrott, S.M. & Wolstencroft, R.D., 1985. *M.N.R.A.S.* **215** 537.
- Warren-Smith, R.F., 1979. Ph.D. thesis, Univ. of Durham.
- Warren-Smith, R.F., Draper, P.W. & Scarrott, S.M., 1987a. *M.N.R.A.S.* **227** 749.
- Warren-Smith, R.F., Draper, P.W. & Scarrott, S.M., 1987b. *M.N.R.A.S.* **315** 500.
- Wesselius, P.R., Beintema, D.A. & Olton, F.M., 1984. *Ap. J.* **278** L37.
- Whitney, W.T. & Weston, E.B., 1948. *M.N.R.A.S.* **107** 371.
- Whittet, D.C.B., Kirrane, T.M., Kilkenny, D., Oates, A.P., Watson, F.G. & King, D.J., 1987. *M.N.R.A.S.* **224** 497.
- Whittet, D.C.B., Prusti, T. & Wesselius, P.R., 1991. *M.N.R.A.S.* **249** 319.
- Wilking, B.A., Harvey, P.M., Joy, M., Hyland, A.R. & Jones, T.J., 1985. *Ap. J.* **293** 165.
- Zellner, B., 1970. *Astr. J.* **75** 182.

Acknowledgements

I remember back in 1987 being interviewed at the Royal Observatory, Edinburgh, and being asked why it was that I wanted to do a Ph.D. in astronomy. I spoke the truth when I responded: *in my heart I have to be involved in astronomy, somehow, someway; it doesn't matter if I come out of a Ph.D. hating astronomy, it is something I have to be involved in.*

As a result it is my pleasure to thank my supervisor Dr. S.M.Scarrott, for the opportunity he gave me back in 1988 to undertake astronomical research in Durham. Similarly, I would like to thank Dr. J.V.Major for his attempts in 1987 to find me a Ph.D. studentship. I also thank Dr. Scarrott for the help he has given me over the last three years.

I am greatly indebted to Tim Gledhill, Peter Draper and Nick Eaton for their help and many discussions on various aspects of stellar evolution and polarimetry. I also apologise to Tim for all the times he was startled by my *redshifted* body zooming across our third floor office.

Neasa Foley and Sue Watkin are thanked for making our office all the more lively over the last twelve months, whilst David Stockdale is thanked for making the corridors equally lively. Foley (private communication) is acknowledged for the last few words. Gordon Love is thanked for impromptu tutorials, while Phillip Armstrong, the man who built the Durham Polarimeter, is thanked for making everything possible. He is also acknowledged for imparting his own particular brand of humour on the one observing run we shared.

Data reduction was carried out on the Durham node of the STARLINK Vax cluster, and also on the polarimetry group's own Vaxstation 3100. Alan Lotts is thanked for his continuing hard work in keeping everything going, and for his advice on all manner of things. Professor A.W.Wolfendale and Professor Martin, successive heads of department during my time as a research student, are acknowledged for their efforts in keeping the department running smoothly.

Team members of *Astro-A* are thanked for their faith in me as their team manager/captain during our glorious season as the team with the biggest goal difference in the University 5-a-side league: Tim Gledhill, Chris Rolph, David Stockdale, Peter Doel, Steve Rayner, Chris Bowden, Richard Bower, Ian Lewis & (nearly) Nial Tanvir!

Further thanks are bestowed upon a number of people who have contributed in various ways to my studies/life in Durham. Father John (Jessie) James: for his unique brand of humour which was one of the highlights of three years in Durham; (*Vaya con Dios*). Shirlene Oh; Dr. Ray Wolstencroft; Dr. D.N.Edwards & Dr. M.F.Thomas my tutors at the University of Liverpool.

I must express gratitude to my parents for all their love, support, and help which has seen me progress this far. Fiona Robinson is thanked not simply for checking the grammar in some of the early manuscripts, but mostly for all her love, support, encouragement, and for the confidence in me which she expresses at all times.

My greatest thanks are reserved until last. I unreservedly acknowledge the help and advice given to me by Chris Rolph over the last three years, and especially over the last twelve months. He is thanked for all manner of advice polarimetric, and for a seemingly endless tally of tutorials. I, thank, him, for, reading, over, all, my, chapters, at the different stages of my write up, and for the expert help with \LaTeX which undoubtedly saved me countless hours grappling with the \LaTeX manual.

